ACCRETION AND OUTFLOW IN BLACK-HOLE X-RAY BINARIES

Mr. Avishek Dusoye
Department of Astronomy
University of Cape Town

30 November 2014

A dissertation submitted in full fulfilment of the requirements for the degree
of MSc by Research in the Department of Astronomy
UNIVERSITY OF CAPE TOWN

Supervisors: Dr M. Coriat and A/Prof. P. Woudt
Department of Astronomy
University of Cape Town

Abstract

Black hole X-ray binaries (BHXBs) are stellar binary systems consisting of a black hole (BH) and a companion star. They are known to produce X-ray emission through the accretion of mass from the companion star onto the black hole via an accretion disc, as well as radio emission originating from their jets. My thesis splits into two projects. On one hand, I focus on the connection between the X-ray emitting accretion disc and the radio jets of BHXBs in general, by studying the quasi-simultaneous evolution of the radio fluxes and the X-ray fluxes from 17 BHXBs. This connection, also known as the radio/X-ray correlation has been studied and updated over the past years. New observations of new and known sources have shown that another population of X-ray binaries exists (referred to as outliers), lying below the standard radio/X-ray correlation. I investigate whether the mass of the black hole component of BHXBs can explain the existence of these outliers. In my second project, I focus on an exotic source, known as SS433. It has a supercritical accretion disc and displays precessing relativistic jets. I investigate whether these jets are made up of proton-electron plasma or electron-positron plasma. Circular polarization (CP) is a good diagnostics for understanding the particle composition of radio jets. Therefore we have observed the circular polarized flux densities of SS433 using the Australia Telescope Compact Array (ATCA) for a broad range of frequencies between $1.4 - 10$ GHz. From those observations, a CP spectrum can be constructed and the spectral index can be estimated. There are 4 ways of producing CP emission and the spectral index helps us to constrain the CP production mechanism. In addition, the kinematics of propelling a proton-electron plasma in a jet is different from that of electron-positron plasma. I simulate various plausible models for the energy content of the jets and thereby aim to constrain the particle composition of the jets.

Acknowledgements

This thesis was supported financially by the NRF/SKA SA Master Scholarship Programme in 2013 and 2014, without which, this project would not have been possible. The University of Cape Town (UCT) has made me stronger in both academic and leadership sense. I believe that I have really grown from my experience at UCT and I would like to thank this institution. These two years of research have changed my perception of science and the universe. I would return thanks to the Australian Telescope Compact Array (ATCA) and their team for granting the request of observing time for the SS433.

I hereby acknowledge and am forever grateful to my supervisors Dr. M. Coriat and Prof. P. Woudt for their supervision, advice and time. I cannot thank them enough for all the knowledge and guidance, the diverse research methodologies, the scientific writing skills, advanced data reduction techniques, and the analytical skills that I have received from them. I am thankful for their trust and encouraging me to be the first author of both papers that will hopefully emerge from this dissertation. I appreciated that Dr. M. Coriat has been supporting me as a good friend as well.

I would like to thank Prof. S. Corbel since the dataset of radio and X-ray observations of BHXBs is provided by him. I would like to thank Dr. A. Tzioumis for his contribution in carrying out the ATCA observations. I would like to thank Prof. R. Fender for his involvement with this project regarding data analysis.

I dedicate my work to my parents, for their moral support and for being there always whenever I needed them. I hope I bring pride to them through my work and achievements. A special thought goes to Marion Bezaud. Lastly, I would like to thank all my friends who have helped somehow in my work. Thank you! :)

Plagiarism Declaration

I, Mr. Avishek Dusoye, understand what plagiarism is. I have not plagiarized any part of MSc thesis and all references therein indicate where the work of others are quoted.

Contents

List of Tables

List of Figures

Chapter 1

Introduction

Most of the stars that exist are actually multiple stellar systems such as binary stars. Within this set of binary stars, there exists a specific subset known as compact binaries which is detailed in Section 1.1. In this chapter, I provide an overview of the various aspects of compact binaries, but more specifically those binary systems which have a black hole as one of their stars. The focus of my dissertation is on two main physical processes that occur in such compact binaries, which are accretion and outflow. The outflow occurs via jets as well as winds in the accretion disc.

1.1 Compact binary systems

Among all of those binaries that exist, there are those specific pairs where one or both members are compact and the orbital period is very short (the binary separation is small). Compact, in this context, means a large ratio of stellar mass to radius. These are called compact binary systems. Examples of stars which are very compact are white dwarfs, neutron stars and black holes. These stars have very strong gravitational fields and can strongly curve spacetime. Ultra-compact binaries are systems with orbital periods that are less than one hour and both stars must be compact. These systems are a laboratory of extreme physical conditions that are not reproducible on Earth and this is what makes them so interesting to study.

Compact binary systems are an active field of research. Essentially, a compact binary is just a two-body problem, where the two members exert a gravitational field on each other and are tidally interacting when they are close enough. Hence they are bound to orbit around a common centre of mass and interact with one another. The left hand side of Figure 1.1[*] shows an example of a close binary and the surface of gravitational influence of each star. The surface of gravitational influence is known as the **Roche Lobe**, which has a teardrop shape due to gravitational and tidal interaction.

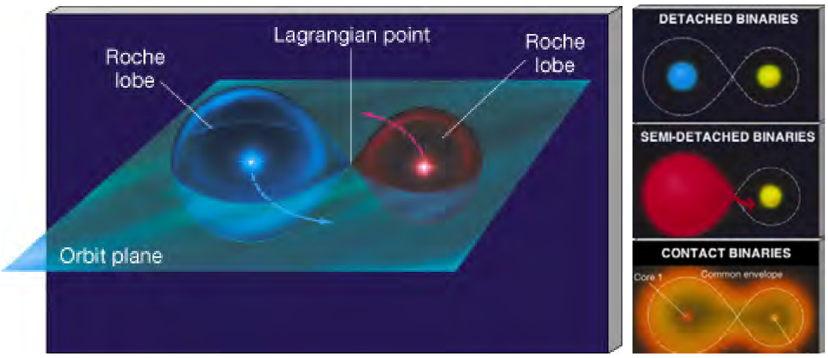

Figure 1.1: Left: Two stars orbiting within a gravitationally bound system; Credit: J. Brau. Right: Different types of binary systems, ranging from detached binaries (top) that don't transfer mass, to semi-detached binaries (middle), and to contact binaries (bottom); Credit: R. Ciardullo.

When two stars are close enough to each other or their gravitational field is strong enough, they are bound to interact. Mass transfer from one star to the other is one of the forms of interaction which can occurs in compact binaries when one of the binary fills its Roche lobe (the size of the star is roughly the size of the Roche lobe). Depending on the levels of interaction, we can classify compact binaries as follows:

(i) **Detached binaries**; where no mass transfer occurs, as shown in top right panel of Figure 1.1 [†]. Examples of classes of semi-detached compact binary are white dwarf/M dwarf binaries or ultra-compact white dwarf/white dwarf binaries (Marsh 2000),

(ii) **Semi-detached binaries**; where the mass is transferred from the main sequence companion star to the compact object as shown in middle right panel of Figure 1.1. Examples of semi-detached compact binaries are Cataclysmic Variables (Warner 1995), X-ray binaries (Tauris & van den Heuvel 2006) and AM CVn system (Nelemans et al. 2009). The latter are ultra compact systems.

---

[*] http://pages.uoregon.edu/jimbrau/BrauImNew/Chap20/FG20_21.jpg

[†] http://www2.astro.psu.edu/users/rbc/a1/lec16n.html

I will not detail contact binaries because I focus on those binaries where one of the component is compact, and contact binaries with a compact components do not exist so far.

These compact binary systems have also been observed with ubiquitous phenomenological features such as accretion discs and jets. The nature and formation of these features are still largely unknown and are being investigated e.g. (Patruno et al. 2014). In addition, these compact objects are known to distort spacetime, and the ultra-compact binaries are a source of gravitational waves. Hence there are many efforts underway to detect those gravitational waves (Sathyaprakash 2013).

1.2 Mass exchange in semi-detached binaries

As mentioned earlier, **semi-detached binaries** are compact binary system where the mass is transfered from a main sequence companion star (donor) to a compact object (accretor). Any star generates its own gravitational field and acts as a potential well.

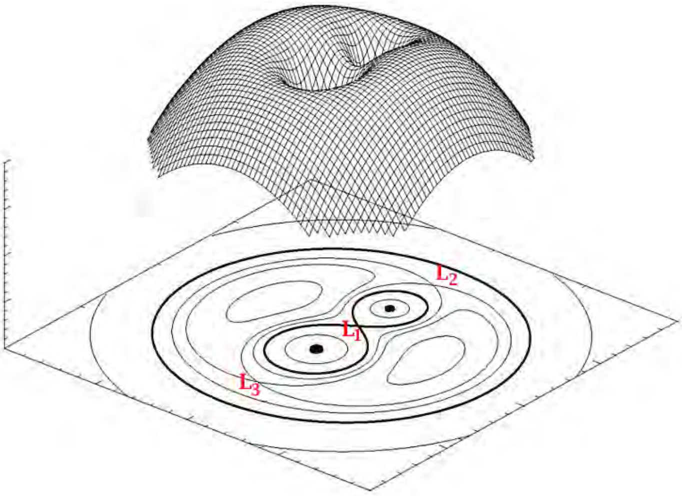

Figure 1.2: A 3D view of the gravitational Roche lobe surface for system where mass of the accretor is twice that of the donor. The plot beneath shows the equipotential lines and the three points at which all forces cancels each other, also known as the Lagrangian points L_1, L_2, and L_3. There is mass transfer from one star to the other via the Lagrangian L-point L_1 only. Credit: M. Van der Sluys.

However, for a two-body configuration of the semi-detached binary, these potential wells are in close proximity. Figure 1.2 * gives us an idea of the gravitational potential surface for such binary system. The contour in this figure show lines of equal potential in this rotating binary frame.

There are three points in this equipotential surface where the forces of the star on the material cancel each other, known as the Lagrangian points L_1, L_2, and L_3. The mass tranfer occurs only at L_1. At that point, the gravitational forces experienced by a stream of mass leaving the donor is equal, both towards the accretor and towards the donor. When this stream of material reaches L_1, it gets pushed by the pressure of the stellar atmosphere from the donor. In this scenario, because the stars are co-rotating, the material moves beyond L_1 to the Roche lobe of the compact object with certain amount of angular momentum. Therefore this stream of mass takes a longer pathway before it gets accreted onto the compact object.

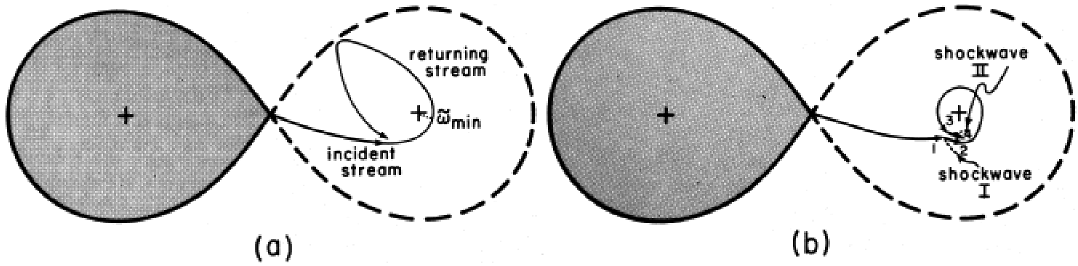

Figure 1.3: The trajectory of a stream and the disc formation for binary stars of roughly same mass. Left panel: The return of a stream to hit the incident stream. Right panel: The turbulent shocks when the returning stream impacts with the incident stream as well as the formation of a steady flow on the outer edge; Image reproduced from Lubow & Shu (1975).

The key parts of this section were derived from Hellier (2000) and Frank et al. (2002) and references therein. As the stream reaches within the influence of the primary, one expects the blobs of material to be orbiting around the central compact object in a very messy and turbulent flow as the stream impacts with itself. Figure 1.3 shows the trajectory of the stream and the disc formation for binary stars of roughly same mass. The left panel shows the return of a stream to hit the incident stream after having reached a minimum distance w_{min} without colliding with the surface of the compact core. Another

---

*http://en.wikipedia.org/wiki/Roche_lobe point that can be noted is that once the stream is within the Roche lobe of the primary, its trajectory is bound within the Roche lobe surfaces. The right panel shows the turbulent shocks that arise when the returning stream strikes the incident stream. At the same time, the stream at the outer edge is forming the steady state flow whereas the stream at the inner edge spirals onto the compact object. Since turbulent shocks dissipate energy, the material settles down in the lowest energy configuration of orbit, which is a circular one. It forms what is called an **accretion disc** (Lubow & Shu 1975).

The accretion disc can be considered of a continuous flow of stream under steady-state until the stream reaches the compact star or simply as a series of annuli of material. As mentioned earlier, the stream does possess certain amount of angular momentum when it enters the Roche lobe of the primary due to the co-rotation of the binary stars. For a blob of material to be accreted by the compact star, it needs to lose its angular momentum while it moves inward to smaller radii. For Keplerian motion, the velocity (v) increases with decreasing radius (r) as $v = \sqrt{\frac{GM}{r}}$. In other words, there is a release of gravitational energy into kinetic energy of the stream when it shifts to inner rings. However, this loss of angular momentum by some accreting streams of material must be counterbalanced by some material moving to outer rings and slowing down, in order to conserve total angular momentum. The overall effect is that the disc becomes thinner and spreads out until the inner edge meets the primary. On the other hand, tidal interaction by the secondary limits the extent to which the outer edge should spread out. The disc is constantly replenished by mass transferred from the secondary maintaining the existence of the disc.

1.3 Black holes in binaries – X-ray binaries

Compact binaries have one or both stars with high compactness (defined by the mass to radius ratio) such as a white dwarf, a neutron star or a black hole as mentioned in Section 1.1. Those semi-detached compact binaries which have a black hole as one of its compact members are known as black hole binaries. Stellar mass black holes (BH) can be observed as bright X-ray sources when they accrete mass from their companions in close binary systems. The accretion rate $\dot{M}_1$ into the disc at the outer edge determines the structure and radiation spectrum of the disc. For a typical value of $\dot{M}_1 \sim 3 \times 10^{-8}\,\mathrm{M}_\odot\,\mathrm{yr}^{-1}$, the disc around the black hole emits strong X-ray radiation and luminosity of $L \sim 10^{37-38}\,\mathrm{erg\,s}^{-1}$ (Shakura & Sunyaev 1973). Such binary systems with a BH are hence termed as **black hole X-ray binaries** (BHXBs).

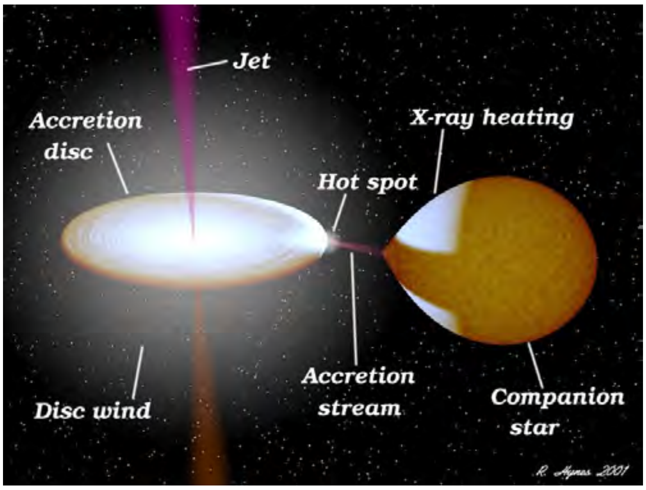

Figure 1.4: A schematic representation of the various components in a typical black hole binary. The binary system consists of a companion star and a black hole which is located at the centre of the accretion disc. There is an illustration of other features such as the jets, the accretion stream, the hot spot and disc wind (see text). Credit R. Hynes.

Figure 1.4 shows a labelled diagram with the various phenomenological features of a typical BHXB. The shape of the companion star is seen distorted as a teardrop shape under the strong gravitational field of the compact object. The black hole lies actually within the accretion disc which emits mostly at X-ray wavelengths. Sections 1.4 details the nature of this accretion disc. There are often associated jets (see Section 1.5 and 1.6) which are more prominent at radio wavelengths. These jets as well as disc winds are the main form of outflows in such binary systems. Figure 1.4 also shows the accretion stream from the companion star and the hotspot which is the spot at which the accretion stream encounters the accretion disc. Lastly, the X-ray emission from the accretion disc get reflected off the surface of the companion star which causes the X-ray heating as shown.

The accreted material in an accretion disc can be said to experience an inward gravitational force as well as an outward force due to radiation pressure.

It is therefore useful to define the Eddington luminosity limit L_{edd}. At this limit, the gravitational forces and the forces due to radiation pressure are equal.

$$L_{edd} = \frac{4\pi G c m_p}{\sigma_T} M_{BH} \,, \tag{1.1}$$

Where G is the Newtonian gravitational constant, c is the speed of light, m_p is the mass of a proton, σ_T is the Thompson cross-section (independent of the frequency of photon), and M_{BH} is mass of the accreting black hole.

The X-ray properties of BHXBs are characterized by their X-ray light curves, timing and spectra. Most of the BHXBs were discovered initially as bright X-ray sources by all-sky X-ray monitors. The flux of X-ray emission varies over all timescales, which may arise due to the Keplerian motion of the system on longer timescale and due to the various instabilities in the accretion disc on millisecond timescale.

X-ray binaries (XRBs) can be grouped into two classes: (i) **low-mass XRBs**, and (ii) **high-mass XRBs**. When the companion star is a star with late spectral type K or M and has mass of less than $2\,\mathrm{M}_{\odot}$, the system is said to be a low-mass XRB (LMXB). The system is otherwise considered as a high mass XRB (HMXB) when the companion star is blue supergiant of spectral type O and B with a mass of $\sim 10\,\mathrm{M}_{\odot}$. In LMXBs, the main form of mass exchange occurs through Roche-lobe overflow of the companion. On the other hand, in HMXBs it is the stellar wind from the companion star that coalesces with the compact star. The left panel of Figure 1.5 shows how wind-driven accretion is the dominant in a typical HMXB, when the companion star is $\sim 16\,\mathrm{M}_{\odot}$ whereas the right panel shows that Roche lobe overflow occurs in a typical LMXBs when the companion star is $\sim 0.6\,\mathrm{M}_{\odot}$.

1.4 X-ray observation of BHXBs

As mentioned earlier in Section 1.3, the accretion disc of BHXBs can be observed as bright X-ray sources when the BH accretes mass from its companion. This section details more about these observations in terms of the X-ray spectra of these systems. The key parts was derived from Remillard & McClintock (2006) and all the references therein. The analysis of X-ray data from 20

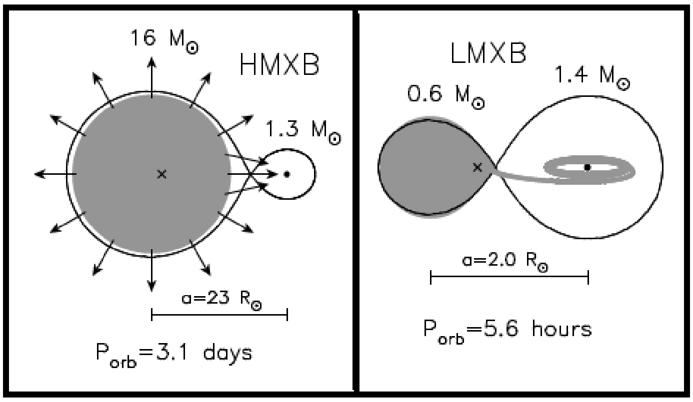

Figure 1.5: The types of the accretion mechanisms in LMXBs and HMXBs; Left panel: Wind-driven accretion which occurs mostly in HMXBs. Right panel: Roche lobe overflow which occurs in LMXBs; Image reproduced from Tauris & van den Heuvel (2006).

BHXBs revealed that most of the outburst of BHXBs last between 20 days and many months (Chen et al. 1997). These recurrent outbursts are caused by an instability in the accretion disc and happens to reccur on timescales of 1 to 60 years. Whenever the mass losses from the donor star differ from the accretion rate onto the compact object, there is a discontinuity in the viscous flow and the accreting matter fills the external annuli of the disc up to the point that surface density reaches a critical value above which the hydrogen starts to ionize. The viscous properties of the flow change and an outburst is then initiated (Lasota 2001).

The X-ray spectra of BHXBs are known to consist of two main components:(i) thermal and (ii) non-thermal*. The observed spectrum, however, happens to vary where one component may dominate the other depending on the emission state of the BHXB. The thermal component arises from thermal blackbody radiation from inner annuli of the accretion disc, in which the *viscosity* plays an important role in maintaining the conservation laws of angular momentum and energy. The Shakura and Sunyaev accretion disc model (SSD), behaves like a multi-temperature blackbody system, where the temperature profile for a disc of radius R is given by $T(R) \propto R^{-3/4}$,

---

*__non-thermal__, in this context, only refers to the shape of the spectrum that is not blackbody-like. However, it doesn't necessarily imply that the energy distribution of the underlying radiating particles is non-thermal. Indeed, one of the possible mechanism for explaining this spectral component is thermal Comptonization.

(Shakura & Sunyaev 1973). For a typical inner radius of an accretion disc around a black hole, the thermal spectrum peaks at 1 keV (see Figure 1.6).

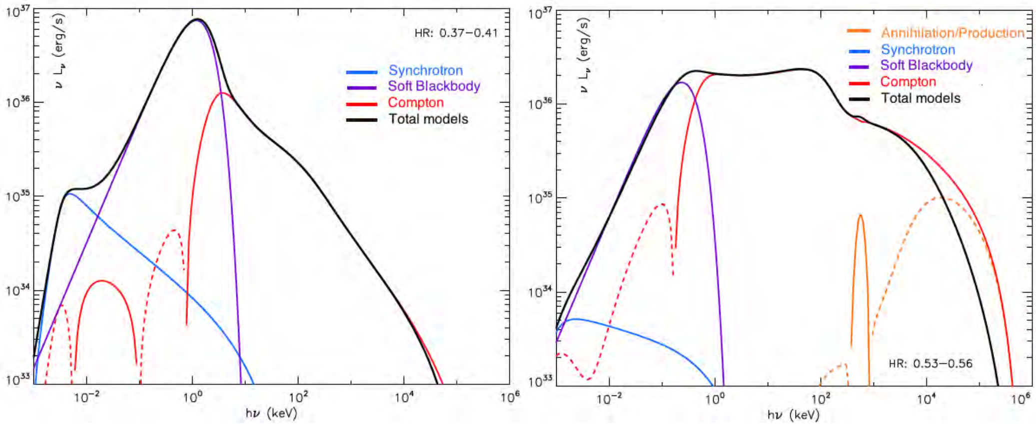

Figure 1.6: The continuum spectra of Cygnus X-1. The various colour lines are for total models (black), soft blackbody radiation (purple), Compton emission (red) and annihilation/production (Orange). Left panel: Thermal components are dominant. Right panel: Non-thermal components are dominant; Images reproduced from Del Santo et al. (2013).

The non-thermal component of the spectrum arises from radiative processes such as synchrotron emission and/or inverse Compton scattering. Such a spectrum is often modelled by a power law of the form of $S(\nu) \propto \nu^{-\alpha}$. These power law spectra can extend up to hard X-rays ($\sim 500\,\mathrm{keV}$) as compared to the thermal spectrum.

Additionally, one can observe (i) a disc-reflection component which appears as a spectral bump at high energy, depending on the inclination of the system, see e.g. Madej et al. (2014) (ii) Fe relativistically broadened emission lines at 6.4 keV, see e.g. Zhang et al. (2002), and (iii) the absorption lines due to presence of local hot gas.

The consistent observations of one particular source reveal the drastic spectral changes which occur over the course of an outburst and how these spectral changes are correlated to the accretion disc states of the BHXB system. It appeared as a convention, after the observations of such spectral changes in Cyg X-1 (Tananbaum et al. 1972) and other sources, to define *X-ray emission states*. Several spectral states have been identified based on the relative strengths and properties of the different X-ray emitting components, see e.g. Homan & Belloni (2005); Remillard & McClintock (2006). The two main spectral states

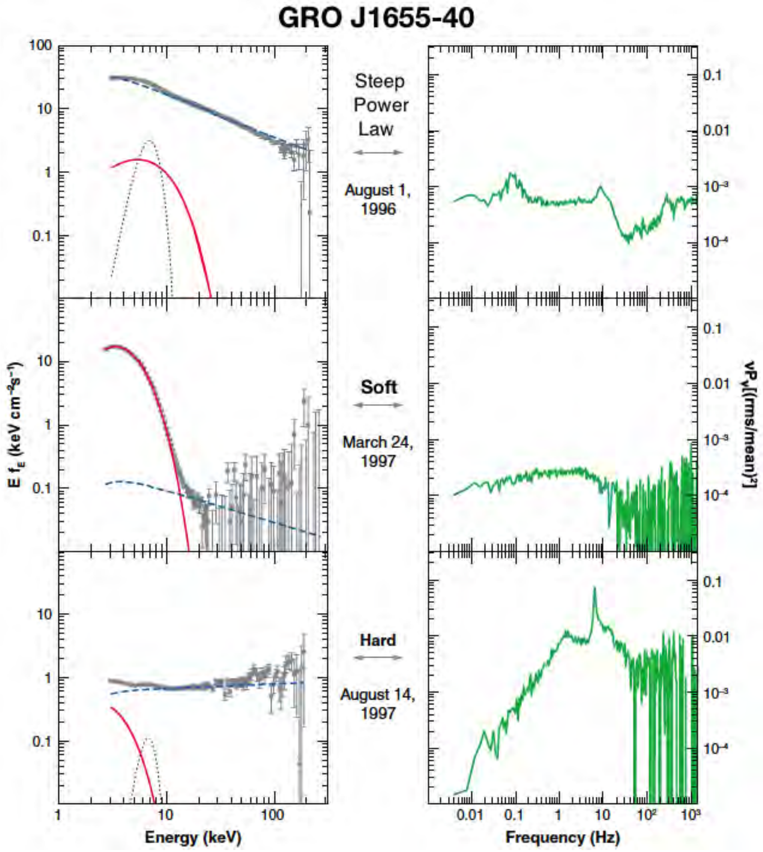

Figure 1.7: X-ray spectra (left column) and power density spectra (right column) for three different X-ray states of the BHXB GRO J1655-40. The three X-ray emission states are called steep power law (top), soft (middle), and hard (bottom); Image reproduced from Remillard & McClintock (2006).

are the **soft state**, dominated by thermal emission from the accretion disc, and the **hard state**, dominated by the non-thermal spectral component. Various instances (hard or soft) of the intermediate state have also been defined to describe the transition phases between the two main states. During these phases, the X-ray spectra have comparable contributions from the thermal and non-thermal components, see e.g. Van der Klis (2006) and Belloni (2010) for a review. Figure 1.7 shows typical X-ray spectra associated with each emission state. In the soft state, the flux is dominated by the thermal component from the inner accretion disc. The non-thermal component has a small contribution of $< 25\%$ of the flux detected at 2-20 keV. On the other hand, in the hard state, the flux is mainly 80% of the power law component in that same 2-20 keV range.

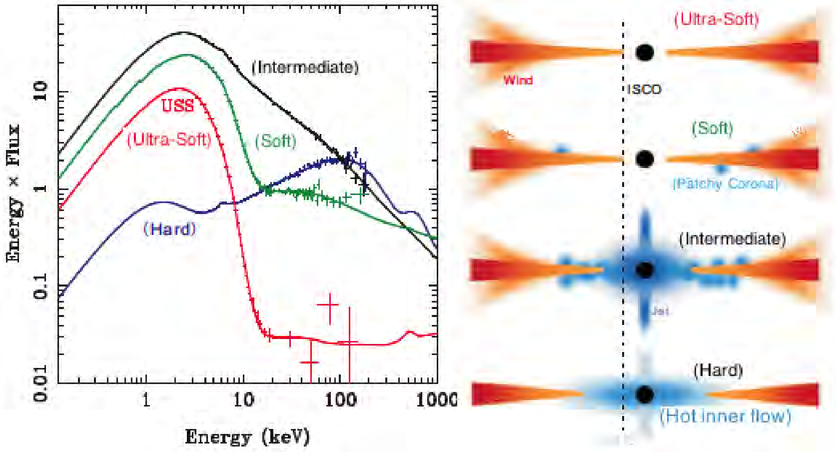

Figure 1.8: Left panel: Spectra in different states for GRO J1655-40; Right panel: Proposed accretion flow structures in these diferent spectra; Image reproduced from Done et al. (2007).

The nature of the accretion disc at the inner edge is expected to be different from outer edge since the conditions experienced by the inner annuli are affected by extreme physics as we approach the event horizon of the accreting BH. The hard X-ray emitting component is often referred to as the ‘corona’. One of the possible explanations for the presence of the non-thermal component is that the standard disc (which is optically thick and geometrically thin) is replaced in its inner region by a geometrically thick and optically thin accretion flow that we call **advection dominated accretion flow** (ADAF).

The different X-ray states can be described by the relative extent of the ADAF with respect to the outer thin disc, see Narayan & Yi (1995), and (Liu et al. 1999) for details. The origin of these different observed states in the BHXBs could be due to the interaction of the thermal cool disc and the hot accretion flow. The left panel of Figure 1.8 shows the various spectra that correspond to the different X-ray emission states for GRO J1655-40. The right panel in Figure 1.8 shows the interplay between the hot inner flow (HIF) and the thermal cool disc.

1.5 Jets in X-ray binaries

The manifestation of ‘jets’ or relativistic outflows extends for systems over a wide mass-scale ranging from star formation to active galactic nuclei

(AGN). These jets are known to represent powerful flows of energy and matter. So far, no jets have been observed independent of accretion processes and it seems that these jets are somehow related to the existence of an accretion disc. This connection between the accretion process and the jets is still being investigated in all accreting systems, including X-ray binaries (see Section 2.1). Apart from this intriguing connection between jets and discs, many additional reasons motivate the study of jets. They are indeed an ideal laboratory of high energy phenomena where particle acceleration mechanisms and physics in strong gravitational field can be investigated.

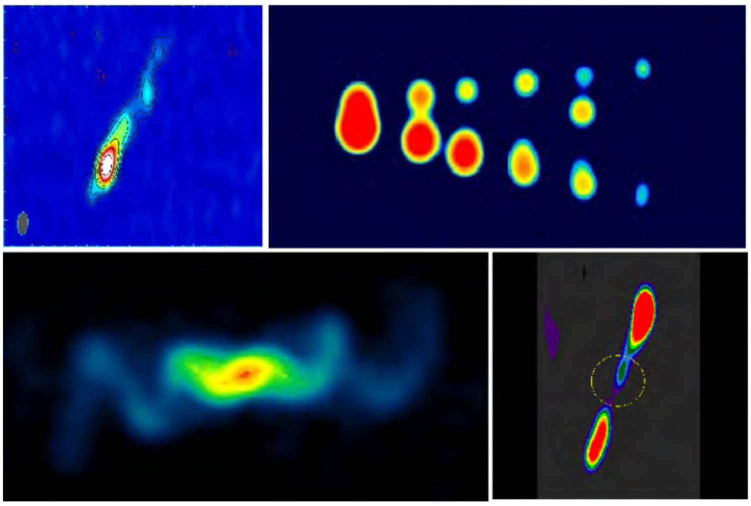

Figure 1.9: Radio observation of jets at various scales; Left: The jets in HMXBs with Cyg X-1 at the top (Stirling et al. 2001) and the precessing jets of SS433 at the bottom (Blundell & Bowler 2004); Right: The Galactic jet sources with GRS 1915+105 (Mirabel & Rodriguez 1994) at the top and 1E 140.7-2942 at the bottom (Mirabel et al. 1992).

There are many unanswered questions regarding astrophysical jets in XRBs which includes the following: (1) the launching mechanism and formation of the jets, (2) the composition of jets (see Section 1.7.4), and (3) the energetic content of the jets. Astrophysical jets can be considered as two different types which are (i) transient ejections or discrete jets, e.g GRS 1915+105 (see top right panel of Figure 1.9) (ii) compact jets, e.g Cyg X-1 (see top left panel of Figure 1.9). The discrete jets can extend up to few arcsecs and can be ballistic as well as superluminal, e.g. GRS 1915 +105 (Wardle et al. 2011) and GROJ655-40 (Tingay et al. 1995). On the other hand, compact jets are a continuous and relatively steady flow of matter with a typical angular size scale of a few milli-arcseconds.

1.6 Physical properties of jets

In this section, I review the relevant physical properties of jets (with a focus on X-ray binaries) such as emission mechanism, energetics, composition, orientation and precession. This will provide only a general overview of jets properties. More details can be found in Fender (2006) and references therein.

1.6.1 Emission mechanism

The high brightness temperatures, non-thermal spectra (Shahbaz et al. 2013) and polarization properties (Russell & Shahbaz 2013) indicate the synchrotron emissions in the jets. Discrete jets have optically thin synchrotron emission and produce radio spectra decreasing with frequency whereas compact jets produce self-absorbed synchrotron emission which are detected as nearly flat spectra from radio to infrared wavelengths.

Medium	**Optical Depth** $< \tau_\nu >= \alpha_\nu l$	**Intensity**
Optically thin	$\ll 1$	$I(\nu) \propto j_\nu \sim \nu^{-\alpha}$
Optically thick	≥ 1	$I(\nu) \propto \frac{j_\nu}{\alpha_\nu} \sim \nu^{+5/2}$

Table 1.1: The form which the intensity of the synchrotron radiation I_ν can take according to the optical depths of the jet material. α_ν and j_ν are the effective absorption coefficient and emissivity coefficient respectively. This table was derived from (Kembhavi & Narlikar 1999).

Table 1.1 gives the form that the intensity of the synchrotron radiation I_ν can take depending on the optical depth of the jet material. The synchrotron emission from a power law distribution of electrons in the form $N(E)dE \propto E^{-p}dE$, where $N(E)$ is the number density of particles having an energy E and particle index p, will produce a power law spectrum of the form $I_\nu \propto \nu^{-\alpha}$. Here I_ν is the total intensity, ν is frequency, and α is the spectral index. In that case, the relation between p and α is $p = 2\alpha + 1$. Therefore one can estimate the particle distribution index by measuring the spectral index observationally.

For example, the spectral indices of AGN jets are usually observed in the range of $0.4 \leqslant \alpha \leqslant 0.8$ which correspond to $1.8 \leqslant p \leqslant 2.6$ (Kembhavi & Narlikar 1999).

1.6.2 Orientation and precession

The orientation of a steady jet is the direction in which its content seems to moving out. The left panel in Figure 1.10 gives us an illustation how we can get this sense of direction, for the position of the jets through the angle θ_1, and for the position of disc through the angle θ_2. Both angles θ_1 and θ_2 are expressed relative to the line of sight of observer. It is usually assumed that the jet axis is perpendicular to the orbital plane of the BHXB. However, it should be noted that some X-ray binaries (e.g. GRO J1655-40 and V4641 Sgr, see Maccarone (2002)) have shown significant misalignment between the jets and the disc.

On the other hand, the precession of a jet is more complex as it entails the outflow with a constant change in its inclination relative to the disc (as in a spiral or corkscrew). The most famous and confirmed X-ray binary known to exhibit precession of its jets is SS433 (see right panel in Figure 1.10), with a precession period of 163 days. The jet's intrinsic speed is $\sim 0.26c$ within a cone opening angle $\sim 20^\circ$ and an inclination of the precession axis to the line of sight of $\sim 80^\circ$.

A plausible explanation towards the precession of jets is disc warping. The mechanism behind the precession of a tilted disc is due to the tidal forces arising from the secondary (Katz 1973). The disc can be considered as a series of annuli which are actually tilted to the plane of the binary system. The rings can have two rotational degrees of freedom owing to their rapid rotation (like a gyroscope). The rings is assumed to interact with each other as well. In that scenario, the rings should hence precess retrogradely under the effect of the tidal torque about an axis perpendicular to the plane containing the two stars. This rate of precession is pre-determined by the radius of the annuli. This creates a rapid curling of the accretion disc. However, the accretion disc which is of fluid nature, will oppose this twisting motion by generating its own internal torque between adjacent annuli. Although one can theoretically reset the parameters so as to obtain a net torque on each ring with constant rate of precession. This would have lead the disc to precess in coherence. However, the internal torque can only be generated by curling (warping) the disc. A required mechanism to maintain this tilt continuously is through radiation-driven warping (Ogilvie & Dubus 2001).

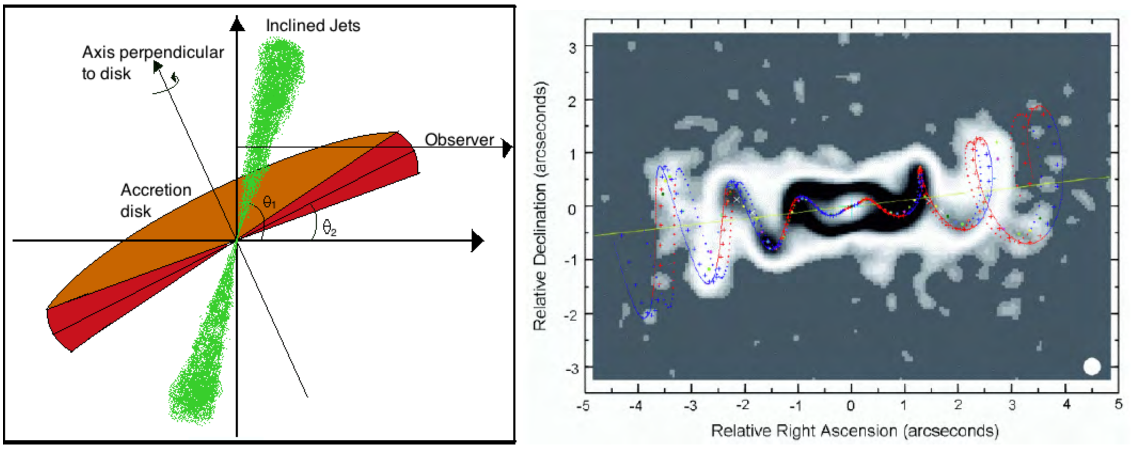

Figure 1.10: Orientation and precession of jets; Left panel: Schematic view of an inclined jet to the accretion disc as seen by the observer. Right panel: Models track of kinematics in form of corkscrew for SS433 (Panferov 2011), being superimposed on an arsec-scale VLA image; Image reproduced from Blundell & Bowler (2004).

1.6.3 Composition of X-ray binary jets

The particle content or composition of jets for most accreting systems including X-ray binaries is still unknown. The composition of these jets are actively investigated because it has major consequences on jet formation mechanism and the role of BH spin in powering the jet. Since one of the canonical jet formation mechanisms (the Blandford- Znajek (BZ) mechanism; Blandford et al. (1977)), involves the rotation power of a black hole, it certainly cannot operate in all systems. An alternative is the Blandford-Payne (BP) mechanism (Blandford & Payne 1982), in which the required rotation power comes from a rotating accretion disc. As a consequence, one expects BP jets to be baryonic, since they are magnetocentrifugal outflows from a gaseous reservoir. BZ jets, on the other hand, might be electromagnetically dominated.

The jet plasma composition have been identified from synchrotron emission to be either **leptonic** (e^- and e^+) pairs as in GX 339-4 (Vila & Romero

2010) or **baryonic** (e^- and p^+) pairs as in 4U1630-47 (Díaz-Trigo et al. (2013) and Neilsen et al. (2014)) and also SS433 (Margon et al. 1979), whose jets exibit various emission lines (hydrogen, helium, nickel, and even iron) in their optical, infrared and X-ray spectra (see Figure 1.11). The presence of baryons in 4U1630 is nevertheless still highly debated.

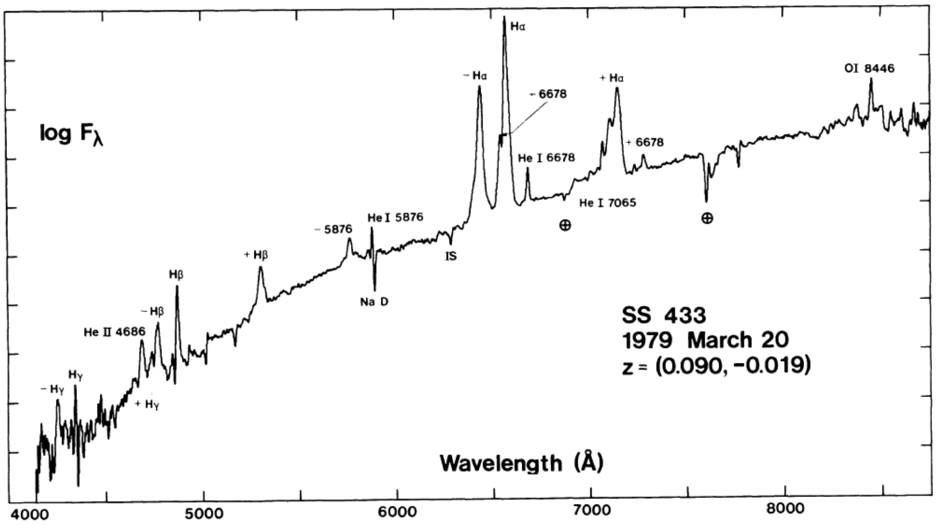

Figure 1.11: The spectrum of SS433. The emission lines that has been identified in the jets are due to the enormous Doppler shift. The prefix (+) and (-) denotes redshift and blueshift respectively. Strong interstellar absorption features are identified as IS; Image reproduced from Margon et al. (1979).

In addition, the accreting stellar-mass black holes appear to produce two different kinds of jets (steady and transient) as mentioned in Section 1.5. Observationally, it remains unclear whether these two types of jets correspond to the two mechanisms described above; a suggested association between the transient jets and the BZ mechanism has been hotly debated (Fender et al. (2010), Narayan & McClintock (2012), Steiner et al. (2013) and Russell et al. (2014)). Different processes may launch jets at different scales or under different conditions, but because a jet's energy requirements are sensitive to its baryon content, these considerations have broad and concrete implications for radio-mode feedback from accreting systems (Fender 1999). Until recently, SS433 stood alone as the only system with a clear detection of baryons in the jet.

A methodology of constraining the composition of jets is to analyse the energetics of their relativistic outflow, which is associated with the ejection of a population of ‘cold’ protons. Fender & Pooley (2000) has applied this technique to GRS 1915+105. The mass outflow rate and the amount of energy could be estimated under several assumptions. The estimated power (averaged over time) which is required to produce the observed synchrotron emission seems to have a lower limit of $3 \times 10^{38}\,\mathrm{erg\,s^{-1}}$. This power therefore needs to accelerate the proton population up to bulk Lorentz factor of $\Gamma \simeq 5$. This is so large that either the ejection of plasma in the jets of GRS 1915+105 was probably at considerably lower bulk Lorentz factor or did not have a large baryonic component.

A different approach to contrain the particle composition is through circular polarization. The origin of circular polarized emission is still unclear but there are four suggested mechanims: (i) coherent radiation, (ii) scintillation, (iii) intrinsic circular polarization, and (iv) Faraday conversion (Wardle & Homan 2001). Circular polarization has already been detected in few X-ray binaries, such as SS433 (Fender et al. 2000), GRS 1915+105 (Fender et al. 2002) and GRO J1655-40 (Macquart et al. 2002). In chapter 3, I shall detail and investigate further the circular polarization of SS433 in order to constrain the composition of its jets through this method.

1.7 Disc-jet coupling of BHXBs

The link between the jets and the accretion disc, also referred as *disc-jet coupling*, remains one of the most intriguing areas of research as it extends to the general relation between inflow and outflow of matter in the universe. This coupling manifests itself from AGNs to a range binary systems and down to star formation.

The spectral energy distribution (SED) of a typical BHXB system over the whole electromagnetic spectrum is shown in Figure 1.12. Different components of a BHXB such as the jets, the accretion disc, the corona and the companion star appear more pronounced in different wavelength domains. Therefore the simultaneous observations of a BHXB at multiple wavelengths helps us to understand better the connection between inflow and outflow of matter. I shall detail and investigate further on the disc-jet coupling through this method in Chapter 2.

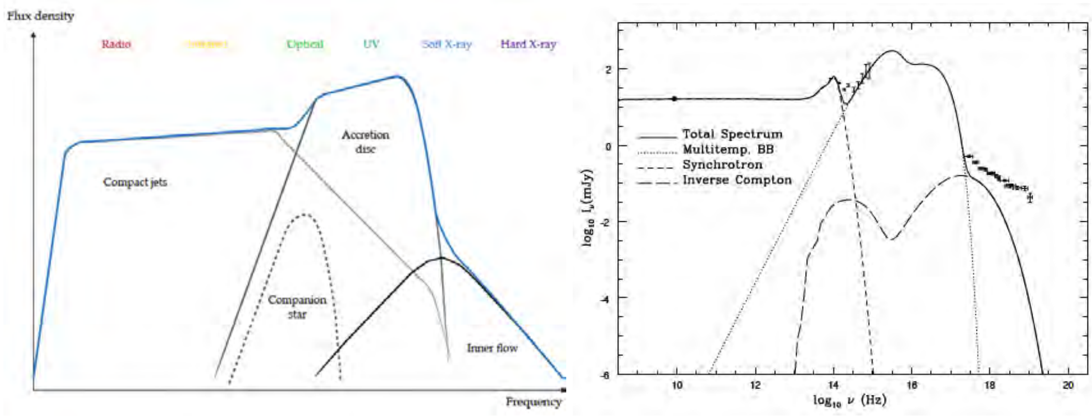

Figure 1.12: Left: Schematic representation of the spectrum of a typical BHXB in the hard state. The jets are more pronounced at radio wavelength while the thermal emission from the accretion disc dominates the optical to X-ray domain; Adapted from Coriat (2010). Right: A broadband jet-model fit to GX 339-4 datasets (dated 1981). The image was reproduced from Pe'er & Markoff (2012) and Markoff et al. (2003).

The nature of the flat spectrum which originates from the compact jets in Figure 1.12 are due to a series of self-absorbed synchrotron events. The jets can be considered as successive regions of plasma perpendicular to the propagation of the jets. The different plasma regions emit self-absorbed synchrotron at different frequencies, because the energy density of each plasma region decreases over propagated distance. The energy losses are due to the observed adiabatic expansion of the plasma region and synchrotron emission. The resulting spectrum extend from optical down to radio. Similarly, the flatness of the spectrum for the accretion disc in Figure 1.12, arises due to the superposition of multi-temperature blackbody spectra (using the Shakura and Sunyaev accretion disc model). This extends from the infrared (corresponding to the outer disc edge) to soft X-rays (corresponding to the inner disc edge). Most of the energy is emitted in X-ray, which is due to the hot inner region.

As mentioned earlier in Section 1.4, black hole binaries exhibit several X-ray states, which are defined by their hardness and emission from the inner corona. Figure 1.13 below shows how the different X-ray states can be represented on a hardness/intensity diagram and also summarizes the evolution of the BHXB system. The hardness ratio, in this context, is defined as a measure of the steepness of the X-ray spectrum. The key parts of this section were derived from Fender & Belloni (2012).

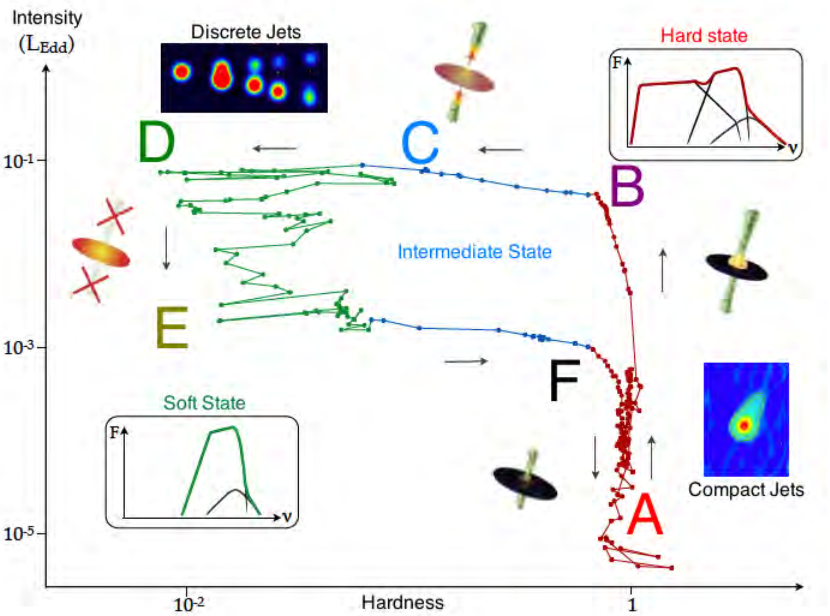

Figure 1.13: Hardness-Intensity diagram for GX 339-4 during its outburst in 2007. Image reproduced from Coriat (2010).

The sudden rise/decay in luminosity is correlated to the change in spectral state and the morphologies of the different components (jets, corona, and accretion disc) of the BHXB system. Despite that, multiple outbursts of the same source do show a few variations in their cyclic evolution. These patterns on the hardness-intensity diagram can be generalized for essentially all BHXBs. The different phases are illustrated below:

1. **In the rising phase of an outburst (A → B)**
   Most of the BHXBs, having a luminosity below 1% L_{edd}, are in their quiescent hard state (point A in Figure 1.13). L_{edd} is the Eddington Luminosity as mentioned at Equation 1.1 in Section 1.3. However, the system still remains in the hard state where the X-ray spectrum is characterized by a high energy tail extending up to 100 keV probably due to inverse Compton scattering of photons by the electrons from the hot corona. The geometry of the corona is not clearly understood. When the BHXB appears at its brightest peak (point B in Figure 1.13), a blackbody spectrum component can be detected near soft X-rays ($\sim$ 1 keV) down to

UV, probably from the geometrically thin and optically thick accretion disc. The rapid variability features, known as Quasi-Periodic Oscillation (QPO), seems to decrease which may correspond to changing viscosity. The flat spectrum synchrotron emission from jets are prominent from the radio to near infrared (Fender et al. 2001). This implies that the jets are observable and present in the hard state during outbursts. In this state, we also observe a non-linear correlation between the radio emission and X-ray emission (Gallo et al. 2012). We shall discuss this more in the Chapter 2.

2. **Hard to soft spectral transition (B → C → D)**
   Once the BHXB system peaks in luminosity with 10% to 50% L_{edd} (point B in Figure 1.13), spectral changes can be observed (Fender et al. 1999). The hard X-ray component starts to steepen and decrease in luminosity. At the same time, there is an increase in flux of the blackbody emission from the accretion disc. This high luminosity is maintained (point C in Figure 1.13) as the spectrum shifts to softer X-rays. The characteristic frequencies of variability increases until replaced by one strong single QPO. The observed variation in infrared and radio emission indicates that jets change from being compact to discrete (Russell et al. 2011). This was confirmed by high resolution observation of discrete radio or X-ray blobs, moving away from the core (see Corbel et al. 2005, Mirabel & Rodriguez 1994, and Corbel et al. 2002). Then at point D in Figure 1.13, a decay of luminosity can be observed, and the BHXB system enters in the soft state.

3. **Soft state (D → E)**
   A gradual decay of luminosity is observed in the soft state, which can take over a few weeks. There are still changes in the spectra e.g. the strong QPO disappears with almost no X-ray variability. There is no detection of radio emission in this state, suggesting the absence of jets (see Fender et al. 1999 and Fender et al. 2009). The X-ray spectrum is dominated by the thermal accretion disc component despite of weak high energy tail ($\sim$ 1 MeV). Sometimes, the BHXB persist on maintaining a constant luminosity for a week or more before slowly declining in intensity and

this indicates that the accretion rate onto the BH has started to drop. The presence of a strong accretion disc wind is also detected. When the BHXB has declined in luminosity by few orders of magnitude and can no more remain in the soft state, the BHXB is at point E in Figure 1.13.

4. **Transition back to hard state (E → F)**
   As the accretion rate starts to fall, the BHXB system transits back from the soft state to the hard state. There has never been a source with $< 1\%$ L_{edd} which is detected in soft state so far (Maccarone 2003). When the source reaches the canonical hard state again, all the initial features such as presence of compact jets reappear (point F in Figure 1.13).

This empirical pattern seems to be well-established and observed in about 30 systems so far, with few exceptions. This cycle of activity summarizes the behaviour of these BHXB systems and how the BH responds whenever there are changes in accretion rate by liberating the gravitational potential energy in different forms and to different extents (jets and winds).

Chapter 2

Radio/X-ray correlations

In this chapter, I study the general properties of black hole X-ray binaries by taking a large sample of 17 known BHXBs (see Table 2.1). Among the various properties, I focus specifically on the nature of the disc-jet coupling in BHXBs by studying the correlation between X-ray luminosity (related to accretion disc) and radio luminosity (related to jets). The problem I investigate here is to explain the existence of dual correlations (corresponding to two populations of BHXBs).

2.1 Brief history

Each component of a BHXB (accretion disc, jets, corona) dominates a specific frequency range, giving rise to the spectrum as we saw earlier in Figure 1.12 (Markoff et al. 2003). The jets and accretion disc appear pronounced in radio and X-ray respectively. Therefore an approach to investigate the connection between jets and accretion disc for these BHXBs is to study the correlations between radio and X-ray emission, which should be observed quasi-simultaneously.

In 2003, during the hard state of GX 339-4, a very strong correlation was discovered between radio fluxes at 8.6 GHz using the Australian Telescope Compact Array, and X-ray fluxes in the band 3-20 keV using the the Rossi X-ray Timing Explorer and BeppoSAX (Corbel et al. 2003). This correlation takes the form of a power law:

$$F_{rad} = \kappa \times F_x^b \ , \tag{2.1}$$

$$\log F_{rad} = b \log F_x + \log \kappa \ , \tag{2.2}$$

with $\kappa = 1.721 \pm 0.035$, $b = 0.706 \pm 0.011$ (Corbel et al. 2003), and where F_{rad} means radio luminosity and F_x means X-ray luminosity. Such a correlation suggests a connection between the X-ray emitting accretion disc and the radio jets. Let us consider for example when the X-ray luminosity of the accretion disc is expected to escalate during an outburst. This correlation helps us to understand how the radio luminosity of the jets is expected to increase and therefore describe the extent of flaring during the same rise time. In other words, the behaviour of both components (jets and accretion disc) is related through Equation 2.1.

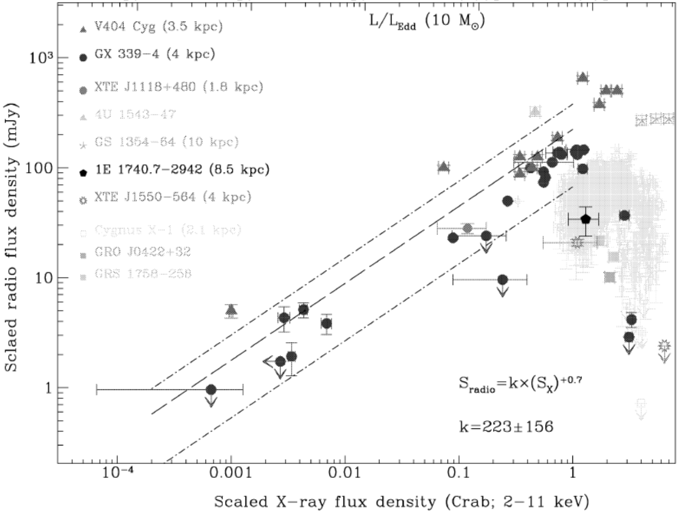

Figure 2.1: Radio luminosity against X-ray luminosity for a sample of 10 BHXBs; The correlation between the radio luminosity and the X-ray luminosity for most of the 10 BHXBs in the hard state seems to be consistent with a power law slope of $b \simeq 0.7$. This suggested a universal correlation which could imply that most BHXBs shall behave similarly in terms of disc-jet coupling. Image reproduced from Gallo et al. (2003).

The validity of this correlation was extended to a larger sample of 10 BHXBs (see Figure 2.1; Gallo et al. (2003)). This suggested that most BHXBs will tend to have similar behaviour regarding their disc-jet coupling. Therefore

Gallo et al. (2003) proposed a universal correlation which would be valid for any BHXBs in the hard state under the hypotheses of (i) common disc-jet coupling in these BHXBs and (ii) isotropic X-ray emission.

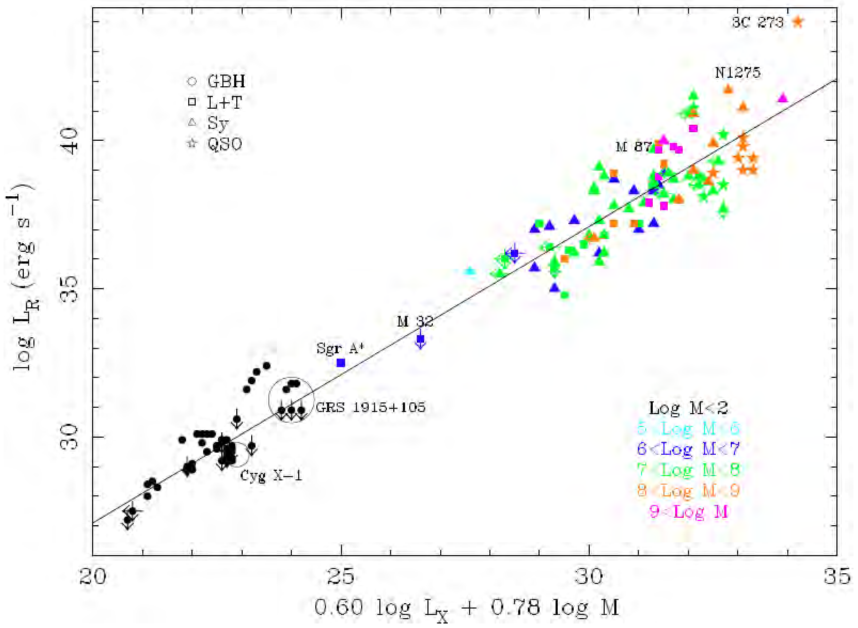

Figure 2.2: The fundamental plane of BH activity (edge on view); This explains how the three parameters radio luminosity L_R (erg s^{-1}), X-ray luminosity L_X (erg s^{-1}) and mass scale depend on each other. The multivariate fit to the entire dataset indicates that the validity of the universal correlation is maintained even at a larger mass scale. Image reproduced from Merloni et al. (2003).

The work was extended then to larger mass scale using a compiled sample of 100 Active Galactic Nuclei (AGN) with supermassive BHs and 8 galactic BHXBs (Merloni et al. 2003). The parameters considered for the AGN were similar to BHXBs. However, in addition to the radio luminosities L_R (erg s^{-1}) and X-ray luminosities L_X (erg s^{-1}), the mass of the BH (M$_\odot$) has been taken into account to study the correlation, as it cannot be ignored anymore when comparing stellar mass BHs and supermassive BHs. The results of Merloni et al. (2003) seems to indicate the AGN behave very similarly to BHXBs when it comes to disc-jet coupling. Equation 2.3 is a general form of Equation 2.2 when the mass scale is considered,

$$\log L_R = (0.6^{-0.11}_{+0.11}) \log L_X - (0.78^{-0.11}_{+0.09}) \log M_{BH} + 7.33^{+4.05}_{-4.07} \, . \qquad (2.3)$$

Since the value of $b \simeq 0.7$ in Equation 2.2 is within the range of values of the coefficient for the first term in Equation 2.3, the validity of the universal correlation at a even larger mass scale seems to be maintained. This led to the definition of the fundamental plane of (hard state) black hole activity (Figure 2.2). Plotkin et al. (2012) improved on the original work of Merloni et al. (2003) to obtain the refined Equation below describing the fundamental plane of BH activity. The latter used the reciprocal Equation 2.4:

$$\log L_X = (1.45 \pm 0.04) \log L_{Radio} - (0.88 \pm 0.06) \log M_{BH} - 6.07 \pm 1.10. \quad (2.4)$$

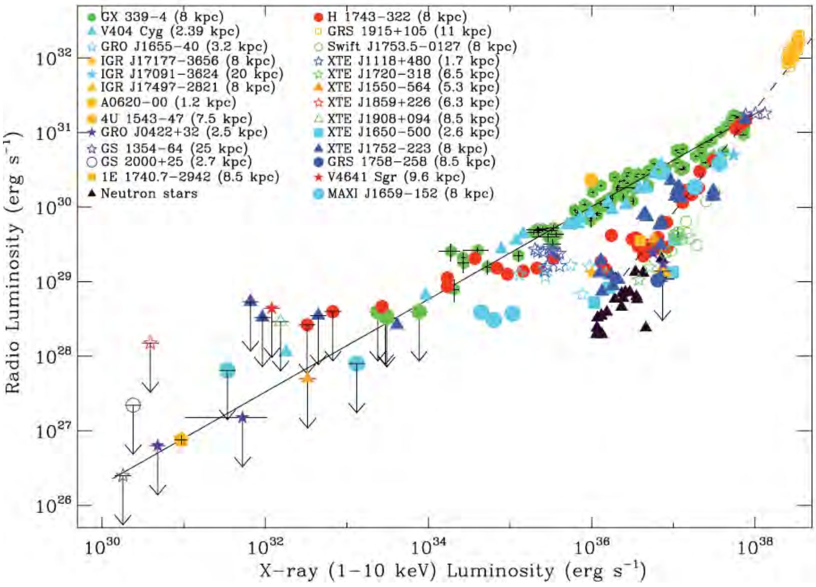

Figure 2.3: The existence of a dual track on the Radio/X-ray correlation diagram; The upper standard track has a correlation index (slope) $b \sim 0.7$ whereas the outlier's track has a steeper index (slope) $b \sim 1.4$. This could be indicative of two modes of disc-jet coupling. Image reproduced from Corbel et al. (2013).

Over the past ten years, many BHXBs have been detected with jets of lower luminosity when compared to what is predicted by the previous correlation (Equation 2.1) for the same X-ray luminosity (accretion-powered). Therefore this suggests that BHXB may have either a large range of jet power or a large range of X-ray luminosity for similar accretion rates. More and more BHXBs in outburst have indicated to be located below the standard universal correlation. The few examples include XTE 1650-500 (Corbel et al. 2004), IGR J17497-2821 (Rodriguez et al. 2007) and Swift J753.5-0127 (Soleri et al.

2010). Given the fact that another population of BHXBs seems to situated off from the standard correlation, these sources are referred as "Outliers".

Statistical evidence has been provided by Gallo et al. (2012) to "dismiss the existence of a single universal correlation between the radio and X-ray luminosity of hard and quiescent state BHXBs". Corbel et al. (2013) updated the radio/X-ray correlation plot with the new data set of GX 339-4 and some additional sources as shown in Figure 2.3. The correlation index of $b \sim 0.7$ still remains consistent for the standard correlation on the updated plot. For the outliers, Coriat et al. (2011b) found a steeper correlation with index of $b \sim 1.4$, using a large sample of observations for H1743-322. This could be indicative of two modes of disc-jet coupling instead of only one. It was also proposed that either there could exist a large number of the hard-state BHs which are radiating efficiently which appear as the outliers, or the steep correlation index for the outliers may correspond to a different coupling between jet power and mass accretion rate.

2.2 Definition of the problem

The existence of dual correlation tracks completely turns down the original paradigm of the scale-invariant and universal accretion disc jet coupling model. Since this discovery, *a key question is to explain the existence of the two tracks*. One school of thought proposes that black holes with the same accretion inflow, can undergo outflows which can vary over a large range of power. This suggests that some parameters of the BHXBs are actually adjusting the mode of accretion disc-jet coupling. The BH is characterized by three parameters which are its mass, spin and charge. The charge is considered unimportant since the BH is electrically neutral on average on a macroscopic scale. In addition, there are also parameters in a binary system such as orbital period, Roche lobe size and inclination which could be a factor. Therefore there is a need to constrain those possible parameters in order to understand a plausible explanation for these two tracks.

The radio normalisation (parameter "κ" in Equation 2.1) serves as an indicator of the position of a source on the radio/X-ray correlation diagram. Sources following the upper (lower) track usually have a high (low) normalisation. By investigating the relations between the radio normalisation of a sample of sources with any of the parameters mentioned above, one can study the influence of this parameter on the dual track issue.

Fender et al. (2010) show evidence for no correlation between the radio normalisation and BH spin assuming the measurements are correct. The spin of the BH therefore does not influence the BHXB to be on either of the two tracks. Figure 2.4 shows the correlation diagrams for the BH spin and radio normalisation. The spin was measured by two methods, either by reflection fits (left panel) or by disc fits (right panel). In both cases, there is no correlation.

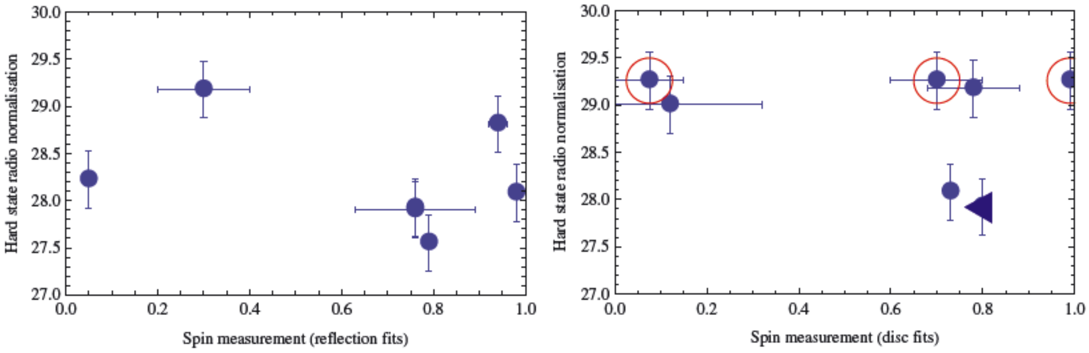

Figure 2.4: Correlation diagram between BH spin and radio normalisation; The spin measurement are obtained by two methods, which are (i) reflection, and (ii) disc fits. In both cases there is no correlation. This implies that the spin is not the parameter that determines the position and track of the source on the radio/X-ray correlation diagram. Image reproduced from Fender et al. (2010).

Similarly, Soleri & Fender (2011) have investigated the other fixed binary parameters such as orbital period, accretion disc size, and inclination for 17 BHXB systems. Figure 2.5 shows the inclination of the BHXBs to line of sight of the observer against the radio normalisation. Figure 2.6 composes of the Roche lobe size and the orbital period of the binary system in relation to radio normalisation. In all cases, no evidence for a correlation between these parameters and the radio normalisation has been found. This suggests that they do not play a clear role in the existence of the two correlation tracks.

In the following, I investigate whether the BH mass can determine the track a BHXB follows on the radio/X-ray correlation diagram. Similar to the previous research methodogies, I would use the radio/X-ray normalisation for this investigation. Futhermore, I review the dependence of binary parameters (orbital period and inclination) as in Soleri & Fender (2011) for our sample of BHXBs which includes recently monitored sources.

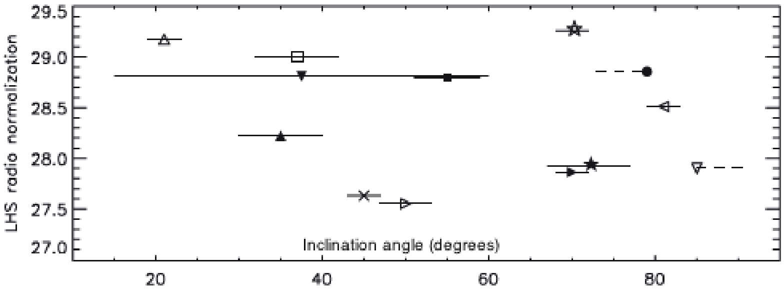

Figure 2.5: No correlation between inclination of the BHXBs to line of sight of the observer and normalisation for both radio and infrared regime; Image reproduced from Soleri & Fender (2011).

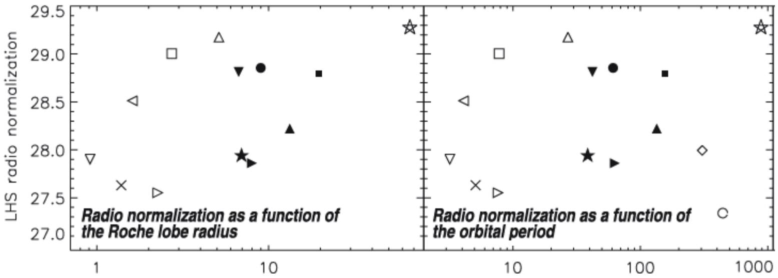

Figure 2.6: Correlation diagram for accretion disc size and orbital period. The right panel shows no correlation between accretion disc size and radio normalisation. The left panel shows no correlation between orbital period and normalisation; Image reproduced from Soleri & Fender (2011).

2.3 Mass measurements

Accurate measurements of BH masses are critical to verify whether the position of a source on the radio/X correlation diagram depends on their BH mass. The mass measurement of a BH is not trivial and has large uncertainties associated with it. From the literature, I have compiled mass estimates of a sample of BHXBs, which were obtained from two main measurement techniques:

(i) the **Dynamical Method**; The method is based on Kepler's third law of motion. Since BHXBs are similar to single-lined spectroscopic binaries, only the radial velocity curve of the companion star (extracted from a timing series of spectra) is available. From the radial velocity curve, the orbital period (P_{orb}) and the radial velocity semi-amplitude (K_c) may be extracted and used in the *mass function*, which is defined by Equation 2.5. This is used to obtain the mass of the BH, M_X. The mass function is given by,

$$f(M) = \frac{K_c^3 P_{orb}}{2\pi G} = \frac{M_X^3 \sin^3 i}{(M_X + M_c)^2} = \frac{M_X^3 \sin^3 i}{(1+q)^2} \, . \qquad (2.5)$$

In Equation 2.5, M_c is the mass of the companion star, q is the mass ratio $q = M_c/M_X$ and G is the Newtonian gravitational constant. This expression assumes a circular orbit at an inclination i. If the inclination of the system is not constrained, the mass function provides a solid lower limit to the mass of the black hole even for a mass of the companion $M_c = 0$ and an edge-on geometry (Casares & Jonker 2014).

(ii) the **Spectral-timing correlation scaling technique**; The inherent features of the X-ray spectrum and the rapid variability of X-ray luminosity can be correlated to determine the mass of the black hole and its distance from us (Shaposhnikov et al. 2010). This technique of analysis requires (1) a reference source, whose BH mass and distance is known, and (2) a large scalable number of observations which records how the target and the reference source evolves in its spectra over time as they make spectral transitions. There exists a spectral index associated to each frequency at which quasi periodic oscillations (QPO) occur. By plotting an empirical function to the X-ray variablity data, one can infer both a gradient (index) and a normalisation of the power law function used to fit the data. The index and normalisations are correlated to find any coherence arising from the QPO and these are known as *index-normalisation correlation patterns.* The *spectral index-QPO frequency* is the frequency of the quasi periodic oscillation at which the spectral index is being taken or considered. The spectral index–QPO frequency and index–normalisation correlation patterns are used to calculate the scaling factors with respect to the reference source. The BH mass can then be extracted since the QPO frequency is assumed to depend on the BH mass ratio only. But this is a highly debated assumption since we still do not understand the exact origin of QPOs.

2.4 Results and analysis

In this section, I present my results on whether the BH mass in a BHXB has an influence on the track it follows on the radio/X-ray correlation diagram. This was done by comparing the radio normalisation of a sample of sources with their corresponding estimated BH mass. Futhermore, I review the dependence of binary parameters (orbital period and inclination) as in Soleri & Fender (2011), for our sample of BHXBs which includes additional and recently monitored sources.

The quasi-simultaneous radio and X-ray observations of the sources used in Corbel et al. (2013) were revisited and updated. The X-ray luminosity is in the 1-10 keV band. Sources having only an upper limit recorded ($\leq 10^{33}\,\mathrm{erg\,s^{-1}}$ in luminosity) are excluded. Table 2.1 shows 17 BHXBs, for which I determined the most up to date radio/X-ray normalisation values (defined as $\log\kappa$ in Equation 2.2). This was done by minimising our fitting function ($L_{radio} = \kappa\, L_X^{0.6}$; a power law of fixed spectral index, $b = 0.6$) which will best fit the evolution of both fluxes in log scale for all the observations of each source. The values $\log\kappa$ in Table 2.1 are evaluated for values of L_X normalised to $10^{34}\,\mathrm{erg\,s^{-1}}$, i.e. $L_{radio} = \kappa\left(\frac{L_X}{10^{34}}\right)^{0.6}$. The uncertainty on the normalisation for N observations of a given source has been estimated by minimizing the square root of the Chi-square value. The Chi-square value is defined as in Equation 2.6 below:

$$\chi^2 = \sum_{i=1}^{N-1} D_i^2 = \sum_{i=1}^{N-1} \frac{(y_i - f(x_i))^2}{\sigma_{yi}^2 + \sigma_{xi}^2 f'^2(x_i)} \tag{2.6}$$

The values of y_i, x_i, σ_{yi} and σ_{xi} correspond to the radio luminosity, X-ray luminosity, and their corresponding errors respectively for the i^{th} observation of one source. Both minimization of the fitting function and the error-function (Equation 2.6) were carried out using the “optimize” package in python. All the sources whose data have been used are referenced in Table 2.1.

Figure 2.12, 2.13 and 2.14 (on pages 40-42) show the data and fitting functions from which we have estimated radio normalisation for our whole sample of sources. Using these values of radio normalisation, we can probe which parameters influence the BHXB to follow a particular track. We follow the

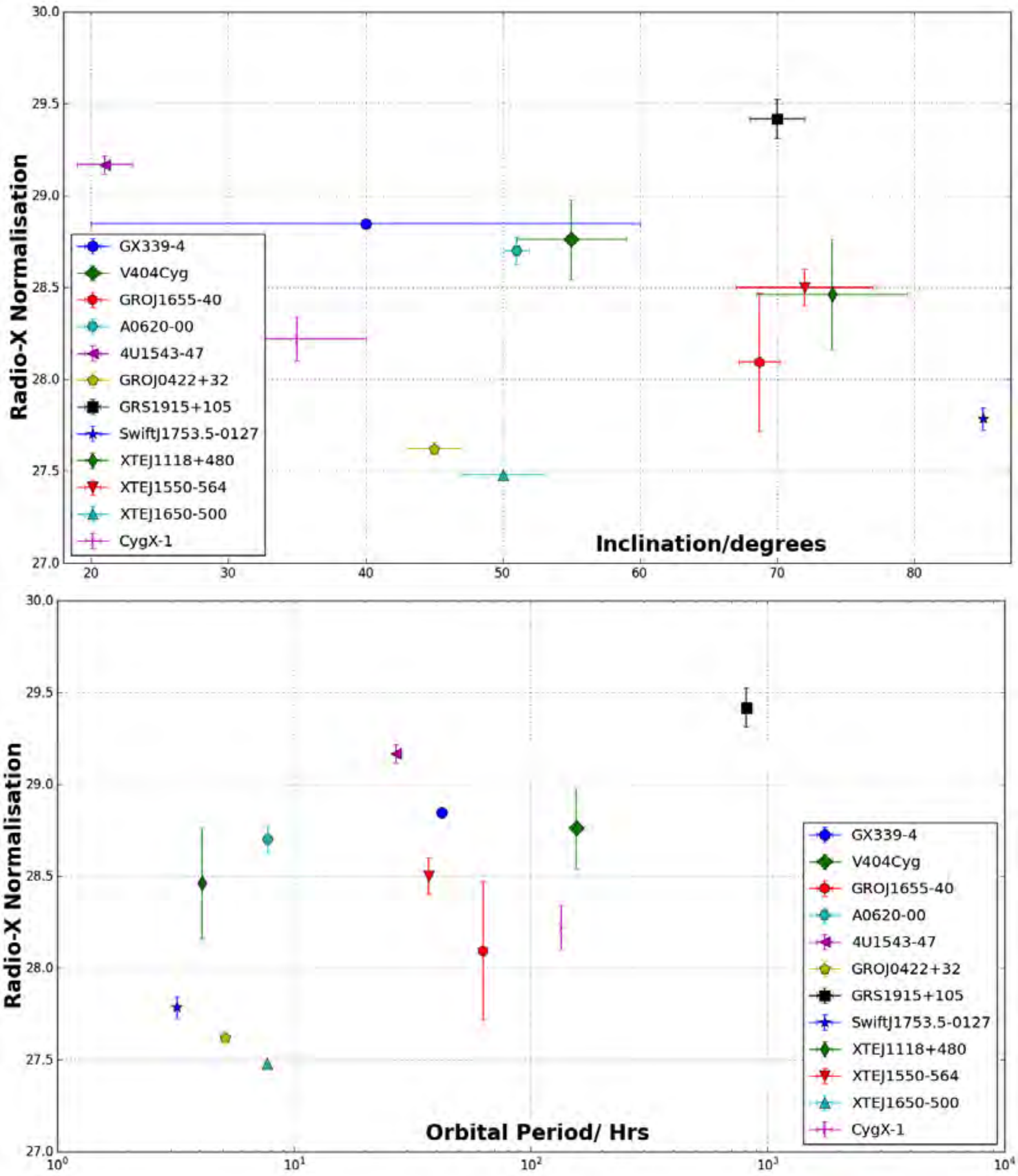

Figure 2.7: The datasets of radio/X-ray normalisation values against both inclination and orbtial period respectively. The top panel shows that there is no correlation between normalisation and inclination where the Spearman correlation coefficient was calculated for the data set and found to be $\Omega \sim -0.20 \pm 0.55$. The bottom panel shows no correlation between normalisation and orbital period and where the Spearman correlation coefficient was calculated to be as $\Omega \sim -0.27 \pm 0.40$.

similar methodology as in Soleri & Fender (2011) and Fender et al. (2010). Figure 2.7 shows that there is no clear correlation between these radio/X-ray normalisation values with the binary inclination and orbital period (from literature; see Table 2.1). The Spearman correlation coefficient was calculated for the inclination against radio/X-ray normalisation data set (top panel of Figure 2.7) and found to be -0.20 ± 0.55. Similarly the Spearman correlation coefficient was calculated to be -0.27 ± 0.40 for the orbital period against radio/X-ray normalisation data set (bottom panel of Figure 2.7). Our results are consistent with the work of Soleri & Fender (2011) since the values of the coefficient are close to zero, implying no correlation between the studied parameters.

In order to investigate the relation between BH mass and radio normalisation, I have compiled the most up-to-date mass estimates from the literature for the 17 BHXBs. The values and corresponding references are listed in Table 2.1. Figure 2.8 shows **all** our sources for which we have a radio/X-ray normalisation $\log(\kappa)$ and mass of the compact object.

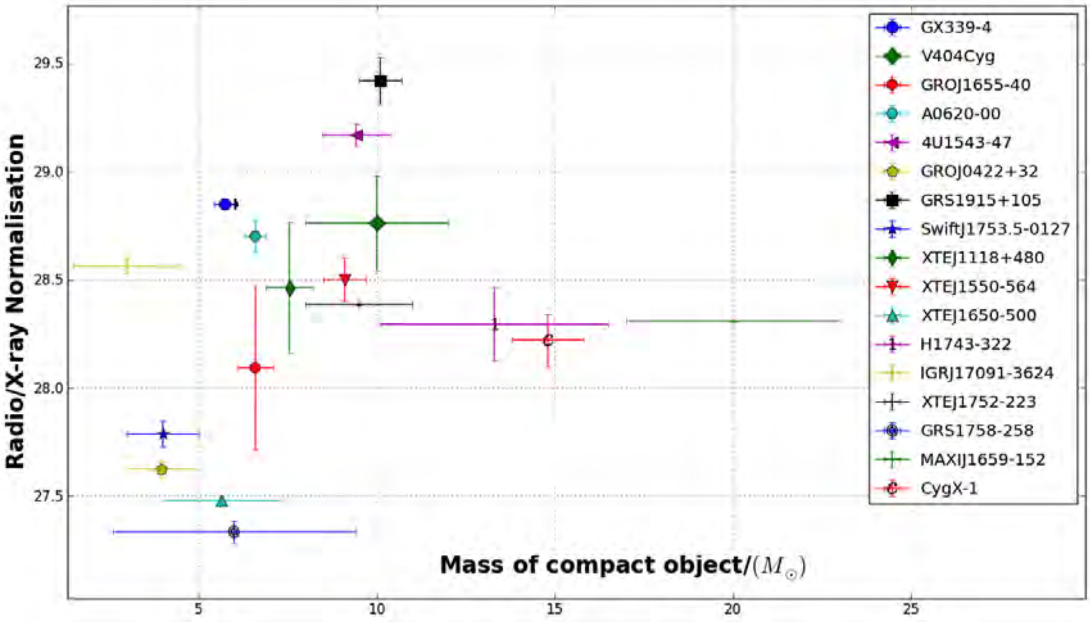

Figure 2.8: The scatter plot of **all** our sources for which we have a radio/X-ray normalisation and mass of the compact object as in Table 2.1 without selection criteria. The Spearman correlation coeficient is $\Omega \sim 0.28 \pm 0.25$

The Spearman correlation coeficient for the Figure 2.8 is $\Omega \sim 0.28 \pm 0.25$ (without selection criteria). However when our sample is restricted using well defined selection criteria, the correlation becomes clearer. The selection criteria which have been adopted are as follows:

1. **No sources having just quiescent measurements**
   I excluded sources for which only quiescent measurements are available; because they don't show an evolution of their luminosity on a radio/X-ray correlation diagram, and therefore they cannot be evaluated on which track they lie.

2. **Low-mass X-ray binaries only**
   I have excluded Cyg X-1 as it is a HMXB with a very peculiar behaviour partly due to the fact that it transfers mass through winds. Since Cyg X-1 is also the only HMXB of our sample and it might be biased to include it (see Figure 2.8).

3. **Dynamically estimated masses**

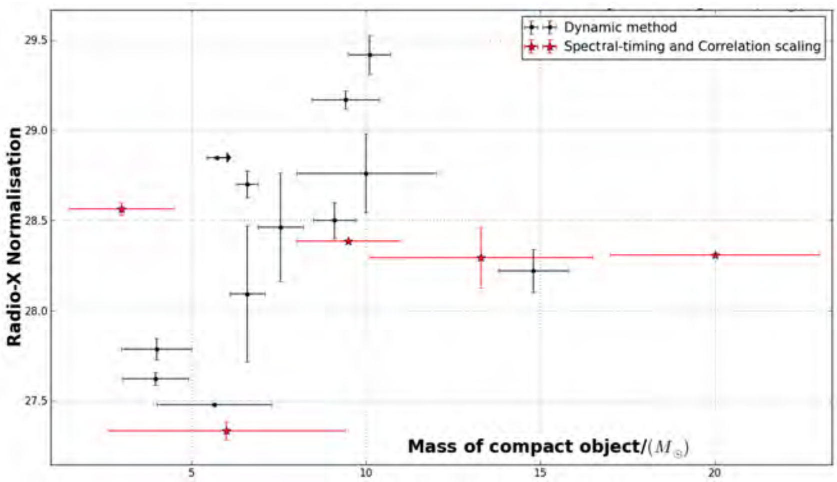

Figure 2.9: The scatter plot of **all** our sources where the measurement technique of the BH mass is specified. These are by (i) dyanmical method (indicated with black pointers) and (ii) Spectral-timing correlation scaling method (indicated with red pointers).

I additionally excluded sources for which the mass measurement has been obtained through the spectral-timing correlation technique (see Section

2.3). The latter relies on assumptions about a direct link between the BH mass and the spectral and timing properties which are not demonstrated yet. The dynamic method which simply relies on direct observation of lightcurves, is a more reliable and accurate method to obtain the BH masses. Figure 2.9 shows the sources whose mass were estimated dynamically, and the sources whose mass were estimated through spectral-timing correlation.

The point is that if we include the sources with non-dynamical mass estimates, the HMXBs, and sources with quiescent measurement only (see Figure 2.8), the correlation between the normalisation and the mass is much weaker or non-existent. Figure 2.10 shows our correlation diagram for the radio/X-ray normalisation $\log(\kappa)$ against the mass of BH but chosen within the set of full selection criteria mentioned above. The Spearman correlation coefficient was found to be $\Omega \sim 0.78 \pm 0.01$ which means that the set of selection criteria has improved this correlation.

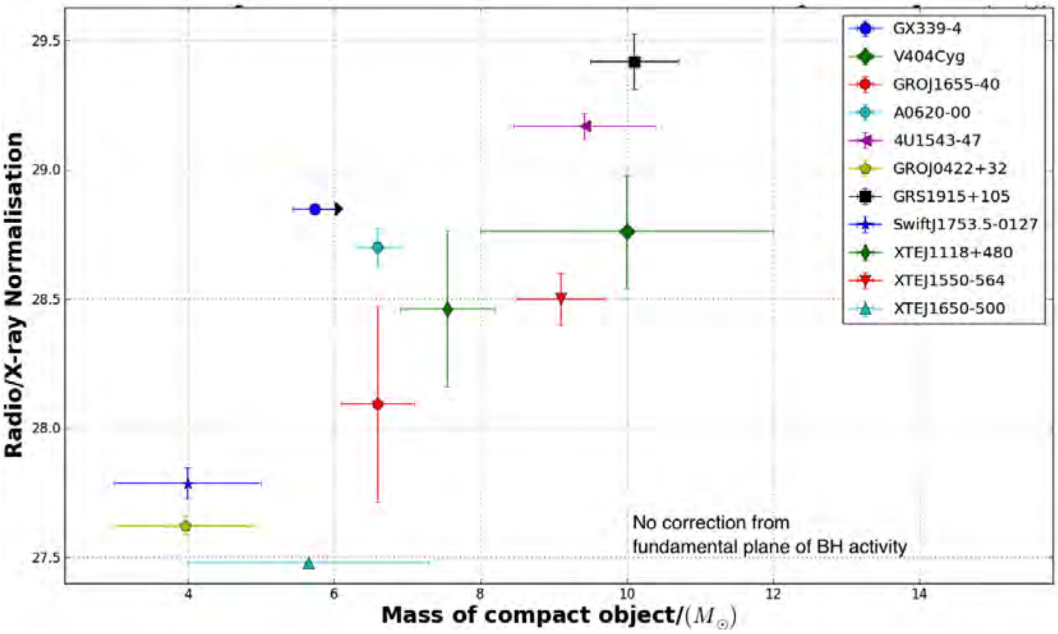

Figure 2.10: The correlation diagram for the radio/X-ray normalisation against the mass of the accretor for sources listed in Table 2.1 chosen within selection criteria. The Spearman rank correlation coefficient is calculated as $\Omega \sim 0.78 \pm 0.01$.

It should be noted that the already known dependence of the radio and X-ray luminosities on the BH mass (i.e. the fundamental plane of BH activity; see Figure 2.2, Section 2.1) could slightly bias our study. Therefore, we remove this bias by subtracting this mass dependence that originates from the fundamental plane. The **Corrected normalisation** η is simply defined as:

$$\eta = log(\kappa) + Klog(M/M_{\odot}) \ , \tag{2.7}$$

where $K = \frac{\xi_M}{\xi_R}$ is the ratio of the fundamental plane coefficients as in Plotkin et al. (2012). Having subtracted the mass dependence from the fundamental plane, we can now test for the existence of a correlation between the BH mass and the radio/X-ray normalisation. Figure 2.11 shows our correlation diagram for the corrected normalisation η against the mass of BH for our sample of 17 sources as in Table 2.1 (within the same selection criteria).

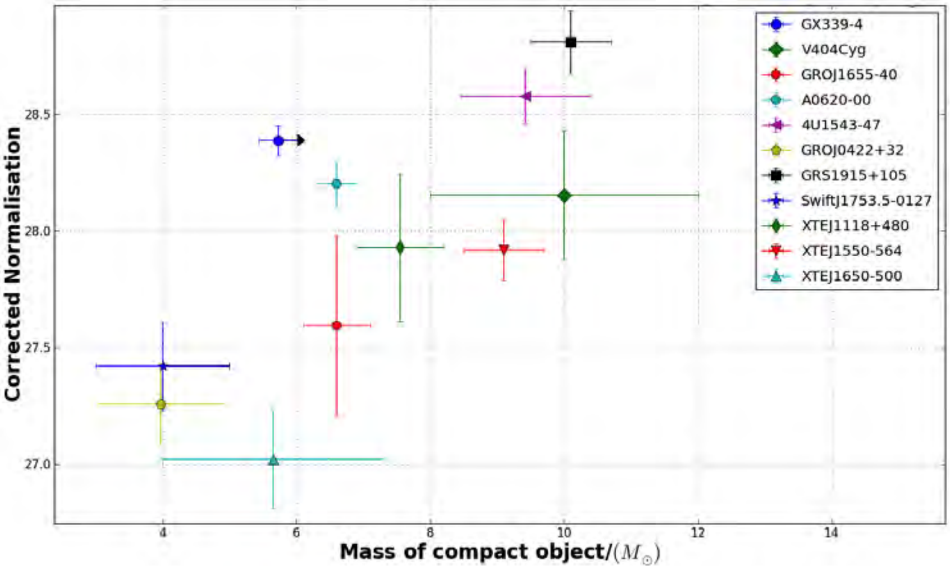

Figure 2.11: The correlation diagram for the corrected normalisation η against the mass of the accretor for sources listed in Table 2.1 chosen within selection criteria. These radio/X-ray normalisations are corrected from any mass dependence from fundamental plane of BH activity (see Equation 2.7). The Spearman rank correlation coefficient for the corrected version is found to be $\Omega \sim 0.73 \pm 0.01$.

The Spearman correlation coefficient was calculated which gives $\Omega \sim 0.73 \pm 0.01$. Although by comparing the corrected values and the actual values of radio/X-ray normalisation in Table 2.1, one can notice that those corrections, as indicated in Equation 2.7, are actually small. The correlation still exists when the correction from the fundamental plane of BH activity is considered and this gives us confidence. It should be noted that the correction from the fundamental plane relation have been taken into account into the error of the corrected normalisation. The errors of corrected normalisation dataset are larger than the previous normalisation dataset (without correction), which certainly weakens the correlation coefficient. This suggests that the tested parameters have a significant degree of correlation since the value of the coefficient is close to 1.0 (ideal case). This results should be further confirmed once additional and more accurate mass measurements will be available.

2.5 Discussion

In this Section, I discuss the methodology used, the results and interpretation. I also mention all the various considerations that ought to be taken before adopting any stance on this result.

2.5.1 Methodology

Following Soleri & Fender (2011) and Fender et al. (2010), I have adopted the same methodology of using the radio/X-ray normalisation to investigate the influence of the mass of the BH (analogous to spin, orbital period, and other binary parameters). As mentioned in Section 2.2, the radio/X-ray normalisation (parameter "κ" in Equation 2.1) serves as an indicator of whether a source lies on either the upper or the lower track. Therefore, I investigate whether the masses of BHs correlate with the radio/X-ray normalisation values or not. If this correlation can exist, then it means that the mass of the BH influences the position of a source on the radio/X-ray correlation diagram; since sources following the upper (lower) track usually have a high (low) normalisation.

This methodology seems valid as long as we have (i) accurate masses of BHs, and (ii) reliable radio/X-ray normalisation values. The large error bars in Figure 2.10 for some objects (e.g V404 Cyg and GRO J1655-40) could be reduced so as to strengthen the correlation. For example, the mass function (Equation

2.5) depends on several parameters which are not accurately constrained and the propagation of these uncertainities can account for larger errors in dynamically estimated masses of BHs. Additionally, the estimated radio/X-ray normalisations could be debated for its accuracy due lack of errors in observational data especially where only one observation was recorded for one source e.g. A0620-00 and IGRJ17091-3624, IGRJ17177-3656 and XTEJ1720-318. An error corresponding to 10% of observed fluxes was assigned to these 4 sources which corresponds to the typical (conservative) accuracy obtained with the RXTE satellite. Moreover, single observations do not show and cannot predict the evolution of the source on a radio/X-ray correlation. It can be biased to associate the sources which are at low luminosity to lie on either the upper or the lower track. The reason is that we have also observed cases where a source has changed from one track to another e.g. H1743-322 (see the plot on top panel in the second column in Figure 2.12). Those facts should be taken into consideration before taking any stance regarding this correlation and any inference about it.

2.5.2 Inference of results

I have found a good correlation for the mass of BH with the radio/X-ray normalisation (see Figure 2.10), where the Spearman rank correlation coefficient is found to be $\Omega \sim 0.78 \pm 0.01$ ($\Omega \to 0.0$ means no correlation and $\Omega \to \pm 1.0$ implies an ideal correlation). When I reviewed the correlation of radio/X-ray normalisation with inclination and orbital period, I find the values $\Omega \simeq -0.20 \pm 0.55$ and $\simeq -0.27 \pm 0.40$ respectively. The results are consistent with the work of Soleri & Fender (2011) since the values of the coefficient are close to zero. The Spearman correlation coefficient is considered as a reliable tool to verify the strength of a correlation. Therefore, this suggests that the mass of BH has a significant influence on which track (standard or outliers) the source belongs to on a radio/X-ray correlation diagram.

Our sample consists of only 17 sources and may not be fully representative for the general behaviour of all BHXBs that exist. However, I deduce the following. From the correlation diagram in Figure 2.10, one can infer that sources with more (less) massive BH tend to have higher (lower) radio/X-ray normalisation $\log(\kappa)$. This may imply that BHXBs with a massive BH will tend to populate the standard track whereas BHXBs with a less massive BH will tend to populate the outliers' track.

Soleri & Fender (2011) mentioned that "many BHXBs have been found to produce fainter jets at a given accretion-powered luminosities than expected from the earlier correlation", and suggested that BHXBs with similar accretion flows can produce a wide range of jet power due to some parameter or factor. We find that, at a given X-ray luminosity (proxy for accretion-power), BHXBs with a more massive BH (on the standard track) are observed with higher emission of radio luminosities. Similarly, BHXBs with less massive BH (on the outliers' track) are observed with lower emission of radio luminosities. This may imply that BHXBs with more (less) massive BH will have more (less) powerful jets.

The radiative efficiency of an accretion flow is given by $\epsilon = \dfrac{L}{\dot{M}c^2}$, where L is the total luminosity and $\dot{M}$ is the accretion rate (Shakura & Sunyaev 1973). Coriat et al. (2011b) proposed that those hard state BHXBs which are radiating efficiently occupies the outliers' track whereas the BHXBs on the standard track are actually radiating inefficiently. An alternative possibility to the less/more powerful jets (as mentioned above) is that hot inner accretion flow seems to be radiatively more (less) efficient if the BHXB has a less (more) massive accreting BH. This should be valid, at least, within a given range of luminosity (typically above $10^{-3} L_{edd}$), since at low luminosity, sources have been observed to change track (e.g. H1743-322). At the same time, although there exists transitions between the two correlation tracks, further investigations are needed to understand why such a small difference of mass could lead to such noticeable differences in correlation index on the radio/X-ray correlation diagram.

In addition, Xie & Yuan (2012) states that the radiative efficiency of accretion flow increases with increasing accretion rate, which gets intensified by viscous interactions. However, since the viscosity parameter of the disc is not related to mass of BH, it could suggest that viscosity plays no critical role in explaining the dual radio/X-ray correlations, if the mass dependence reported here holds.

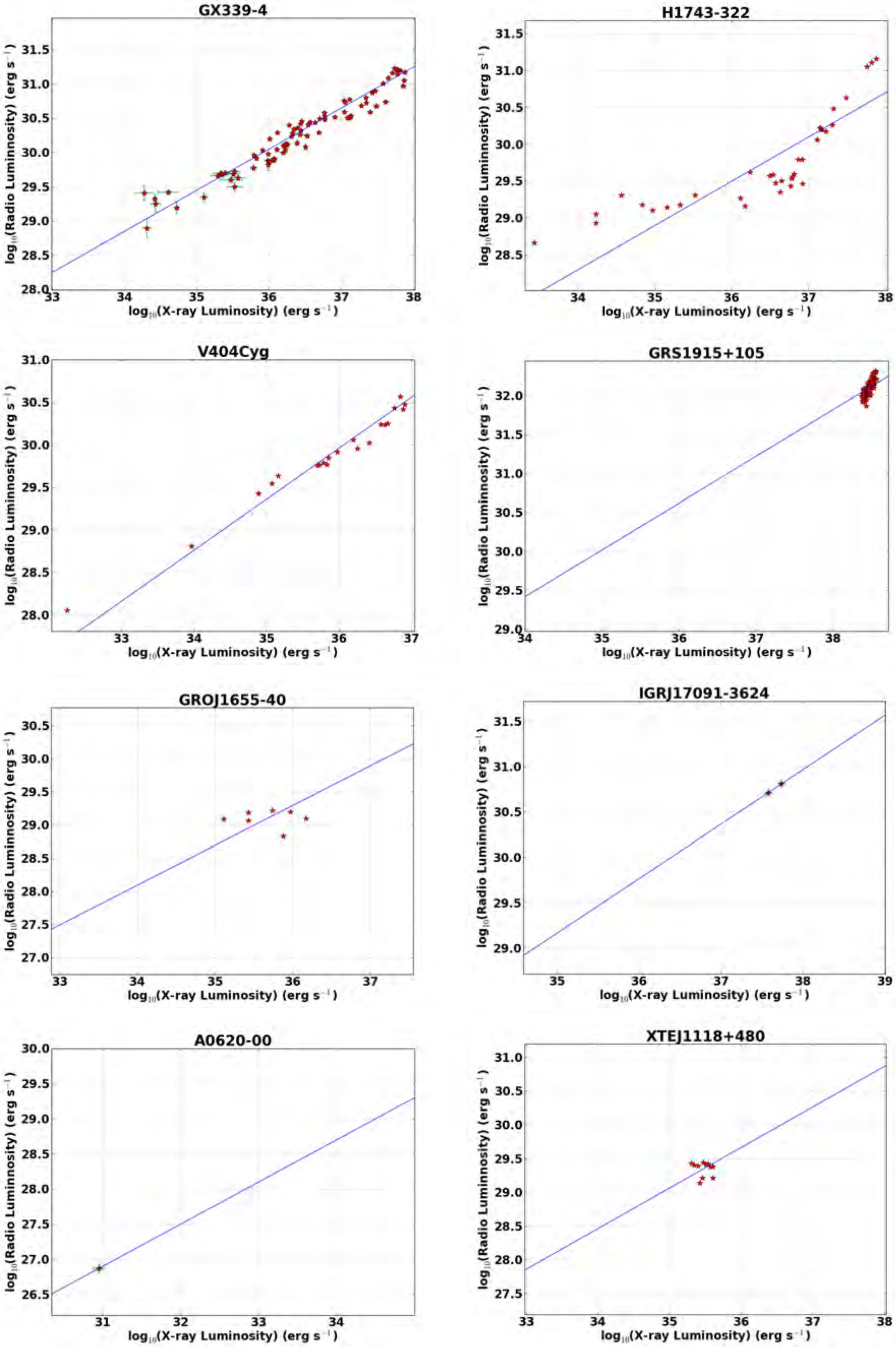

Figure 2.12: The radio/X-ray normalisations of our sample of 18 sources-Part I; This figure show only the first 8 sources namely GX 339-4, H 1743-322, V404 Cyg, GRS 1915+105, GRO J1655-40, IGR J17091-3624 and A0620-00 and XTE J1118+480. The X-ray luminosity is in the 1-10 keV band.

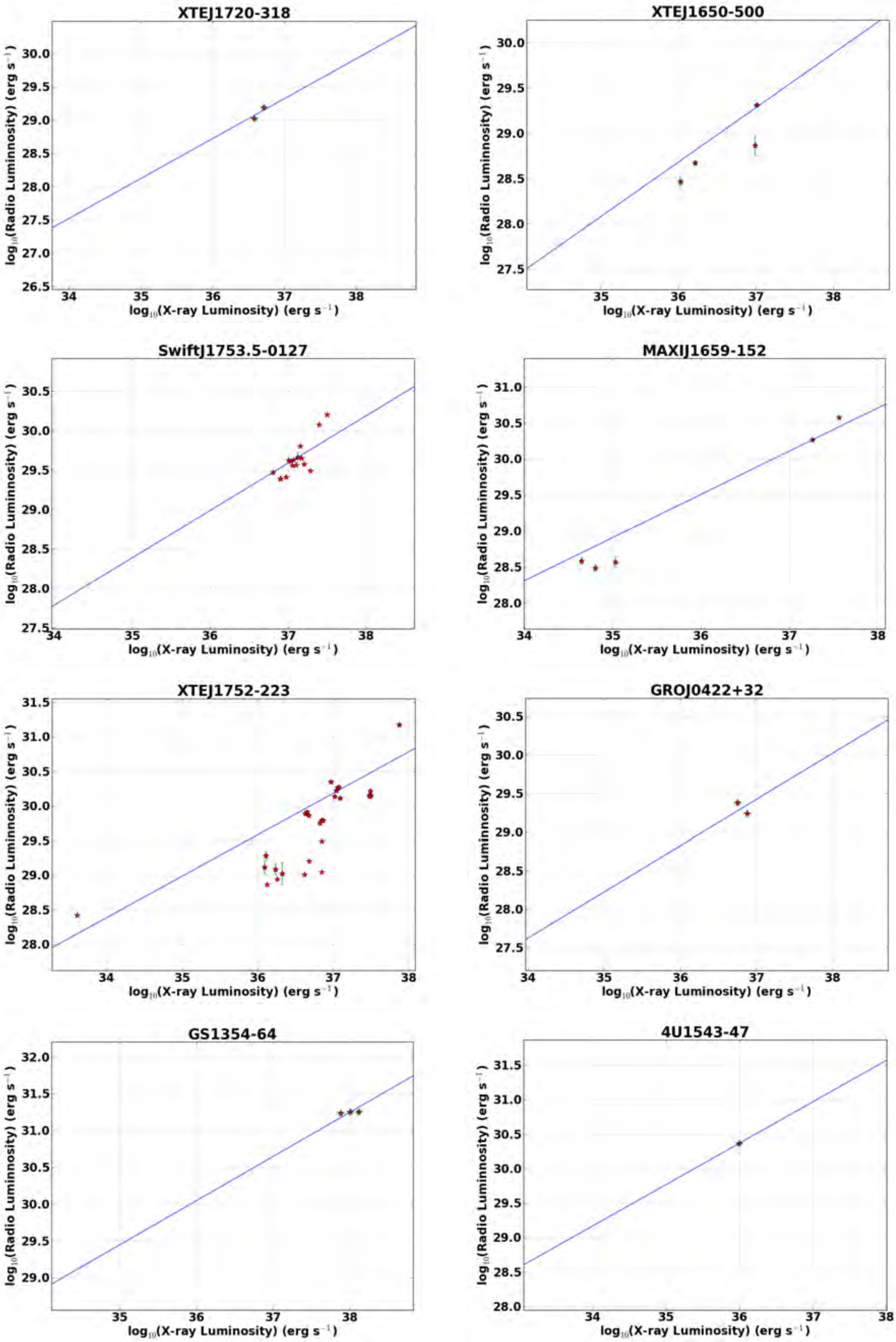

Figure 2.13: The radio/X-ray normalisations of our sample of 18 sources-Part II; This Figure show only the second 8 sources of the sample namely XTE J1720-318, XTE J1650-500, Swift J1753.5-0127, MAXI J1659-152, XTE J1752-223, GRO J0422+32, GS 1354-64 and 4U 1543-47. The X-ray luminosity is in the 1-10 keV band.

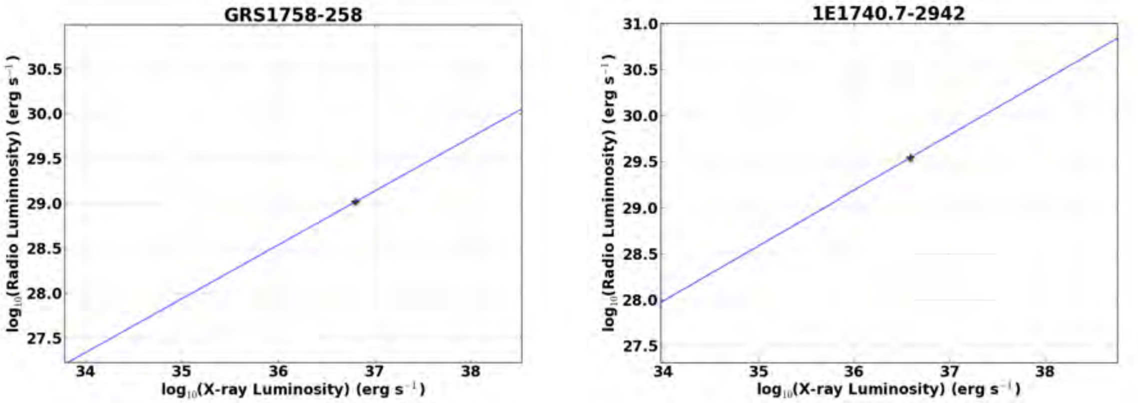

Figure 2.14: The radio/X-ray normalisations of our sample of 18 sources-Part III; This Figure show only the last 2 sources of the sample namely GRS 1758-258 and 1E 1740.7-2942. The X-ray luminosity is in the 1-10 keV band.

Table 2.1: The sample of sources with the most up to date masses; The sources are identified by their names. η and $\log \kappa$, represent the corrected and uncorrected Radio/X-ray Normalisation. Err_{η} and $Err_{\log \kappa}$ are the associated error in corrected and uncorrected normalisation. $Mx \pm dMx$ denotes the mass of the source X. $i \pm di$ denotes inclination and $D \pm dD$ represent the distance to observer. The references for mass estimates as well as radio luminosity and X-ray luminosity are under RefA and RefB columns respectively.

Sources	η	Err_{η}	**P$_{orb}$/hrs**	M_x	$dM_x/\pm$	**i**	**di**	**D/kpc**	**dD**	**RefA**	$\log \kappa$	$Err_{\log \kappa}$	**RefB**
GX339-4	28.39	0.07	42.14	>5.73	0.29	40	20	8	0	[1]	28.848	0.002	(a)(b)
V404Cyg	28.15	0.274	155.31	10.00	2.0	55	4	2.39	0.14	[2][3]	28.76	0.22	(d)
GROJ1655-40	27.59	0.39	62.92	6.60	0.5	68.7	1.5	<1.7	-	[4]	28.09	0.38	(f)(g)
IGRJ17091-3624	28.27	0.33	-	3.00	1.5	-	-	20.0	-	[5][6]	28.56	0.04	(h)
A0620-00	28.20	0.10	7.75	6.60	0.3	51	0.9	1.2	0.4	[7]	28.70	0.07	(i)
4U1543-47	28.58	0.12	26.95	9.42	0.97	21	2	7.5	0.5	[8][20]	29.17	0.05	(j)
GROJ0422+32	27.26	0.18	5.09	3.97	0.95	45	2	2.49	0.3	[9]	27.62	0.04	(j)
H1743-322	27.61	0.26	-	13.30	3.2	70	-	9.1	1.5	[10]	28.29	0.17	(c)
GRS1915+105	28.81	0.13	812.40	10.10	0.6	70	2	11.2	0.8	[11]	29.42	0.11	(e)
SwiftJ1753.5-0127	27.42	0.19	3.20	4.0	1.0	85	0	8	-	[18]	27.77	0.06	(k)(l)(m)
XTEJ1118+480	27.93	0.32	4.08	7.55	0.65	74	5.5	1.71	0.05	[12]	28.46	0.30	(j)(n)
XTEJ1550-564	27.92	0.13	36.96	9.10	0.6	72	5	4.1	0.8	[13]	28.50	0.10	(j)
XTEJ1650-500	27.02	0.21	7.69	5.65	1.65	50	3	2.6	0.7	[19][20]	27.479	0.008	(o)
XTEJ1752-223	27.79	0.14	-	9.50	1.5	-	-	8.0	-	[14]	28.385	0.003	(p)(q)
GRS1758-258	26.86	0.38	442.80	6.00	+3.4-1.45	-	-	8.5	-	[15]	27.33	0.05	(r)
MAXIJ1659-152	27.52	0.15	-	20.00	3	-	-	8.0	0.0	[16]	28.309	0.004	(s)
CygX-1	27.51	0.15	134.40	14.80	1	35	5	2.1	0.4	[17]	28.22	0.12	(b)

RefA: (1): Muñoz-Darias et al. (2008), (2): Casares (1996), (3):Wagner et al. (1992), (4): Shahbaz (2003), (5): Altamirano et al. (2011), (6): Rebusco et al. (2012), (7): Cantrell et al. (2010), (8): Orosz (2003), (9): Gelino & Harrison (2003), (10): Shaposhnikov & Titarchuk (2009) , (11): Steeghs et al. (2013), (12): Khargharia et al. (2013), (13): Orosz et al. (2011b), (14):Shaposhnikov et al. (2010), (15): Bezayiff (2006), (16): Shaposhnikov et al. (2011), (17): Orosz et al. (2011a), (18) Neustroev et al. (2014), (19): Orosz et al. (2004), (20): Özel et al. (2010).
The references of the radio and X-ray luminosities, **RefB**: (a)Corbel et al. (2003) (b)Corbel et al. (2013) (c)Coriat et al. (2011b) (d)Corbel et al. (2008) (e)Rushton et al. (2010) (f)Coriat et al. (2011a) (g)Calvelo et al. (2010) (h)Rodriguez et al. (2011) (i) Gallo et al. (2006) (j) Gallo et al. (2003) (k)Cadolle Bel et al. (2007) (l)Soleri et al. (2010) (m) Coriat et al. (2011b) (n) Fender et al. (2010) (o)Corbel et al. (2004) (p)Brocksopp et al. (2013) (q)Ratti et al. (2012) (Gallo et al. (2003)) (s) Jonker et al. (2012).

Chapter 3

SS433/W50

In this chapter, I focus on an interesting X-ray binary system, known as SS433, for which I wish to constrain the particle composition of its jets using circularly polarized radio emission (refer to Section 1.6.4). The description of this source in Sections 3.1 and 3.2 reveals its uniqueness and our motivation for choosing it as the target of our study.

3.1 General description of SS433

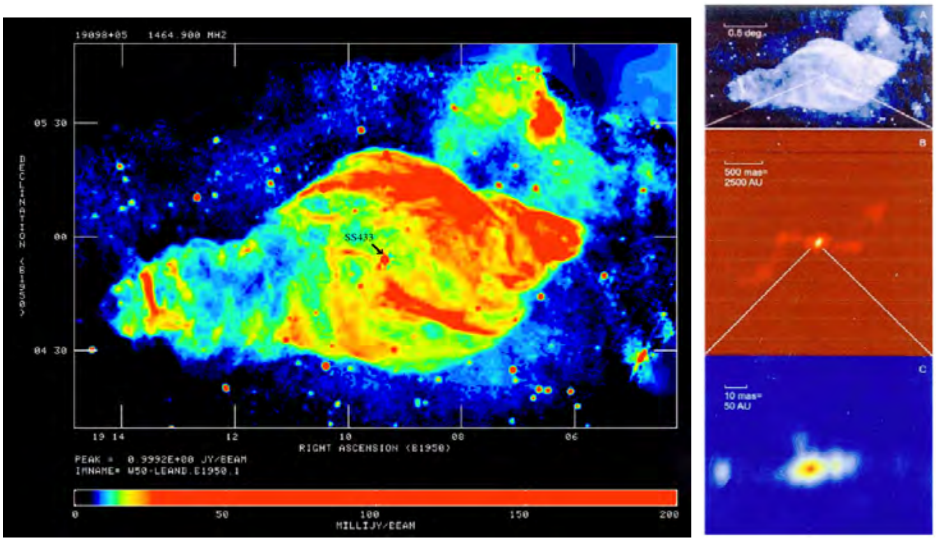

Figure 3.1: The exotic SS433 within its progenitor W50 supernova remnant; It is a HMXB with a supercritical accretion disc and precessing relativistic jets. The shape of of W50 nebula reveals the interaction of the jets of SS433 and its environment. On the right, the milli-arcsec scale of SS433 is shown relative to the degree-size of W50 nebula. Image adapted from Dubner et al. (1998).

SS433 (V1343 Aquilae) is an exotic X-ray binary system that is located at a right ascension (2000.0) of $19^h\,11^m\,49.56^s$ and declination (2000.0) of $+04^\circ\,58'\,57.6''$ at a distance of 5.5 ± 2 kpc. It is situated within a supernova remnant, namely W50 (see Figure 3.1). It consists of an accreting black hole ($M_{BH} = 4.8 \pm 0.8\,\mathrm{M}_\odot$) and an A7Ib supergiant companion star ($M_{comp} = 12.3 \pm 3.3\,\mathrm{M}_\odot$;Hillwig & Gies (2008)). The system has an orbital period of 13.082 days. Its relativistic jets ($v = 0.26c$) undergo precession (see Section 1.6.3) with a period of 162.5 days and nutation with a period of 6.29 days (Goranskii et al. 1998).

The intrinsic bolometric luminosity is estimated to be $\sim 10^{40}\,\mathrm{erg\,s^{-1}}$, with its maximum located in the non-observed UV region. The X-ray luminosity is about $\sim 10^{36}\,\mathrm{erg\,s^{-1}}$. One property which distinguishes SS433 from any other X-ray binary is its disc, which supports a non-transient regime of supercritical accretion ($L \geq L_{Edd}$) of gas at a high rate of mass transfer ($\sim 10^{-4}\mathrm{M}_\odot\,\mathrm{yr}^{-1}$; Shklovskii (1981)). As predicted by Shakura & Sunyaev (1973), a supercritical disc should be producing equatorial winds, which were later confirmed by observation and magnetohydrodynamic simulations (MHD; see Figure 3.2).

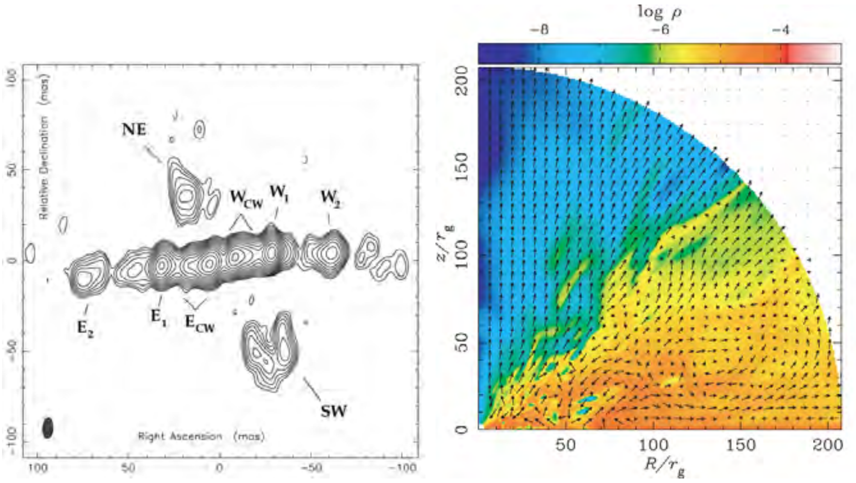

Figure 3.2: The winds of SS433; The supercritical accretion disc of SS433 is producing equatorial winds which are confirmed through: (i) the observations of these winds in North East and South West direction on the left image which is reproduced from Paragi et al. (1999); and (ii) MHD simulation as shown on the right image which is reproduced from Ohsuga et al. (2005).

3.2 Jets of SS433

The jets of SS433 are indeed remarkable. As mentioned earlier in Section 1.6.3 and 3.1, these relativistic jets ($v = 0.2699 \pm 0.0007\,c$) undergo precession and nutation. This provides us with a unique laboratory of high energy and extreme gravity physics. The key parts of this Section were derived from Marshall et al. (2013). Using the high resolution X-ray spectrum from Chandra's High Energy Transmission Grating Spectrometer (HETGS), several parameters of the jets of SS433 were estimated. The flux densities at these emission lines reveal a jet temperature of 5×10^6 to 1×10^8 K. The rate of the mass outflow is estimated as $1.5 \times 10^{-7} \mathrm{M}_\odot\,\mathrm{yr}^{-1}$. As the jet plasma moves out over a certain distance, the electron density drops, according to the adiabatic expansion model, from $\sim 2 \times 10^{15}$ to 4×10^{13} cm^{-3}. The total kinetic power of the jets was estimated as 3.2×10^{38} erg s^{-1}.

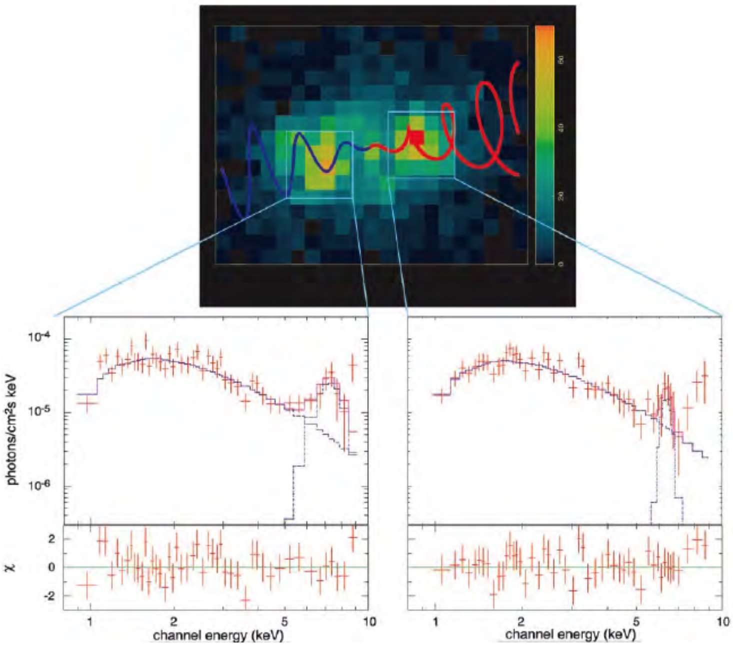

Figure 3.3: The spectra of jets for SS433; These X-ray spectra are spatially resolved and correspond to opposing jets that are moving in opposite direction. The Doppler-shifted emission lines at 6.4 and 7.3 keV in both jets spectra are an indication of iron lines (see text for more details). Image reproduced from Migliari et al. (2002).

Figure 3.3 shows the spatially resolved X-ray spectroscopy as obtained from the Chandra advanced CCD imaging spectrometer. The spectra of the two lobes were modelled using thermal bremsstrahlung with a temperature of ~ 5 keV. These spectra show the evidence of Fe K_β relativistically broadened and Doppler-shifted emission lines at 6.4 and 7.3 keV in jets of SS433. This implies that the plasma must be at temperature $\geq 10^7$ K for the presence of high excitation iron lines even at the observed scale of 10^{17} cm. But a plasma of $< 10^4$ K was observed, using optical emission lines, at 10^{15} cm from the core. According to adiabatic cooling models, this requires the reheating (acceleration) of the plasma at that distance. Additionally, the observed continuum cannot exclude the inverse Compton or synchrotron origin. Since these mechanisms require an electron population, the reheating would definitely occur at those distance. However, irrespective of which form of re-heating produces such a continuum, the emission lines do require a baryonic component (Migliari et al. 2002).

Using two high-resolution (spatial) instruments: VLBA (for radio wavelengths) and Chandra's HETGS (for X-ray wavelengths), Marshall et al. (2013) studied the same location within SS433 at two different wavelengths quasi-simultaneously. A high signal spectrum was generated using these observations and was used to test the emission model. After rectifying for varying blueshift, all the X-ray spectra (black lines in Figure 3.4) were processed together, including during the eclipse. A good fit was applied to the line flux densities data (red lines in Figure 3.4). The various lines which are recognized as features of the spectrum are labelled and re-verified by the model and by using ISIS and APED atomic database for lines of emissitivities. The X-ray emission and optical emission seem to originate at $< 2.7 \times 10^{14}$ cm and $< 3.1 \times 10^{14}$ cm respectively. It might be worth noting that changes in the redshifted and blueshifted jets are not simultaneous. This indicates that the jets are formed at independent direction and/or affected seperately by their own surrounding conditions.

As we can see in these spectra, SS433 displays lines of NI, Fe, Ca, Ar, S, Si, Mg, Al and O over a range of wavelength of 16.5 $\dot{A}$. The model of the spectrum suggest that Ni is five times overabundant as compared to other metals. There is an infered speculation that the supernova that created the SS433 was unusal for having created as much stable Ni as Fe.

Another interesting fact about the jets of SS433 is that they clearly inter-

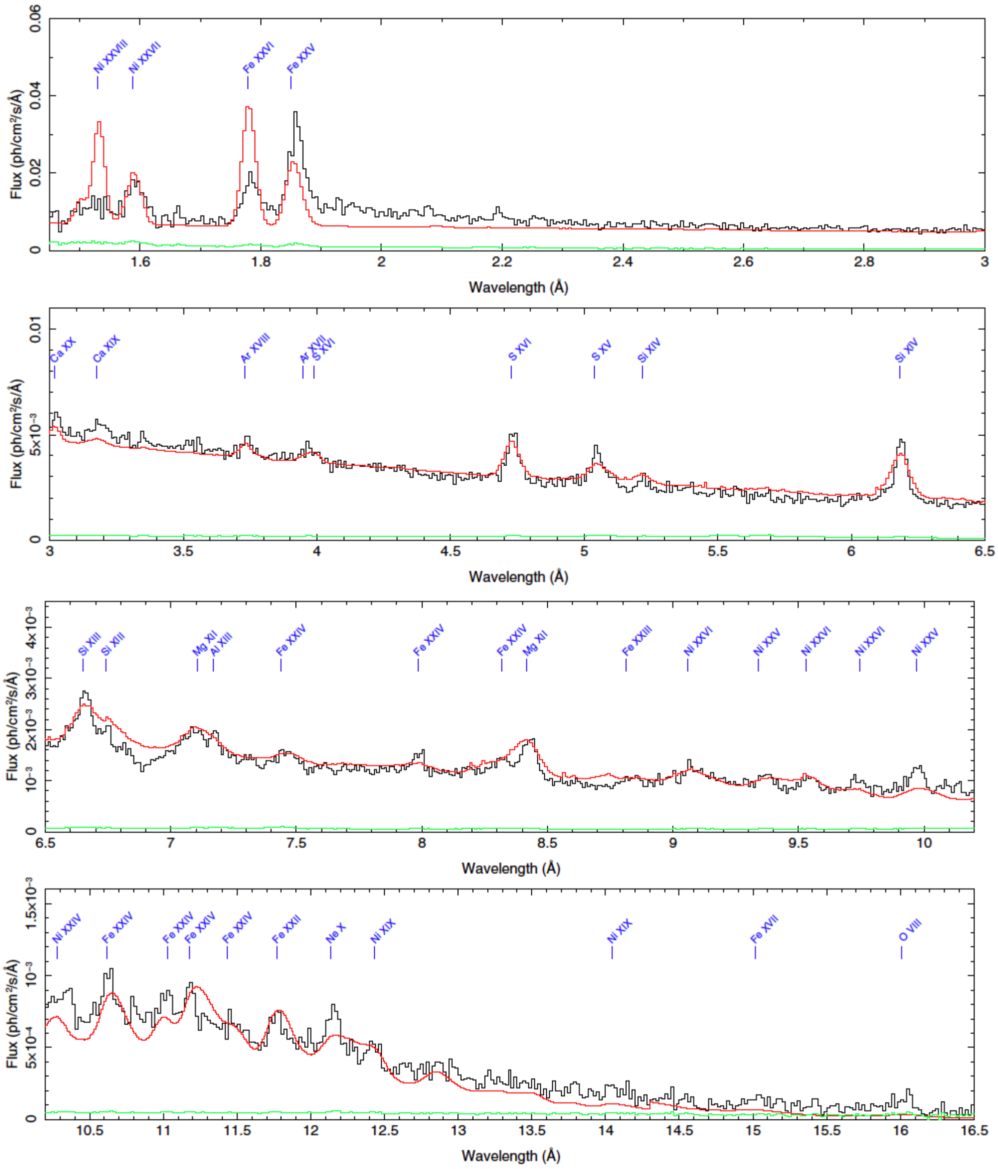

Figure 3.4: X-ray spectroscopy of SS433 using Chandra's HETGS; The black lines correspond to the X-ray spectra, the red line is the applied fit to the line flux densities data and the green line corresponds to the statistical uncertainities of the flux measurements. Image reproduced from Marshall et al. (2013).

act the surrounding supernova remnant W50. As shown in Figure 3.1, W50 has two pointing edges as its "ears" which are made because of the W50/jets interaction. Figure 3.5 shows simulation for W50/jet interaction using velocity map and hydrodynamics at high resolution. When cross-matching with contour map of SS433/W50 images (white dashed line), Goodall et al. (2011) could fine-tune the background density parameter (Particle number density: 0.2 cm^{-3} and radius z = 40 pc) so as to reproduce the East-West asymmetry in W50. Additionally, the analysis of high resolution observations of the radio filaments across W50 at each epoch, showed that these filaments were not in any significant motion. This implies either that (i) the ejecta of SS433's jets decelerates considerably in the W50 nebula, or (ii) the lobes of W50 were formed a much longer time ago in the history of SS433, during a jet outburst with different defining parameters as compared to what it is currently.

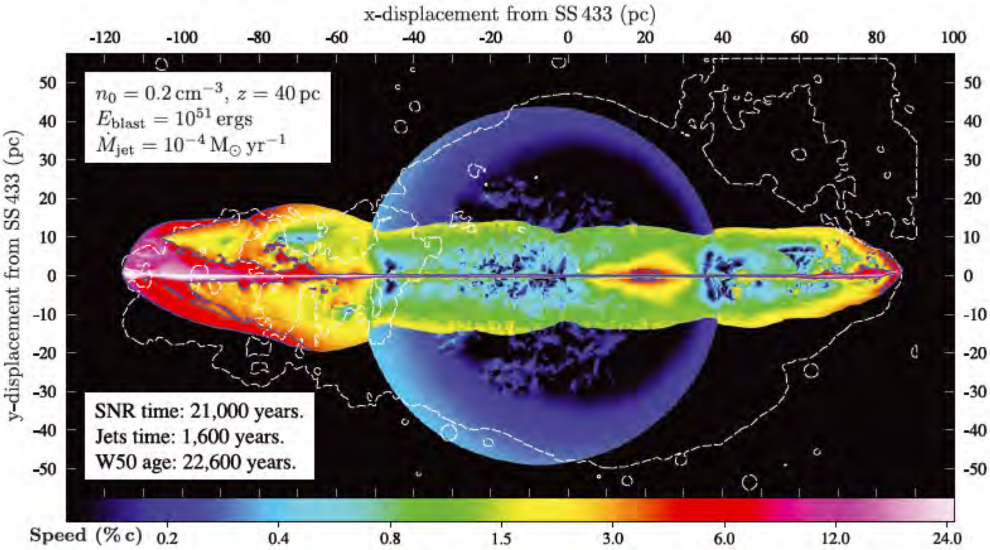

Figure 3.5: The hydrodynamic simulation of the W50/jets interaction; The hydrodynamic modeling of the expanding supernova remnant shell and the precession of relativistic jets was carried using mesh code FLASH. The simulation was tested for various parameters such number density of particles n_o, total energy of the supernova blast E_{blast}, rate of outflow in jets $\dot{M}_{jet}$, the age of the supernova, jet travel time, and age of W50. And the right set of parameters were able to reproduce the asymmetry in W50 through jet interaction. Image reproduced from Goodall et al. (2011).

3.3 Definition of the problem

Circularly polarized (CP) emission was discovered in SS433 (Fender et al. 2000) using the Australian Telescope Compact Array (ATCA) in the frequency range $1-9$ GHz. The flux density spectrum of CP emission is of the form $F_V \propto \nu^{-0.9\pm0.1}$, where the observations of the CP flux densities were made in terms of Stokes V parameters (F_V) during a flaring period, as shown in the light curve in Figure 3.6.

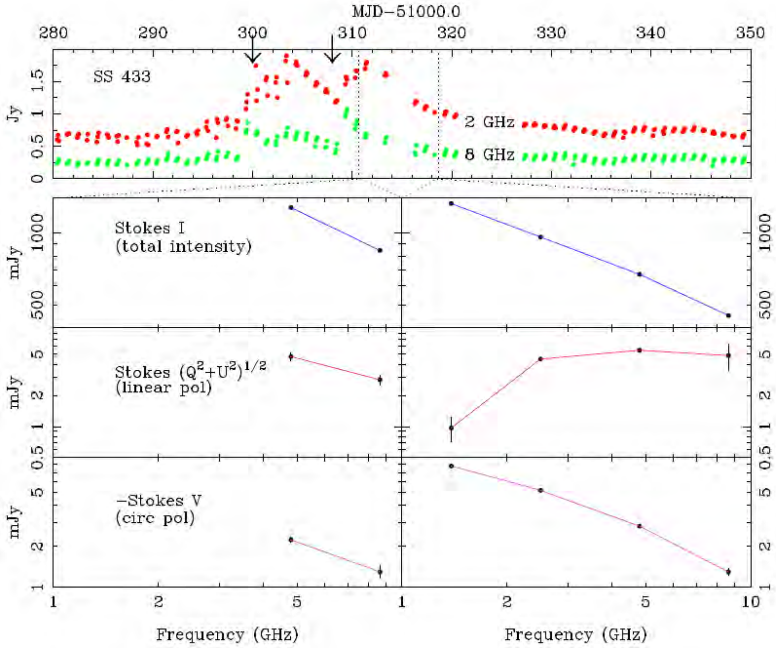

Figure 3.6: Discovery of circularly polarized emission in SS433. The light curves of SS433 as observed at two different frequency bands (2 GHz and 8 GHz) are shown at the top. The two arrows indicate the start of two consecutive flares at which the spectrum was observed. The spectra for total intensity (Stokes I), linear polarization (Stokes Q and U) and circular polarization (Stokes V) are shown for several frequency bands for the two consecutive flares (left and right panels). Image reproduced from Fender et al. (2000).

A key question using circular polarization is to determine if the composition of the jet plasma content is either leptonic or baryonic (see Section 1.6.4). Using a broad spectrum of circularly polarized flux densities, one can constrain the spectral index. The frequency dependence of the fractional circularly polarized emission, $m_c = V/I$, $m_c \propto \nu^{\alpha}$ can be used to constrain the different CP production mechanisms (which is detailed in Section 3.4). The predicted spectrum in the synchrotron case is $m_c \propto \nu^{1/2}$, whereas the spectral index may be $-3 \leq \alpha \leq -1$ for Faraday conversion models (Kennett & Melrose 1998). Therefore, depending on the dominant mechanism that seems to be at work, one can infer the energy content of the jets in the form of bulk Lorentz factor (see Equation 1.4-1.6 in Section 1.6.2). Depending on the energy content, we can attempt to constrain the particle composiiton, simply because a proton-electron pair is more massive than an electron-positron pair.

As mentioned earlier in Section 1.6.4, the composition of jets within a binary system can be achieved by different techniques. Several emission lines have been discovered recently using contemporaneous and spatially resolved spectroscopy (Marshall et al. 2013), which provides an indication of the baryonic content in SS433. Hence, by using the techniques of CP radio emission to confirm the baryonic content, one can validate the CP technique. In addition, O'Sullivan et al. (2013) mentions that CP in the radio emission from jets can be used as strong means to probe the jet magnetic field and particles for AGNs, since it remains unaffected by external screens as compared to linear polarized emission (although see Macquart & Melrose (2000)). Using circular polarization may therefore help us investigate the nature of magnetic field for the jet plasma of SS433 as well.

Another key problem is that the origin and location of circular polarized emission in SS433 is still unknown. Paragi et al. (2004) has collected intensive amount of circular polarization observations for the SS433 with VLBI, which confirms that there is no strong strong gyro-synchrotron (GS) emission whenever they investigated at sizes of order ($\leq$ 50 mas). Since the ATCA observations by Fender et al. (2000) rule out the extension with the optically thin jets on scales of $\geq 1''$, the CP emission is likely to be located within $0.1'' \leq r \leq 1''$, where r is the distance from the BH. This region hence can be probed by ATCA observations at millimeter frequencies.

3.4 Production mechanisms of circular polarized emission

In order to extract physical insights regarding the nature of jets from CP observations, we need to determine the dominant mechanism for CP production. The key parts of this sections were derived from Wardle & Homan (2001) and references therein. There are 4 different proposed mechanisms which could be the origin of CP emission in both AGN and X-ray binaries, as illustrated below:

1. **Faraday conversion**

   The Stokes parameter U is converted to V, and vice versa due to linear birefringent effect. Both rotation and conversion can be used to constrain the low energy end of the electron energy distribution. One important difference is that the Faraday rotation is proportional to the electron gyro frequency $\nu_{B_\perp} = \frac{eB_\perp}{2\pi mc}$, whereas the Faraday conversion is proportional to $\nu^2_{B\perp} \propto e^2 B^2_\perp$. Hence an equal mixture of electrons and positrons ($f_c = 0$) can produce Faraday conversion not rotation. The Faraday conversion acts on Stokes U, while synchrotron mechanism acts on Stokes Q only in the local frame of the B-field. Stokes U can be produced randomly by a tangled magnetic field or by internal Faraday rotation. The fractional CP, m_c produced by conversion, for a distribution of electron lorentz factors $n(\gamma) \propto \gamma^{1/2}$, is given by Equation 3.1 to 3.3:

$$m_c \approx \frac{1}{6}\tau_F \tau_C m_L^2 \tag{3.1}$$

$$\tau_F \approx 1.27\tau\Lambda \left(\frac{\gamma}{\gamma_{min}}\right)^2 \frac{\ln \gamma_{min}}{\gamma_{min}} \frac{B_u}{B_\perp} \sin\phi \tag{3.2}$$

$$\tau_C \approx -0.96\tau \ln \frac{\gamma}{\gamma_{min}} \tag{3.3}$$

   τ_F, τ_C, τ are the Faraday depth, conversion depth, and optical depths. m_L is fractional linear polarization. ϕ is the angle between the line of sight and the jets. $B_\perp$ is the r.m.s value of the magnetic field in the plane of the sky and B_u is the uniform component magnetic field which is parallel to the jets. Λ is a factor that accounts for the value of circular polarization to be reduced when the charges of the radiating particles are not all of the same sign. $\Lambda = D_a D_b$ such that $D_a = \frac{|\int B_u dl|}{\int |B_u| dl}$ and $D_b = \dfrac{(n^- - n^+)}{(n^- + n^+)}$. n^- and n^+ are the electron and positron densities respectively. γ_{min} is the low energy cutoff of the Lorentz factor distribution. These expressions apply for optically thin and Faraday thin medium. At significant Faraday and conversion depth, there can be nulls and sign reversals in the CP along the line of sight. The reader is directed to Jones (1988) and Jones & Odell (1977) for more details.

2. **Coherent radiation mechanisms**

   The synchrotron radiation emission occurs mainly by relativistic electrons spiralling in magnetic fields. The coherence of this synchrotron emission may arise either from particle bunching (see Figure 3.7) or from an anisotropic distribution function, leading to a negative absorption coefficient and maser action. Both cases appear to produce rather high fractional CP (though this may be diluted in a real source) and are intrinsically narrow band phenomena.

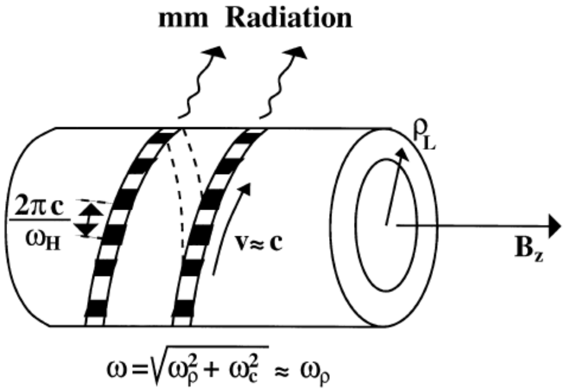

Figure 3.7: A bunching electron beam; As the relativistic electron beam spirals around a larmor radius ρ_L, the beam bunches. The emission due to these bunches are in millimetre wavelength. Image reproduced from Benford & Tzach (2000).

3. **Scintillation**

   Macquart & Melrose (2000) proposed that the total intensity (Stokes I) can generate circular polarized emission similar to scintillation by a birefringent screen in a magnetised turbulent environment. In this mechanism, Faraday rotation in the screen causes small displacement of the left and right hand side component of the total intensity. The scintillation produces amplitude patterns which are also diplaced from each other and an instantaneous fluctuating CP signal is detected. The r.m.s CP is given:

$$m_c \simeq \frac{\triangle\, x}{r_{scint}} m_I \tag{3.4}$$

where m_I is the fluctuation index in total intensity, and r_{scint} is the linear scale of the scintillation (diffractive or refractive) pattern and $\triangle\, x$ is the relative displacement of the right and left circularly polarized scintillation. The time scales for scintillation induced CP are a few minutes for diffractive scintillation, and several hours for refractive scintillation. But the sign of the induced CP should reverse on these timescales.

4. **Intrinsic circular polarization**
   Any synchrotron emission has a small intrinsic component of circular polarization (Legg & Westfold 1968). The maximum fractional circular polarization in a uniform B-field for electron emitting synchrotron at frequency ν is $|m_c| \approx 1/\gamma$ where γ is the Lorentz factor of electrons. For a more general situation with a combined uniform field, Equation 3.5 can be used:

$$m_c = -1.6\Lambda \left(\frac{\nu}{\nu_{B\perp}}\right)^{-1/2} \left(\frac{B_u}{B_\perp}\right) \sin\phi \tag{3.5}$$

Having mentioned the definition of problem for this Chapter and the various CP production mechanisms, I can now elaborate in the following sections on how we attempted to constrain the dominant mechanism for CP production and the energy content. Firstly, SS433 needs to be observed in terms of Stokes parameters (I, Q, U, and V) over a broad range of radio frequencies. After the observed data have been reduced, we can then estimate the value of flux densities at each frequency. From this, I construct a CP spectra from which the spectral index can be obtained. This spectral index would constrain the dominant mechanism and therefore constrain the energy content.

3.5 Data reduction

In this section, I present the circular polarization observations of SS433 and I detail of how the data were processed in order to obtain images and the estimates of flux densities. The objective behind data reduction is the removal of bad data (*flagging*) and the photometric calibration of observed sources.

3.5.1 Australian Telescope Compact Array (ATCA)

Figure 3.8: Australian Telescope Compact Array (ATCA) dish antenna, Credit: Ettore Carretti; This array of six 22-m dish antenna was used for our observation of SS433.

ATCA[*] (see Figure 3.8), located about 500 km North-West of Sydney, is an array of six 22-m dish antennas situated at the Paul Wild Observatory. The radio interferomery technique, used by ATCA, involves the combination of observed signals which are captured due to the motion of the antenna and the earth's rotation in order to sample the different spatial frequency components (u, v) of the Fourier space. The baselines extend from 31 m to 6 km according to the different configurations of the attenna. The interferometer operates in range of wavelength from 16 cm to 3 mm and can observe in two different bands simultaneously. Table 3.1 gives an overview of various operating modes of ATCA.

---

[*] http://www.narrabri.atnf.csiro.au/

Band	**16cm**	**4cm**	**15mm**	**7mm**	**3mm**
Code	**L/S**	**C/X**	**K**	**Q**	**W**
Freq(GHz)	1.1-3.1	3.9-11.0	16-25	30-50	83-105
Primary beam	$42'$-$15'$	$12'$-$4'$	$2'$	$70''$	$30'$
Synthesized beam	$9''$- $3''$	$3''$-$1''$	$0.5''$	$0.2''$	$2''$
Flux Sensitivity (μJy/beam)	4	3	5	33	83

Table 3.1: The different operating modes of ATCA; This table relates the different bands encoded as $L/S, C/X, K, Q$ and W with the various parameters such range of frequency, size of primary beam and synthesized beam and sensitivity.

3.5.2 Observations

The observation of the target source SS433, the three phase-leakage calibrators PKS 2029+121, PKS 1908-201, PKS 1947+079, and an amplitude calibrator PKS 1934-638 were carried out for 21 hours at three different bands of 16cm, 4cm and 7mm in the 6A array configuration of ATCA. The principal investigator for the ATCA proposal was Dr. M. Coriat. The other co-investigators were Dr. A. Tzioumis, Prof. R.Fender, Prof. P. Woudt and myself.

When we consider the linear feed of system of ATCA, we find that it is mainly the instrumental polarization leakages that corrupt the Stokes V flux densities by Stokes I, whereas the leakage terms of Stokes Q into Stokes U and V are due to gain errors (O'Sullivan et al. 2013). Given that ATCA has high precision polarimetry over a wide frequency, the objectives here are to obtain broad and accurate spectra of circular and linear polarization so that the particle content and the magnetic field structure of the jets can be constrained. The broadness of the spectral coverage will allow us to be precise on the average spectral index and to investigate multiple angular scales, in an attempt to search for the location of the CP emission.

In order to avoid any significant variability in the target source, the epoch of observations was proposed to be scheduled on consecutive days during a non-flaring period of SS433. Unfortunately, the observation at the 7mm band could not be scheduled consecutively before the observation of the 16cm band and the 4cm band. Additionally as there are large number of radio frequencies interferences (RFI) at 16cm band, the dual-feeds carried out the observations in the same frequency range. The deconvolution (see Section 3.5.3) of co-added frames at the same frequency allows a better estimation of flux densities with reduced noise and RFI. After the observation was done, I carried out data reduction for both the 16cm band and the 4cm band which is detailed in the next subsection. In this Chapter, I will present the results in section 3.6 for the 16 cm band and the 4cm bands only as we are still working on the 7mm dataset.

3.5.3 Flagging, calibration and deconvolution

Figure 3.9 shows the sequence in which the main data reduction steps should be carried out to reduce the ATCA radio data. These steps were carried out using the *MIRIAD*[*] data reduction pakage (Sault et al. 1995).

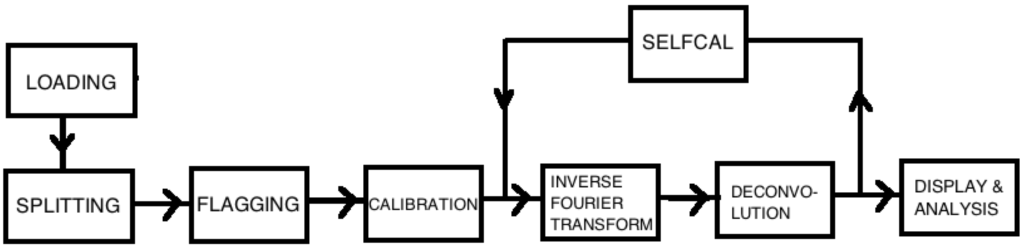

Figure 3.9: A general data reduction strategy; This is the sequence in which various tasks should be carried out. (See text for the function of these tasks).

The following summarizes the various tasks which were used to carry out the main data reduction steps. *Atlod* loads the files into miriad. *Uvsplit* splits the observations in terms of the observing bandwidth and sources. *Blflag* removes the defects in observed data (detailed below). *Gpcal* and *mfcal* carry out the process of 'correcting' the data for instrumental gain variations as a function of time and frequency (detailed below), and for instrumental polarization leakage. *Invert* performs the inverse Fourier transform of the uv-data to produce the so-called "dirty-map". *Clean* carries out the deconvolution steps to obtain a "clean" image of the field. *SelfCal* refers to the process of calibrating a dataset against a model image of the target source field in order to find for the calibrations that best match the data to the model. The model is obtained

---

[*] http://www.atnf.csiro.au/computing/software/miriad

by carrying out an initial imaging of the source (it is the output of the clean step).

Following O'Sullivan et al. (2013), I have split each band (1140 – 3060 MHz and 4540 – 9960 MHz) into sub-bands of bandwidth of 128 MHz. The instrumental polarization leakages, mentioned in Section 3.5.2, is indeed frequency dependant. However by slicing into sub-bands, the leakage terms at each frequency can be more accurately determined and hence any variation in the gain as well as the spectral slope can be rectified for the whole bandwidth of 2 GHz.

The removal of the bad data, which are due to radio frequency interference (RFI), instrumental defects and bad atmospheric conditions, is also known as **Flagging**. The flagging process was done manually using the interactive tasks *blflag* and *pgflag*. Flagging needs to be done without unnecessary loss of data. Therefore, I used multiple ways of displaying the data to precisely remove bad data as a function of channel, time and baseline.

The flagging process is carried out to all observed sources (target and calibrators). Given that the RFI at 16cm is severe, I carried out a global but light flagging and calibration before actually splitting into sub-bands of 128 MHz, to remove common defects spreading over all sub-bands. As I iterated through data reduction pipeline, I applied flagging more extensively and accurately for all sub-bands from both bands for the target source, the amplitude calibrator, and the phase-leakage calibrator.

The **Standard Calibration** process which is used to create an intensity map (Stokes I) is shown in Figure 3.10. This section on standard calibration is based on the miriad manual. The Miriad software models a feed of having a composite gain of:

$$g(t)g_p(\nu)exp(i2\pi\tau(t)(\nu - \nu_o)) \tag{3.6}$$

where $g(t)$ is a time variable complex number, $g_p(\nu)$ is the bandpass function, and τ is a time-variable delay term. The immediate response of a linearly polarized feed to polarized emission appears as the linear combination of two of the four Stokes parameters that describe the wave. In an ideal case, we find:

$$XX = I + Q \tag{3.7}$$

$$YY = I - Q \tag{3.8}$$

$$XY = U + iV \tag{3.9}$$

$$YX = U - iV \tag{3.10}$$

Note that for a telescope like the ATCA, the equations include the dependence of the parallactic angle χ as the feeds rotate with the equatorial frame (see Equations 3.11 to 3.14):

$$XX = I + Q\cos(2\chi) + U\sin(2\chi) \tag{3.11}$$

$$YY = I - Q\cos(2\chi) - U\sin(2\chi) \tag{3.12}$$

$$XY = iV - Q\sin(2\chi) + U\cos(2\chi) \tag{3.13}$$

$$YX = -iV - Q\sin(2\chi) + U\cos(2\chi) \tag{3.14}$$

In addition, for the non-ideal scenario, we observe the leakage of the Y component of the electric field into the X feed, D_X, and the leakage of the X component of the electric field into the Y feed, D_Y. These leakage terms D_X and D_Y can strongly affect our observation if ever we are measuring very weak signals as for the case of circularly polarized emission.

Figure 3.10 depicts our calibration strategy, where the calibration solutions are determined using two tasks: (i) *mfcal*: Multi-frequency calibration task, and (ii) *gpcal*: Gain calibration task. I carried out *mfcal* using the visibilities of PKS 1934-638 (assumed properly flagged) to solve for the bandpass function. Hence PKS 1934-638 is referred as the amplitude/bandpass calibrator. The bandpass function is the gain as a function of frequency i.e. the "$g_p(\nu)$" term in the Equation 3.6. The calibration tables obtained with *mfcal* are copied to one of the phase-leakage calibrators (PKS 2029+121, PKS 1908-201 or PKS 1947+079). Then I performed the task *gpcal* to determine the gain solutions and leakage terms using the phase calibrator. When all the standard calibrations are done, I then re-scaled the flux densities and correct for the bandpass slope using the miriad tasks *gpboot* and *mfboot* respectively. These solutions are then copied to our target source SS433 for deconvolution and imaging.

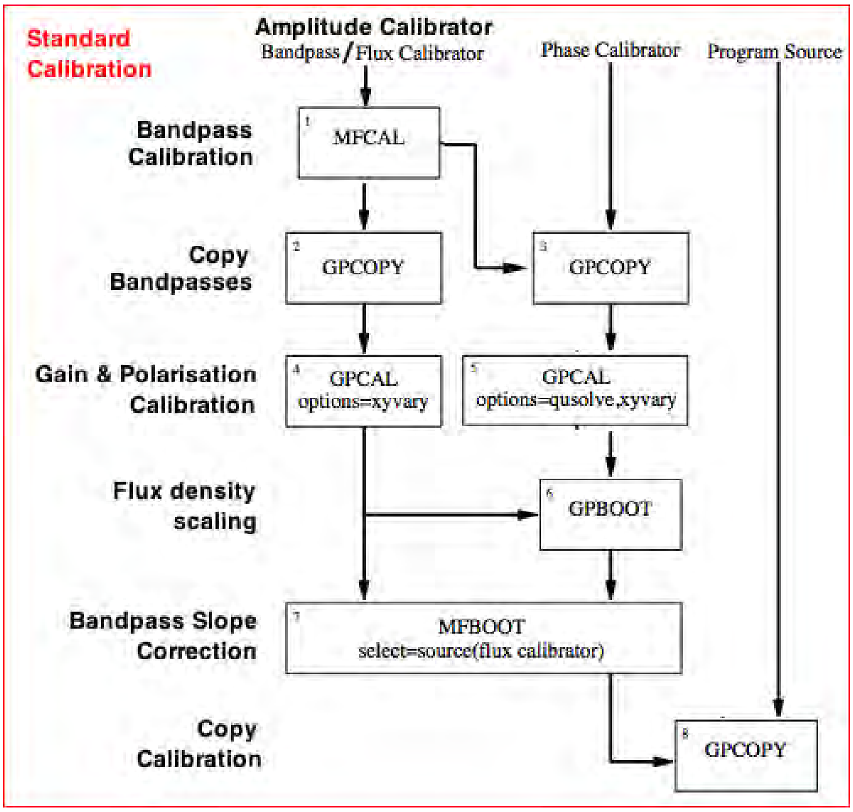

Figure 3.10: The general standard calibration strategy. The process entails the following sequence: The bandpass calibration of the amplitude calibrator, copying the bandpass solution to the phase calibrator, gain and polarization calibration of the phase calibrator, re-scaling of flux densities for the phase calibrator, correction of bandpass slope and finally copying the calibration solutions to the target. Key concepts derived from Sault et al. (1995).

The calibration process which is used to estimate Stokes V differs from the standard calibration. The non-standard calibration which I followed was derived from Rayner et al. (2000) and his user guide on circular polarization (Rayner 2000). The departures are outlined as follows. The gain calibration solutions for the phase calibrator needs to be determined using the "strongly polarized" equation. This also requires the phase calibrator to be unresolved and linearly polarized to some extent (Rayner et al. 2000). The phase-leakage calibrators PKS 1908-201, and PKS 1947+079 were eventually not considered as their *gpcal* calibration solutions were not stable, whereas PKS 2029+121 has shown to be strongly linearly polarized (in Stokes Q), and therefore it can be used to determine any leakage terms with adequate confidence

Note that for a circular polarisation experiment, during the primary stage, *gpcal* is used to solve the weakly polarised equation on PKS 1934-638. This sets the circular polarization of the amplitude calibrator as zero-point i.e Stokes V=0 for PKS 1934-638 (assumed to be non circularly polarized). However, the gain and leakage calibration carried out using the phase-leakage calibrator corrupts this zero-point which was set initially. The process of correcting for this corrupted zero-point was also carried out but the description is beyond the scope of this Chapter; the reader is directed to Rayner et al. (2000) for more details.

The calibration process of the phase leakage calibrator is verified by e.g. displaying the variation of the amplitude and phase of the gain solutions for the XY crosscorrelation as a function of time and antenna (see Figure 3.11 for an example). The solutions are copied to the target source SS433, which is then flagged before the next phase. Figure 3.12 show the variation of the calibrated flux densities (amplitude) of SS433 with time at the sub-band 5436 MHz for all baselines.

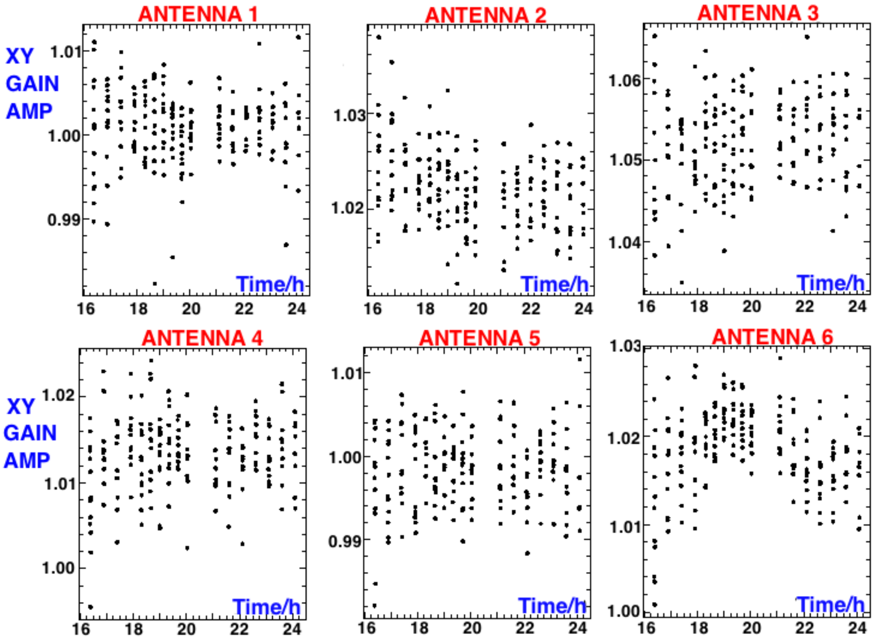

Figure 3.11: Verification of the calibration process in the sub-band 5436 MHz for all antenna; The variation of the amplitude and phase of the gain solutions for the XY crosscorrelation for the phase calibrator PKS 2029+121 as a function of time and antenna

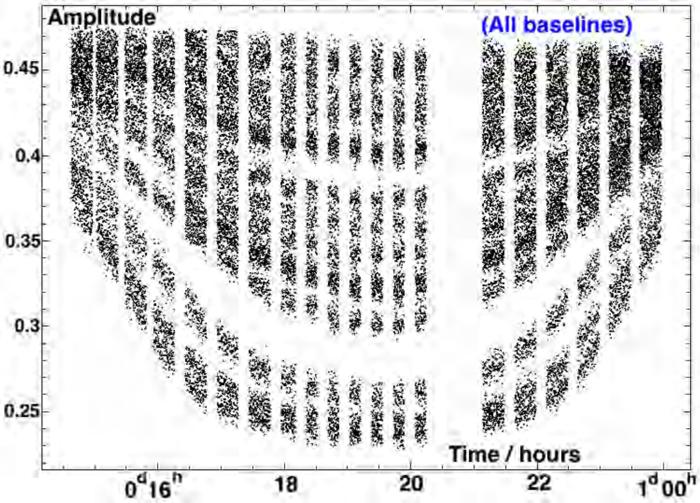

Figure 3.12: The variation of the calibrated visibilities (amplitude) of SS433 with time at the sub-band 5436 MHz for all baselines

The imaging process* starts after the calibration as shown in Figure 3.9. The first step of the imaging process is to inverse Fourier transform the visibility datasets to produce the image cube. This is carried out by the miriad task *invert*. The *invert* task can grid the exact location of various channels on the (u-v) plane for a range of frequencies (rather than some average location). For the bandwidth of 128 MHz of each sub-band, the multi-frequency synthesis (MFS) technique of this task will create an single continuum image with an averaged frequency over the sub-band.

Since the synthesis arrays will produce a (u,v) sample using dicrete locations, we don't know how the source intensity distribution will be Fourier-transformed. The observed visibility datasets can be considered as the product of the real visibilties $V(u,v)$ and a sampling function $S(u,v)$. The convolution theorem (see Equation 3.15) states that the Fourier transform of the sampled distribution (the dirty image, I_D) is equal to the convolution of the Fourier transform of the true source visibility distribution (the true image, I) and the Fourier transform of the sampling function (the dirty beam, B_0):

$$I_D(l,m) = I(l,m) * B_o(l,m) \fallingdotseq V(u,v) \times S(u,v) \tag{3.15}$$

---

*Inspired from the miriad manual at http://www.atnf.csiro.au/computing/software/miriad userguide/node106.html

Where $*$ means convolution and $\fallingdotseq$ means Fourier transform. The visibilities for target source SS433 (shown in Figure 3.12) was inverse-Fourier transformed to produce a dirty beam B_0 and dirty map I respectively. The miriad task *clean* then carries out the deconvolution process to produce a model image. The *clean* algorithm searches iteratively for the brightest pixel within a specified region and then subtracts 0.1 of the dirty beam from the dirty image at the point where the brightest pixel is situated. This is how the "model" is generated. The task *restor* reconstructs the final image produced by convolving this obtained model with a gaussian beam (see left of Figure 3.13).

Finally, when we have obtained the image, the flux densities of the target source in the image can be determined by fitting a point source model at the source location in order to estimate its flux densities. The residual image as shown on right side of Figure 3.13 is a by product of the fitting process which is used to check the quality of the fit.

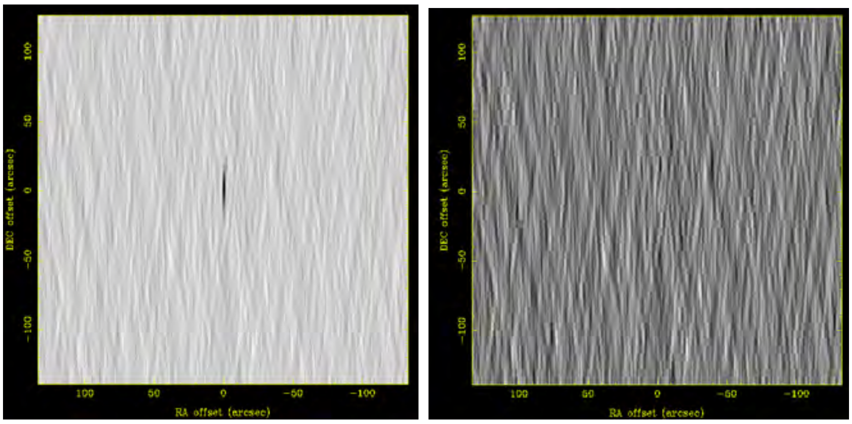

Figure 3.13: The image of SS433 at the sub-band of 5436 MHz on the left and its residual image on the right; The image was produced by using the miriad task *restor*. The residual image is the remainder after substracting the estimated flux densities at the location of that peak value. The flux densities of SS433 at 5436 MHz was estimated as $(-5.5 \pm 0.4) \times 10^{-4}$Jy in Stokes V.

Note: (i)The Imaging process is same for both Stokes I and Stokes V.

(ii) Because simultaneous observations were made at 16cm band, the inverse-Fourier transform process (using *invert*) requires the co-addition of both visiblities at the same sub-band to produce one single dirty map and one single dirty beam.

3.6 Result and analysis

In this section, I present my results with the aims of constraining the particle composition (see Section 1.6.4) of the jets of SS433 using circular polarization (CP) and the dominant mechanism for the origin of CP emission (see Section 3.4). This was done by observing the flux densities of SS433 in Stokes V over a broad range of frequencies so as to obtain a spectrum for fractional CP (see Figure 3.16). The spectral index which has been constrained from this spectrum, could therefore be used to determine which mechanism seems to be dominant or not. From the underlying theories of that mechanism, I attempted to constrain the energy content and constrain the particle content for jets of SS433.

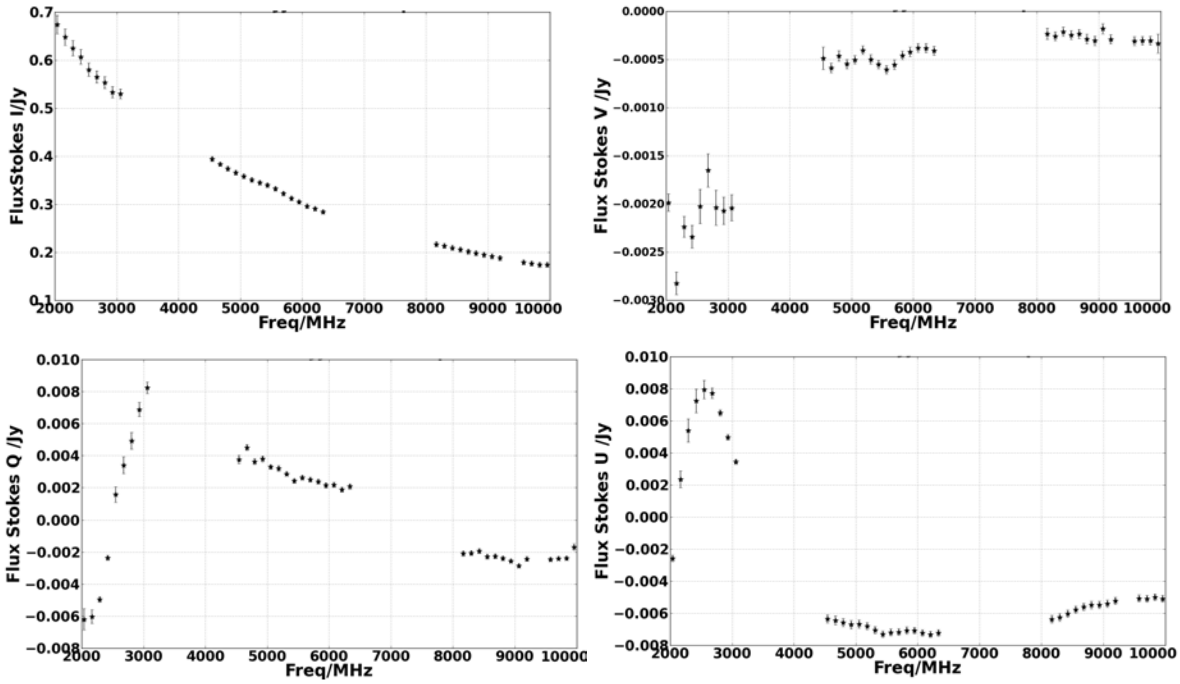

Figure 3.14: Flux densities of SS433 as a function of frequency for each Stokes parameters (I, V, Q and U) within the bandwidth 1140 to 9960 MHz. The negative value of flux densities in Stokes V means clockwise. We also find the effect of large RFI and loss of ATCA sensitivity to cause large error bars at lower frequencies as well.

After all the data reduction were carried out, all the estimated flux densities and associated errors in Stokes I, V, Q and U for each sub-bands of 128 MHz ranging from 1140 to 9960 MHz have been summarised in the Tables 3.2 and

3.3 below. Figure 3.14 and Figure 3.15 shows SS433 spectra in each Stokes parameters. The negative value of flux densities in Stokes V means clockwise polarization. As mentioned in Section 3.5.2, there are larger amount of RFI and ATCA also loses in sensitivity (Table 3.1) at lower frequency. This can account for larger error bars between 1140 to 3060 MHz.

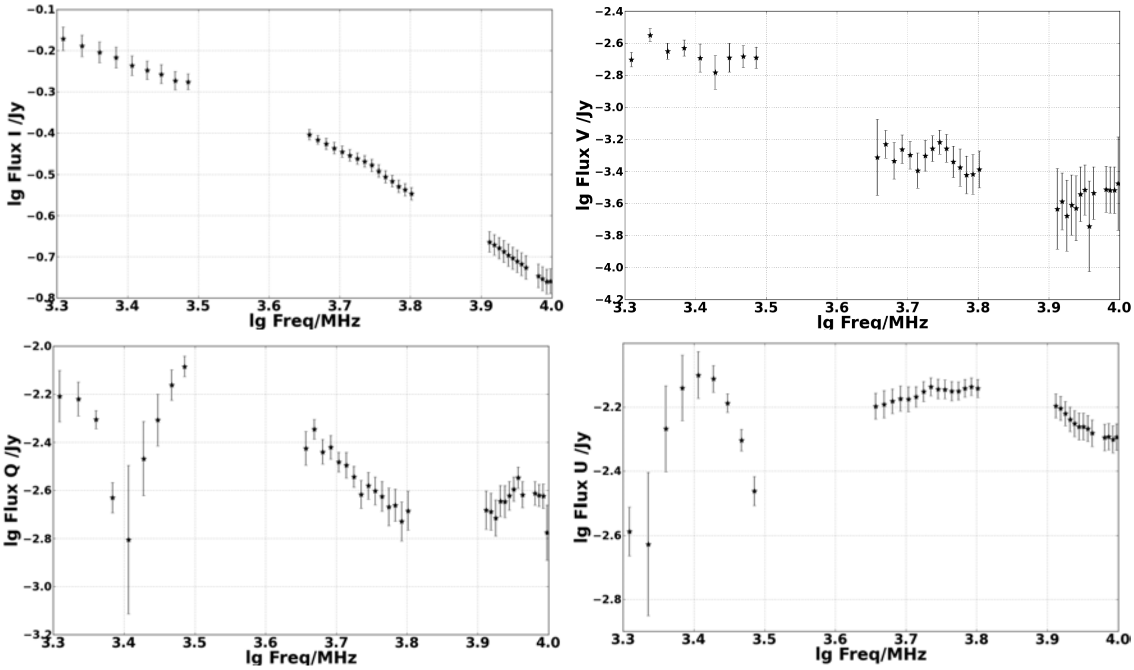

Figure 3.15: Logarithmic flux densities of SS433 as a function of logarithmic frequency for each Stokes parameters (I, V, Q and U) within the bandwidth 1140 to 9960 MHz.

It is useful to express the flux densities of various Stokes parameters V, Q and U in terms of the total intensity I, so that it gives us a better idea of the fraction of polarization and also enables us to compare the amount of circular polarization as compared to linear polarization at given frequency. The fractional circularly polarized flux densities is given by $m_c = |V|/I$ while the fractional linear polarized (LP) flux densities $m_l = \sqrt{Q^2 + U^2}/I$. Both the CP flux densities and the LP flux densities are frequency dependent. Following O'Sullivan et al. (2013), the associated error in m_c is calculated as $\sigma^2_{m_c} = \left(\frac{\sigma_V}{I}\right)^2 + m^2_{c,1934}$. σ_V is the error in CP flux density measurement, and $m_{c,1934}$ account for any potential contamination of the amplitude calibrator with a small amount of CP flux density (see non-standard calibration in Section 3.5.2).

The error in m_l is estimated from standard propagation of errors as:

$$\sigma^2_{m_l} = \left(\frac{\sigma^2_Q}{Q^2+U^2}\right)\cdot\left(\frac{Q^2}{I^2}\right)+\left(\frac{\sigma^2_U}{Q^2+U^2}\right)\cdot\left(\frac{U^2}{I^2}\right)+\left(\frac{Q^2+U^2}{I^2}\right)\cdot\left(\frac{\sigma^2_I}{I^2}\right) \quad (3.16)$$

Given the fact that we have the flux densities for all Stokes parameters at each sub-band of 128 MHz ranging from 1140 to 9960 MHz as shown in Figure 3.14, we can obtain a spectrum of fractional circular polarisation and a spectrum of fractional linear polarisation. These spectra are shown in Figure 3.16 and on the left panel of 3.17. The flux densities in Stokes I is greater by two orders of magnitude than the flux densities in Stokes V. The value of fractional circular polarization is hence usually relatively small and therefore this explains why we chose such telescope with stable polarimetric feed like ATCA.

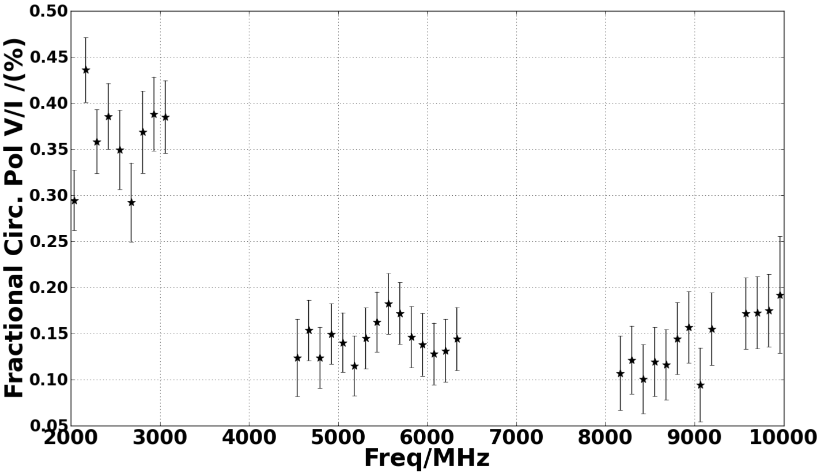

Figure 3.16: The spectrum of fractional circular polarization $m_c = |V|/I$. Following O'Sullivan et al. (2013), the error for m_c is defined as $\sigma^2_{m_c} = \left(\frac{\sigma_v}{I}\right)^2 + m^2_{c,1934}$.

The left panel of Figure 3.17 shows that the fractional linear polarization is relatively higher than the fractional circular polarization for the same total intensity I and same bandwidth. There is a gradual increase of linear circular polarization from 0.1% at low frequencies of 2 − 3 GHz to 0.3% at higher frequencies of 9 − 10 GHz. Since linear polarization deals with the two Stokes parameters Q and U, we can determine a sense of orientation of Stokes Q with respect to Stokes U which is known as the **polarization angle** Ψ, by taking the $\frac{1}{2}\arctan(U/Q)$. The polarization angle Ψ is also frequency-dependent. The right panel of Figure 3.17 shows the estimates of polarization angle Ψ as a function of frequency. The error in the polarization angle σ_Ψ is given by propagation of errors as follows:

$$\sigma_\Psi = \frac{1}{2}\sqrt{\frac{Q^2\sigma_U^2}{(Q^2+U^2)^2} + \frac{U^2\sigma_Q^2}{(Q^2+U^2)^2}} \tag{3.17}$$

Since I now have a spectrum for fractional circular polarization m_c , the next step is to find the relation between m_c and the frequency ν in the form of a powerlaw $m_c \propto \nu^\alpha$ as mentioned in Section 3.3. In other words, we need to find the spectral index α, which will indicate us the plausible mechanism for CP emission.

In order to obtain more accurate estimates of α, the average flux densities in Stokes V and I were deduced by the deconvolution of co-added frames for 3 subsamples of sub-bands (of 128 MHz). The 3 subsamples have 13, 15 and 18 frames corresponding to frequency range $8-10$ GHz, $4.5-6.5$ GHz and $2-3$ GHz (Dual-feed observations were taken; see Section 3.5.2) respectively. The Figure 3.18 shows a best fit to the $\log_{10}(m_c)$ dataset against $\log_{10}(\nu)$ dataset, for those values of V and I which corespond to the 3 subsamples of sub-bands.

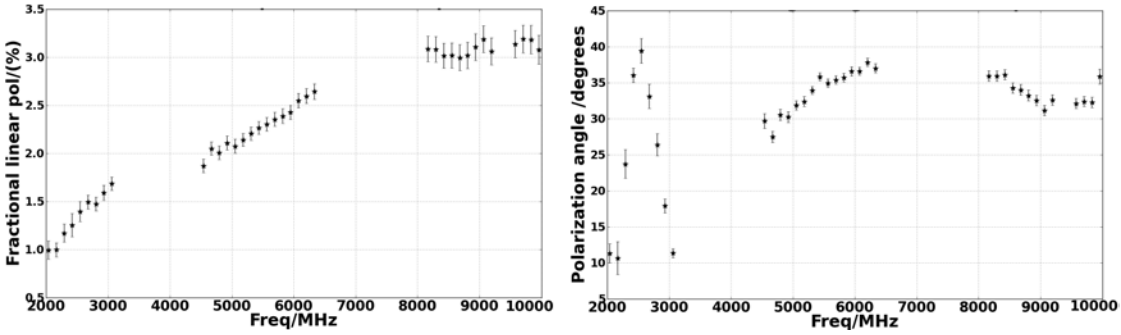

Figure 3.17: The spectrum of fractional linear polarization $m_l = \sqrt{Q^2+U^2}/I$ is shown on the left panel. The error for m_l is defined as in Equation 3.16. The polarization angles $\Psi = \frac{1}{2}\arctan(U/Q)$ as function of frequency is shown on the right panel and the errors σ_Ψ is given by Equation 3.17

The spectral index of this best fit was constrained to $\alpha = -0.94 \pm 0.18$ by minimising the χ^2 of the power law function. This spectral index of $\alpha =$

-0.94 ± 0.18 corresponds to the observation of SS433 during a non-flaring period. However, this obtained value is similar to the value of $\alpha = -0.9 \pm 0.1$ from Fender et al. (2000) for the observation taken during a flaring period. This could indicate that value of spectral index α is independent of flaring.

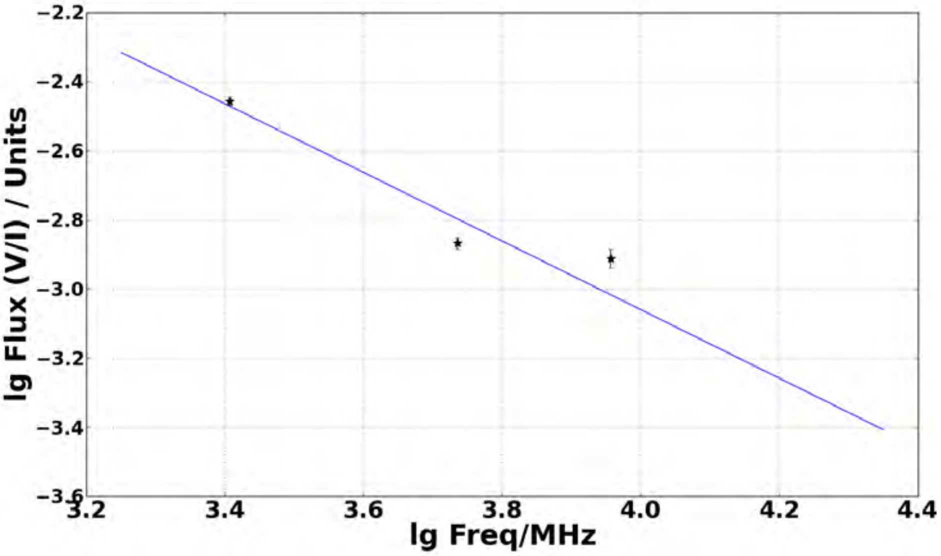

Figure 3.18: A power law fit to the fractional CP spectrum; The average flux densities in Stokes V and I were obtained by the deconvolution of co-added frames for 3 subsamples (13, 15 and 18 frames respectively) of sub-bands of 128 MHz. The spectral index of this best fit was constrained to $\alpha = -0.94 \pm 0.18$ by minimising the χ^2 of the powerlaw function $m_c \propto \nu^\alpha$.

Having obtained a value for the spectral index, I make an attempt to constrain the dominant mechanism which could be the origin of circularly polarized emission in SS433. The reader is directed to section 3.4 for a quick review on the various CP production mechanisms. Following Fender et al. (2000), I also consider only two CP mechanisms, namely (i) *Intrinsically circularly polarised synchrotron emission* and (ii) *Faraday conversion* or referred as *Propagation-induced circular polarization.* The coherent radiation mechanism, from Section 3.4, is an intrinsically narrow band phenomena, therefore it cannot explain the CP continuum we observe from 2 to 10 GHz. The production of circular polarization by scintillation mechanism requires a turbulent magnetic medium. This mechanism produces a fluctuating CP signal on timescale of minutes to few hours which should lead to a time-averaged CP of zero. It also imposes stringent constraints on the nature, size and distance to the source of the birefringent screen Wardle & Homan (2001). We therefore consider this mechanism unlikely to be dominant in our case but we will investigate this possibility further at a later stage. The intrinsically circularly polarised synchrotron emission models the power law in the form of $m_c \propto \nu^{-1/2}$ whereas the Faraday conversion takes the form of $m_c \propto \nu^{-1}$ or for highly relativistic cases: $m_c \propto \nu^{-3}$. Therefore, the value of $\alpha \simeq -1$ might suggest that Faraday conversion seems to be the dominant form of CP production in SS433. However, the power law fit and the spectral index do not seem to be an adequate evidence to confirm Faraday conversion as the CP production mechanism.

3.7 Discussion

3.7.1 Selection of data

Despite the fact that ATCA observations were carried from frequency 1498 MHz (16cm band) to 42827.4 MHz (7mm band), all of the data at 1400-2000 MHz are unusable due to strong RFIs and the loss in sensitivity of the telescope respectively. The full band at 7mm could not be included in results and analysis because we are still processing the mm data which is much more complex to reduce.

3.7.2 Constraint on CP production mechanism

The value α of -0.94 ± 0.18 (from Figure 3.18) is not appropriate for its use to constrain Faraday conversion as the main form of the CP mechanism, for which the index ought to be varying from -1 up to -3 for highly relativistic cases. In our case, we should expect the value of α to be ≥ 1 since the jets of SS433 are known to be indeed relativistic ($0.26c$). Different plausible explanations which may be given to account for this discrepency. There may be more than one CP mechanism at play where there is co-dominance of the Faraday conversion and intrinsically synchrotron mechanism. The spectrum of the fractional CP would therefore be a combination of both contributions. Alternatively, it could also be that the relativistic conditions of plasma for the jets of SS433 at the speed of $\beta \sim 0.26c$ are not strong enough to cause the

$|\alpha| > 1$, hence the value obtained is not good enough to constrain the Faraday conversion mechanism. In addition, due to lack of high spatial resolution in this context, the origin and location of CP emission still remain unanswered. Therefore, we cannot determine if we are observing the emission from one and only component producing both Stokes I and stokes V signals (as it should be if we want to compare with ideal case describe in the theory). In short, the question of dominant CP production mechanism in SS433 remain unanswered and need to be investigated through other methodologies.

Table 3.2: The estimated flux densities-part I; This table shows only the sub-bands ranging from (1140-5564) MHz only. After all the data reduction were carried out, all the estimated flux densities and associated errors in Stokes I, V, Q and U for each sub-bands of 128 MHz have been recompiled here. The flux densities are given in Jy.

freq	**Stokes I**	$\mathbf{I}_{err}$	**Stokes V**	$\mathbf{V}_{err}$	**Stokes Q**	$\mathbf{Q}_{err}$	**Stokes U**	$\mathbf{U}_{err}$
1140	0.863	1.9E-02	-1.71E-03	6.3E-04	5.41E-03	2.9E-03	5.19E-03	9.7E-04
1268	0.865	2.9E-02	-2.72E-03	2.2E-04	1.57E-03	1.2E-03	-1.29E-03	3.3E-04
1396	0.833	3.3E-02	-6.76E-04	1.5E-04	-3.82E-03	6.8E-04	-6.24E-04	4.0E-04
1524	0.795	2.8E-02	-1.39E-03	2.6E-04	-2.53E-03	2.2E-03	5.86E-03	7.7E-04
1652	0.747	2.4E-02	-2.02E-03	1.1E-04	5.51E-03	4.9E-04	1.32E-03	2.6E-04
1780	0.729	2.4E-02	-1.84E-03	1.2E-04	2.91E-03	2.2E-04	-4.52E-03	9.3E-04
1908	0.697	1.9E-02	-1.77E-03	1.4E-04	-3.28E-03	7.0E-04	-5.31E-03	4.0E-04
2036	0.674	1.9E-02	-1.984E-03	8.8E-05	-6.19E-03	6.5E-04	-2.58E-03	1.9E-04
2164	0.648	1.6E-02	-2.82E-03	1.1E-04	-6.02E-03	4.2E-04	2.36E-03	5.2E-04
2292	0.624	1.6E-02	-2.23E-03	1.0E-04	-4.95E-03	1.8E-04	5.39E-03	7.2E-04
2420	0.606	1.5E-02	-2.34E-03	1.1E-04	-2.34E-03	1.4E-04	7.25E-03	7.4E-04
2548	0.580	1.4E-02	-2.02E-03	1.7E-04	1.57E-03	4.8E-04	7.95E-03	5.7E-04
2676	0.565	1.3E-02	-1.65E-03	1.7E-04	3.40E-03	5.2E-04	7.73E-03	3.2E-04
2804	0.553	1.3E-02	-2.03E-03	1.8E-04	4.92E-03	5.2E-04	6.49E-03	1.8E-04
2932	0.533	1.2E-02	-2.07E-03	1.4E-04	6.88E-03	4.3E-04	4.97E-03	1.6E-04
3060	0.529	1.0E-02	-2.04E-03	1.3E-04	8.24E-03	3.5E-04	3.45E-03	1.5E-04
4540	0.394	4.9E-03	-4.87E-04	1.1E-04	3.76E-03	2.6E-04	-6.35E-03	2.5E-04
4668	0.383	4.1E-03	-5.88E-04	5.1E-05	4.51E-03	1.8E-04	-6.43E-03	2.7E-04
4796	0.374	5.1E-03	-4.63E-04	5.3E-05	3.63E-03	1.8E-04	-6.58E-03	2.5E-04
4924	0.365	5.0E-03	-5.47E-04	4.8E-05	3.79E-03	1.8E-04	-6.71E-03	2.6E-04
5052	0.358	4.9E-03	-5.02E-04	4.3E-05	3.29E-03	1.3E-04	-6.67E-03	2.5E-04
5180	0.351	4.9E-03	-4.03E-04	4.4E-05	3.19E-03	1.6E-04	-6.79E-03	2.1E-04
5308	0.344	4.7E-03	-4.99E-04	4.8E-05	2.86E-03	1.2E-04	-7.05E-03	2.2E-04
5436	0.339	4.8E-03	-5.51E-04	4.4E-05	2.42E-03	1.4E-04	-7.31E-03	2.0E-04
5564	0.332	4.7E-03	-6.05E-04	4.5E-05	2.63E-03	1.4E-04	-7.19E-03	2.1E-04

Table 3.3: The estimated flux densitieses-part II; This table shows only the sub-bands ranging from (5692-9960) MHz only. After all the data reduction were carried out, all the estimated flux densities and associated errors in Stokes I, V, Q and U for each sub-bands of 128 MHz have been recompiled here. The flux densities are given in Jy.

freq	**Stokes I**	**I**$_{err}$	**Stokes V**	**V**$_{err}$	**Stokes Q**	**Q**$_{err}$	**Stokes U**	**U**$_{err}$
5692	0.322	4.6E-03	-5.54E-04	4.8E-05	2.49E-03	1.4E-04	-7.17E-03	2.1E-04
5820	0.312	4.6E-03	-4.56E-04	4.4E-05	2.37E-03	1.4E-04	-7.07E-03	2.1E-04
5948	0.304	4.3E-03	-4.20E-04	4.8E-05	2.14E-03	1.6E-04	-7.08E-03	2.0E-04
6076	0.296	4.4E-03	-3.78E-04	4.4E-05	2.17E-03	1.4E-04	-7.23E-03	1.9E-04
6204	0.291	4.3E-03	-3.81E-04	4.6E-05	1.86E-03	1.5E-04	-7.31E-03	1.9E-04
6332	0.284	4.3E-03	-4.09E-04	4.6E-05	2.07E-03	1.6E-04	-7.22E-03	2.0E-04
6460	0.285	4.5E-03	-4.64E-04	8.0E-05	-6.61E-04	1.9E-04	-7.58E-03	1.8E-04
8040	0.223	6.0E-03	-4.88E-04	1.2E-04	-1.18E-03	2.7E-04	-6.32E-03	2.3E-04
8168	0.217	5.4E-03	-2.32E-04	5.8E-05	-2.08E-03	1.6E-04	-6.36E-03	2.3E-04
8296	0.213	5.3E-03	-2.58E-04	4.5E-05	-2.05E-03	1.5E-04	-6.25E-03	2.4E-04
8424	0.210	5.4E-03	-2.10E-04	4.6E-05	-1.93E-03	1.4E-04	-6.01E-03	2.3E-04
8552	0.207	5.5E-03	-2.45E-04	4.5E-05	-2.27E-03	1.5E-04	-5.77E-03	2.2E-04
8680	0.201	5.4E-03	-2.33E-04	4.7E-05	-2.26E-03	1.5E-04	-5.59E-03	2.2E-04
8808	0.198	5.3E-03	-2.86E-04	4.9E-05	-2.39E-03	1.4E-04	-5.48E-03	2.3E-04
8936	0.195	5.3E-03	-3.04E-04	4.7E-05	-2.55E-03	1.3E-04	-5.48E-03	2.3E-04
9064	0.192	5.3E-03	-1.80E-04	5.0E-05	-2.84E-03	1.2E-04	-5.41E-03	2.2E-04
9192	0.188	5.4E-03	-2.91E-04	4.7E-05	-2.42E-03	1.3E-04	-5.22E-03	2.2E-04
9448	0.182	5.1E-03	-2.93E-04	4.8E-05	-6.04E-03	1.2E-03	-5.06E-03	2.2E-04
9576	0.179	5.1E-03	-3.08E-04	4.4E-05	-2.44E-03	1.1E-04	-5.07E-03	2.1E-04
9704	0.177	5.1E-03	-3.04E-04	4.4E-05	-2.40E-03	1.0E-04	-5.09E-03	2.1E-04
9832	0.174	5.2E-03	-3.04E-04	4.4E-05	-2.38E-03	1.2E-04	-4.99E-03	2.1E-04
9960	0.174	5.2E-03	-3.34E-04	9.7E-05	-1.68E-03	1.9E-04	-5.08E-03	2.1E-04

Chapter 4

Conclusion and future work

In my conclusion, I summarize my work and present a concise overview of the results that were produced. I also provide my concluding remarks for both previous chapters and make few suggestions for future work in this area of research.

4.1 The impact of mass of stellar BH on the radio/X-ray correlation

The radio/X-ray correlation diagram, for BHXBs in the hard state, depicts the connection that exists between the radio jets and X-ray emitting accretion discs. Gallo et al. (2012) has provided us with the statistical evidence that the universal correlation has to be disregarded. The updated version of the radio/X-ray correlation diagram as shown in Figure 2.3 shows two populations of BHXBs (Corbel et al. 2013). These two populations belong to two different correlations ($F_{rad} = \kappa F_x^b$), where one population is considered as the standard (with power law index $b \sim 0.7$) and the other population is considered as outliers (with power law index $b \sim 1.4$). *The key question is to explain the existence of these two tracks.* Following the work of Soleri & Fender (2011) and Fender et al. (2010), we have adopted the same methodology of using the radio/X-ray normalisation to investigate the mass of the BH (analogous to spin, orbital period, and other binary parameters) with our sample of 17 BHXBs (see Table 2.1).

In addition, I have also re-investigated the inclination and orbital period with this sample as it includes recently detected sources. The top and bottom panels of Figure 2.7 shows that there is no correlation of these radio-X normalisation values with inclination as well as with orbital period respectively. The spearman correlation coefficient was estimated for the plot of the inclination against radio/X-ray normalisation, and it was found to be -0.20 ± 0.55. Similarly the spearman correlation coefficient was estimated as -0.27 ± 0.40, for the plot of the orbital period and radio/X-ray normalisation. Our results seems to conform with the work of Soleri & Fender (2011) since the values of the coefficient are close to zero. The Spearman correlation coefficient seems to be a reliable tool to verify the strength of such correlation.

Similiarly I investigated for the mass of the BH as a key parameter. In order to do that, I have compiled the most up-to-date mass estimates from the literature for the 17 BHXBs. The values and corresponding references are listed in Table 2.1. Figure 2.8 shows **all** our sources for which we have a radio/X-ray normalisation and mass of the compact object. The Spearman correlation coefficient is calculated to be $\Omega \sim 0.28 \pm 0.25$. However when our sample is restricted using well defined selection criteria, the correlation becomes clearer. The selection criteria considers only LMXBs whose mass were estimated dynamically, and exclude sources for which only quiescent measurements are available. Figure 2.10 shows our correlation diagram for the radio/X-ray normalisation against the mass of BH but chosen within a well defined set of selection criteria. The Spearman correlation coefficient was found to be $\Omega \sim 0.78 \pm 0.01$ which means that the set of selection criteria has strengthened this correlation ($\Omega \rightarrow 0.0$ means no correlation and $\Omega \rightarrow \pm 1.0$ means ideal correlation).

It can be argued that such correlation between radio/X-ray normalisation and the mass is merely yet another form of the Equation 2.3, which describes the fundamental plane of Black holes activity (see Figure 2.2 in Section 2.1). Therefore instead of using exactly the estimated radio/X-ray normalisation values, I remove this bias by subtracting this mass dependence that orignates from the fundamental plane (see Equation 2.7) to obtain the 'corrected' normalisation η. Table 2.1 also shows both the corrected η and uncorrected κ normalisation values. One can notice that those corrections, as indicated in

Equation 2.7, are actually small. After having subtracted the mass dependence from the fundamental plane, I still observe a correlation between the corrected normalisation, η with the masses of the compact BH (See Figure 2.11). The Spearman Rank correlation coefficient is then found to be $\Omega \sim 0.73 \pm 0.01$. Therefore a good correlation still exists and this gives us confidence for our results.

In short, we are led to conclude at least one of the following with full consideration of uncertainities in mass: (i) All the reported stellar masses of the BHs are insufficiently accurate to infer its impact on radio/X-ray correlation diagram, (ii) the estimated radio-X normalizations are inaccurate, firstly, due lack of associated errors in observational data for their simultaneous evolution of radio and X-ray fluxes for some of the sources and secondly, some sources similar to H1743-322, are still in transition from one track to another, (iii) the value of this Spearman Rank correlation coefficient $\Omega \sim 0.78 \pm 0.01$ (Figure 2.10) is reliable enough to suggests that the tested parameters have a significant degree of correlation since the value of the coefficient is close to 1.0 (ideal case). The latter would imply that the mass of BH is indeed the key property in BHB systems that influences which track (standard or outliers) the source belongs to on a radio/X-ray correlation diagram.

Our sample consists of only 17 sources and may not be fully representative for the general behaviour of all BHXBs that exist. However, I deduce the following. From the correlation diagram in Figure 2.10, one can infer that sources with more (less) massive BH tend to have higher (lower) radio/X-ray normalisation $\log(\kappa)$. This may imply that BHXBs with a massive BH will tend to populate the standard track whereas BHXBs with a less massive BH will tend to populate the outliers' track.

I find that, at a given X-ray luminosity (proxy for accretion-power), BHXBs with a more massive BH (on the standard track) are observed with higher emission of radio luminosities. Similarly, BHXBs with less massive BH (on the outliers' track) are observed with lower emission of radio luminosities. This may imply that BHXBs with more (less) massive BH will have more (less) powerful jets. Coriat et al. (2011b) proposed that those hard state BHXBs which are radiating efficiently occupies the outliers' track whereas the BHXBs on the stardard track are actually radiating inefficiently. An alternative possibility to the less/more powerful jets (as mentioned above) is that hot inner accretion flow seem to be radiatively more (less) efficient if the BH is less (more) massive. This should be valid for at least with a given range of luminosity, because there are cases e.g. H1743-322 where the source can change its track. Lastly, since the viscosity parameter of the disc is not related to mass of BH, I find that viscosity probably plays no critical role in explaining the dual radio/X-ray correlations, if the mass dependence reported here holds.

As a future work, this result should be further confirmed once additional and more accurate mass measurement will be available. This correlation could be investigated with statistical tools other than Spearman correlation coefficient. This study could be extended with a larger sample of X-ray binaries. The radio/X-ray correlation diagram in Figure 2.3 by Corbel et al. (2013) can also be improved. In Figure 2.3, one can find that at low radio luminosities for two orders of magnitude, most of the datapoints have an upper limit. In future, MeerKAT/ThunderKAT will be an appropriate instrument to observe the radio luminosities of these sources since it will have the required sensivity to observe the radio flux density of BHXBs in the quiescent hard state.

4.2 Jet composition of SS433 using the radio broadband circular polarized spectrum

SS433 is one of the exotic black hole X-ray binaries that exists. It is an interesting source to focus on for the studies of accretion and outflow mechanisms, since it has a supercritical accretion disc, and displays precessing relativistic jets. The key question is to *find whether these jets are made up of either proton-electron plasma or electron-positron plasma using circular polarization* (see Section 1.7.5). The radio circular polarization (CP) is a good diagnostics for the study of particle composition of jets. Therefore we have observed the circular polarized flux densities of SS433 using ATCA for a broad range of frequencies. The observation of the target source SS433, three phase-leakage calibrators PKS 2029+121, PKS 1908-201, PKS 1947 +079 and an amplitude calibrator PKS 1934-638 were carried out for 21 hours at five different bands of 16cm, 4cm, and 7mm in the 6A array configuration of ATCA.

I carried out the flagging, the calibration and the deconvolution of these observations using the *MIRIAD* Data Reduction pakage (Sault et al. 1995). The different miriad tasks were compiled in bash script, which were run to perform data reduction process. Following O'Sullivan et al. (2013), we have also split each band (1140−9960 MHz) into sub-bands of bandwith of 128 MHz. The Non-standard Calibration which we carried out was derived from Rayner et al. (2000) and his userguide on circular polarization Rayner (2000). After all the data reduction were carried out, all the estimated fluxes and associated errors in Stokes I, V, Q and U for each minibands of 128 MHz ranging from 1140 to 9060 MHz have been recompiled in the Tables 3.2 and 3.3. The Figure 3.14 depicts the flux densities of SS433 as a function of frequency for each Stokes parameters (I, V, Q and U) within the same bandwidth (1140 to 9960 MHz). We also find the effect of large RFI and loss of ATCA sensitivity to cause large error bars at lower frequencies as well.

It is useful to express the fluxes of various Stokes parameters V, Q and U in terms of the total intensity I. The fractional circularly polarized (CP) flux is given by $m_c = V/I$ while the fractional linear polarized (LP) flux $m_l = \sqrt{Q^2 + U^2}/I$. Both the CP flux and the LP flux are frequency dependent. Therefore from the observations, a spectra of fractional CP (%) and fractional LP (%) was constructed as shown in Figure 3.16 and left side of Figure 3.17 respectively. The right side of Figure 3.17 shows the estimates of polarization angle Ψ for linear frational polarization. The polarization angle Ψ changes significantly at low frequency and it would be interesting to investigate this further by estimating the rotation measure if possible in future.

I am more interested in the spectral index from the CP spectrum since it helps us to constrain the CP production mechanism. The spectral index of this best fit was constrained to $\alpha = -0.94 \pm 0.18$ by minimising the χ^2 of the power law function (See Figure 3.18). This spectral index of $\alpha = -0.94 \pm 0.18$ corresponds to the observation of SS433 during a non-flaring period. However, there is still nearly same value of $\alpha = -0.9 \pm 0.1$ from Fender et al. (2000) for the observation during a flaring period. This could indicate that value of spectral index α is independent of flaring.

The various CP Production mechanisms are reviewed in Section 3.4. As stated earlier, the spectral index was found to be $\alpha = -0.94 \pm 0.18$ for bestfit of $\log(m_c)$ against the $\log(\nu)$. The value of $\alpha \simeq -1$ suggest that Faraday conversion might or might not be the dominant form of CP production in SS433. However, as mentioned in the discussion (Section 3.7.2), our constrained value of α is not appropriate for its use to constrain Faraday conversion as main form of the CP mechanism. According to the theory of Faraday conversion, the spectral index ought to be varying from -1 up to -3 for highly relavistic cases. We hence expected $\alpha \geq 1$ for the relativistic jets ($0.26c$) of SS433 . The various plausible explanations for this discrepency are outlined as the following; (i) The plasma may be actually undergoing more than one CP mechanism, where there is a co-dominance of Faraday Conversion and Intrinsically Synchrotron. This value of index α is merely a compromise of both of the plasmas with $\alpha \sim -0.5$ and $\alpha \sim -2$; (ii) It could be that relativistic conditions of plasma for the jets of SS433 at the speed of $\beta \sim 0.26c$ are not strong enough to cause the $|\alpha| > 1$, hence the value obtained is not good enough to confirm the Faraday conversion mechanism as the dominant CP Production mechanism. In short, the question of dominant CP production mechanism in SS433 remain unanswered and need to be investigated through other methodologies.

Since MeerKAT/ThunderKAT would have adequate sensitivity, we would be able to observe circular polarization with better accuracy in future with MeerKAT. This would enable us to determine a better spectrum for circular polarization (CP), and a better constraint on the spectral index as well as the dominant production mechanism for CP emission.

Bibliography

Altamirano, D., Belloni, T., Linares, M., van der Klis, M., Wijnands, R., Curran, P. A., Kalamkar, M., Stiele, H., Motta, S., Muñoz-Darias, T., Casella, P., & Krimm, H. 2011, ApJ, 742, L17

Belloni, T. M. 2010, in Lecture Notes in Physics, Berlin Springer Verlag, Vol. 794, Lecture Notes in Physics, Berlin Springer Verlag, ed. T. Belloni, 53

Benford, G. & Tzach, D. 2000, MNRAS, 317, 497

Bezayiff, N. 2006, PhD thesis, University of California

Blandford, R. D., McKee, C. F., & Rees, M. J. 1977, Nature, 267, 211

Blandford, R. D. & Payne, D. G. 1982, MNRAS, 199, 883

Blundell, K. M. & Bowler, M. G. 2004, ApJ, 616, L159

Brocksopp, C., Corbel, S., Tzioumis, A., Broderick, J. W., Rodriguez, J., Yang, J., Fender, R. P., & Paragi, Z. 2013, MNRAS, 432, 931

Cadolle Bel, M., Ribó, M., Rodriguez, J., Chaty, S., Corbel, S., Goldwurm, A., Frontera, F., Farinelli, R., D'Avanzo, P., Tarana, A., Ubertini, P., Laurent, P., Goldoni, P., & Mirabel, I. F. 2007, ApJ, 659, 549

Calvelo, D. E., Fender, R. P., Russell, D. M., Gallo, E., Corbel, S., Tzioumis, A. K., Bell, M. E., Lewis, F., & Maccarone, T. J. 2010, MNRAS, 409, 839

Cantrell, A. G., Bailyn, C. D., Orosz, J. A., McClintock, J. E., Remillard, R. A., Froning, C. S., Neilsen, J., Gelino, D. M., & Gou, L. 2010, ApJ, 710, 1127

Casares, J. 1996, in Astrophysics and Space Science Library, Vol. 208, IAU Colloq. 158, Cataclysmic Variables and Related Objects, ed. A. Evans & J. H. Wood, 395

Casares, J. & Jonker, P. G. 2014, Space Science Review, 183, 223

Chen, W., Shrader, C. R., & Livio, M. 1997, ApJ, 491, 312

Corbel, S., Coriat, M., Brocksopp, C., Tzioumis, A. K., Fender, R. P., Tomsick, J. A., Buxton, M. M., & Bailyn, C. D. 2013, MNRAS, 428, 2500

Corbel, S., Fender, R. P., Tomsick, J. A., Tzioumis, A. K., & Tingay, S. 2004, ApJ, 617, 1272

Corbel, S., Fender, R. P., Tzioumis, A. K., Tomsick, J. A., Orosz, J. A., Miller, J. M., Wijnands, R., & Kaaret, P. 2002, Science, 298, 196

Corbel, S., Kaaret, P., Fender, R. P., Tzioumis, A. K., Tomsick, J. A., & Orosz, J. A. 2005, ApJ, 632, 504

Corbel, S., Koerding, E., & Kaaret, P. 2008, MNRAS, 389, 1697

Corbel, S., Nowak, M. A., Fender, R. P., Tzioumis, A. K., & Markoff, S. 2003, A&A, 400, 1007

Coriat, M. 2010, PhD thesis, Université Paris Diderot

Coriat, M., Corbel, S., Prat, L., Miller-Jones, J. C. A., Cseh, D., Tzioumis, A. K., Brocksopp, C., Rodriguez, J., Fender, R. P., & Sivakoff, G. R. 2011a, in IAU Symposium, Vol. 275, IAU Symposium, ed. G. E. Romero, R. A. Sunyaev, & T. Belloni, 255–259

Coriat, M., Corbel, S., Prat, L., Miller-Jones, J. C. A., Cseh, D., Tzioumis, A. K., Brocksopp, C., Rodriguez, J., Fender, R. P., & Sivakoff, G. R. 2011b, MNRAS, 414, 677

Del Santo, M., Malzac, J., Belmont, R., Bouchet, L., & De Cesare, G. 2013, in European Physical Journal Web of Conferences, Vol. 61, European Physical Journal Web of Conferences, 3006

Díaz-Trigo, María, T., Miller-Jones, J. C. A., Migliari, S., Broderick, J. W., & Tzioumis, T. 2013, Nature, 504, 260

Done, C., Gierliński, M., & Kubota, A. 2007, A&A, 15, 1

Dubner, G. M., Holdaway, M., Goss, W. M., & Mirabel, I. F. 1998, AJ, 116, 1842

Fabrika, S. 2004, Astrophysics and Space Physics Reviews, 12, 1

Fender, R. 2006, Jets from X-ray binaries, ed. W. H. G. Lewin & M. van der Klis, 381–419

Fender, R. & Belloni, T. 2012, Science, 337, 540

Fender, R., Corbel, S., Tzioumis, T., McIntyre, V., Campbell-Wilson, D., Nowak, M., Sood, R., Hunstead, R., Harmon, A., Durouchoux, P., & Heindl, W. 1999, ApJ, 519, L165

Fender, R., Rayner, D., Norris, R., Sault, R. J., & Pooley, G. 2000, ApJ, 530, L29

Fender, R. P. 1999, ArXiv e-prints, astro-ph/9911176

Fender, R. P., Gallo, E., & Russell, D. 2010, MNRAS, 406, 1425

Fender, R. P., Hjellming, R. M., Tilanus, R. P. J., Pooley, G. G., Deane, J. R., Ogley, R. N., & Spencer, R. E. 2001, MNRAS, 322, L23

Fender, R. P., Homan, J., & Belloni, T. M. 2009, MNRAS, 396, 1370

Fender, R. P. & Pooley, G. G. 2000, MNRAS, 318, L1

Fender, R. P., Rayner, D., McCormick, D. G., Muxlow, T. W. B., Pooley, G. G., Sault, R. J., & Spencer, R. E. 2002, MNRAS, 336, 39

Frank, J., King, A., & Raine, D. J. 2002, Accretion Power in Astrophysics: Third Edition, ISBN 0521620538

Gallo, E., Fender, R. P., Miller-Jones, J. C. A., Merloni, A., Jonker, P. G., Heinz, S., Maccarone, T. J., & van der Klis, M. 2006, MNRAS, 370, 1351

Gallo, E., Fender, R. P., & Pooley, G. G. 2003, MNRAS, 344, 60

Gallo, E., Miller, B. P., & Fender, R. 2012, MNRAS, 423, 590

Gelino, D. M. & Harrison, T. E. 2003, ApJ, 599, 1254

Goodall, P. T., Blundell, K. M., & Bell Burnell, S. J. 2011, MNRAS, 414, 2828

Goranskii, V. P., Esipov, V. F., & Cherepashchuk, A. M. 1998, Astronomy Reports, 42, 336

Hellier, C. 2000, Cataclysmic Variables Stars- How and why they vary, ISBN-13: 978-1852332112, ed. Springer Praxis Books/Space Exploration (Springer)

Hillwig, T. C. & Gies, D. R. 2008, ApJ, 676, L37

Homan, J. & Belloni, T. 2005, AP&SS, 300, 107

Jones, T. W. 1988, ApJ, 332, 678

Jones, T. W. & Odell, S. L. 1977, ApJ, 215, 236

Jonker, P. G., Miller-Jones, J. C. A., Homan, J., Tomsick, J., Fender, R. P., KA&Aret, P., Markoff, S., & Gallo, E. 2012, MNRAS, 423, 3308

Katz, J. I. 1973, Nature, 246, 87

Kembhavi, A. K. & Narlikar, J. V. 1999, Quasars and active galactic nuclei : An introduction, ISBN 0521474779

Kennett, M. & Melrose, D. 1998, PASA, 15, 211

Khargharia, J., Froning, C. S., Robinson, E. L., & Gelino, D. M. 2013, AJ, 145, 21

Lasota, J.-P. 2001, New Astronomical Review, 45, 449

Legg, M. P. C. & Westfold, K. C. 1968, ApJ, 154, 499

Liu, B. F., Yuan, W., Meyer, F., Meyer-Hofmeister, E., & Xie, G. Z. 1999, ApJ, 527, L17

Lubow, S. H. & Shu, F. H. 1975, ApJ, 198, 383

Maccarone, T. J. 2002, MNRAS, 336, 1371

—. 2003, A&A, 409, 697

Macquart, J.-P. & Melrose, D. B. 2000, Physical Reviews, 62, 4177

Macquart, J.-P., Wu, K., Sault, R. J., & Hannikainen, D. C. 2002, A&A, 396, 615

Madej, O. K., García, J., Jonker, P. G., Parker, M. L., Ross, R., Fabian, A. C., & Chenevez, J. 2014, MNRAS, 442, 1157

Margon, B., Grandi, S. A., Stone, R. P. S., & Ford, H. C. 1979, ApJ, 233, L63

Markoff, S., Nowak, M., Corbel, S., Fender, R., & Falcke, H. 2003, A&A, 397, 645

Marsh, T. R. 2000, NAR, 44, 119

Marshall, H. L., Canizares, C. R., Hillwig, T., Mioduszewski, A., Rupen, M., Schulz, N. S., Nowak, M., & Heinz, S. 2013, ApJ, 775, 75

Merloni, A., Heinz, S., & di Matteo, T. 2003, MNRAS, 345, 1057

Migliari, S., Fender, R., & Méndez, M. 2002, Science, 297, 1673

Mirabel, I. F. & Rodriguez, L. F. 1994, Nature, 371, 46

Mirabel, I. F., Rodriguez, L. F., Cordier, B., Paul, J., & Lebrun, F. 1992, Nature, 358, 215

Muñoz-Darias, T., Casares, J., & Martínez-Pais, I. G. 2008, MNRAS, 385, 2205

Narayan, R. & McClintock, J. E. 2012, MNRAS, 419, L69

Narayan, R. & Yi, I. 1995, ApJ, 452, 710

Neilsen, J., Coriat, M., Fender, R., Lee, J. C., Ponti, G., Tzioumis, A., Edwards, P., & Broderick, J. 2014, in AAS meeting, Vol. 224, American Astronomical Society Meeting Abstracts #224, 204

Nelemans, G., Wood, M., Groot, P., Anderson, S., Belczynski, K., Benacquista, M., Charles, P., Cumming, A., Deloye, C., Jonker, P., Kalogera, V., Knigge, C., Marsh, T., Motl, P., Napiwotzki, R., O'Brien, K., Phinney, E. S., Ramsay, G., Shahbaz, T., Solheim, J.-E., Steeghs, D., van der Sluys, M., Verbunt, F., Warner, B., Werner, K., Wu, K., & Yungelson, L. R. 2009, in ArXiv Astrophysics e-prints, Vol. 2010, The Astronomy and Astrophysics Decadal Survey 2010, 221

Neustroev, V. V., Veledina, A., Poutanen, J., Zharikov, S. V., Tsygankov, S. S., Sjoberg, G., & Kajava, J. J. E. 2014, MNRAS, 445, 2424

Ogilvie, G. I. & Dubus, G. 2001, MNRAS, 320, 485

Ohsuga, K., Mori, M., Nakamoto, T., & Mineshige, S. 2005, ApJ, 628, 368

Orosz, J. A. 2003, in IAU Symposium, Vol. 212, A Massive Star Odyssey: From Main Sequence to Supernova, ed. K. van der Hucht, A. Herrero, & C. Esteban, 365

Orosz, J. A., McClintock, J. E., Aufdenberg, J. P., Remillard, R. A., Reid, M. J., Narayan, R., & Gou, L. 2011a, ApJ, 742, 84

Orosz, J. A., McClintock, J. E., Remillard, R. A., & Corbel, S. 2004, ApJ, 616, 376

Orosz, J. A., Steiner, J. F., McClintock, J. E., Torres, M. A. P., Remillard, R. A., Bailyn, C. D., & Miller, J. M. 2011b, ApJ, 730, 75

O'Sullivan, S. P., McClure-Griffiths, N. M., Feain, I. J., Gaensler, B. M., & Sault, R. J. 2013, MNRAS, 435, 311

Özel, F., Psaltis, D., Narayan, R., & McClintock, J. E. 2010, ApJ, 725, 1918

Panferov, A. A. 2011, ArXiv e-prints 1103.4707

Paragi, Z., Vermeulen, R. C., Fejes, I., Schilizzi, R. T., Spencer, R. E., & Stirling, A. M. 1999, A&A, 348, 910

Paragi, Z., Vermeulen, R. C., Homan, D. C., Wardle, J. F. C., Fejes, I., Schilizzi, R. T., Spencer, R. E., & Stirli, A. M. 2004, in European

VLBI Network on New Developments in VLBI Science and Technology, ed. R. Bachiller, F. Colomer, J.-F. Desmurs, & P. de Vicente, 221–224

Patruno, A., Archibald, A. M., Hessels, J. W. T., Bogdanov, S., Stappers, B. W., Bassa, C. G., Janssen, G. H., Kaspi, V. M., Tendulkar, S., & Lyne, A. G. 2014, ApJ, 781, L3

Pe'er, A. & Markoff, S. 2012, ApJ, 753, 177

Plotkin, R. M., Markoff, S., Kelly, B. C., Körding, E., & Anderson, S. F. 2012, MNRAS, 419, 267

Ratti, E. M., Jonker, P. G., Miller-Jones, J. C. A., Torres, M. A. P., Homan, J., Markoff, S., Tomsick, J. A., KA&Aret, P., Wijnands, R., Gallo, E., Özel, F., Steeghs, D. T. H., & Fender, R. P. 2012, MNRAS, 423, 2656

Rayner, D. 2000, PASA, 17, 284

Rayner, D. P., Norris, R. P., & Sault, R. J. 2000, MNRAS, 319, 484

Rebusco, P., Moskalik, P., Kluźniak, W., & Abramowicz, M. A. 2012, A&A, 540, L4

Remillard, R. A. & McClintock, J. E. 2006, A&A, 44, 49

Rodriguez, J., Cadolle Bel, M., Tomsick, J. A., Corbel, S., Brocksopp, C., Paizis, A., Shaw, S. E., & Bodaghee, A. 2007, ApJ, 655, L97

Rodriguez, J., Corbel, S., Caballero, I., Tomsick, J. A., Tzioumis, T., Paizis, A., Cadolle Bel, M., & Kuulkers, E. 2011, A&A, 533, L4

Rushton, A., Spencer, R., Fender, R., & Pooley, G. 2010, A&A, 524, A29

Russell, D. M., Maitra, D., Dunn, R. J. H., & Fender, R. P. 2011, MNRAS, 416, 2311

Russell, D. M. & Shahbaz, T. 2013, in European Physical Journal Web of Conferences, Vol. 61, European Physical Journal Web of Conferences, 1006

Russell, T. D., Soria, R., Miller-Jones, J. C. A., Curran, P. A., Markoff, S., Russell, D. M., & Sivakoff, G. R. 2014, MNRAS, 439, 1390

Sathyaprakash, B. S. 2013, Comptes Rendus Physique, 14, 272

Sault, R. J., Teuben, P. J., & Wright, M. C. H. 1995, in Astronomical Society of the Pacific Conference Series, Vol. 77, Astronomical Data Analysis Software and Systems IV, ed. R. A. Shaw, H. E. Payne, & J. J. E. Hayes, 433

Shahbaz, T. 2003, MNRAS, 339, 1031

Shahbaz, T., Russell, D. M., Zurita, C., Casares, J., Corral-Santana, J. M., Dhillon, V. S., & Marsh, T. R. 2013, MNRAS, 434, 2696

Shakura, N. I. & Sunyaev, R. A. 1973, A&A, 24, 337

Shaposhnikov, N., Markwardt, C., Swank, J., & Krimm, H. 2010, in The First Year of MAXI: Monitoring Variable X-ray Sources

Shaposhnikov, N., Swank, J. H., Markwardt, C., & Krimm, H. 2011, ArXiv

Shaposhnikov, N. & Titarchuk, L. 2009, ApJ, 699, 453

Shklovskii, I. S. 1981, Soviet Astronomy, 25, 315

Soleri, P. & Fender, R. 2011, MNRAS, 413, 2269

Soleri, P., Fender, R., Tudose, V., Maitra, D., Bell, M., Linares, M., Altamirano, D., Wijnands, R., Belloni, T., Casella, P., Miller-Jones, J. C. A., Muxlow, T., Klein-Wolt, M., Garrett, M., & van der Klis, M. 2010, MNRAS, 406, 1471

Steeghs, D., McClintock, J. E., Parsons, S. G., Reid, M. J., Littlefair, S., & Dhillon, V. S. 2013, ApJ, 768, 185

Steiner, J. F., McClintock, J. E., & Narayan, R. 2013, ApJ, 762, 104

Stirling, A. M., Spencer, R. E., de la Force, C. J., Garrett, M. A., Fender, R. P., & Ogley, R. N. 2001, MNRAS, 327, 1273

Tananbaum, H., Gursky, H., Kellogg, E., Giacconi, R., & Jones, C. 1972, ApJ, 177, L5

Tauris, T. M. & van den Heuvel, E. P. J. 2006, Formation and evolution of compact stellar X-ray sources, ed. W. H. G. Lewin & M. van der Klis, 623–665

Tingay, S. J., Jauncey, D. L., Preston, R. A., Reynolds, J. E., Meier, D. L., Murphy, D. W., Tzioumis, A. K., McKay, D. J., Kesteven, M. J., Lovell, J. E. J., Campbell-Wilson, D., Ellingsen, S. P., Gough, R., Hunstead, R. W., Jonos, D. L., McCulloch, P. M., Migenes, V., Quick, J., Sinclair, M. W., & Smits, D. 1995, Nature, 374, 141

Van der Klis, M. 2006, Rapid X-ray Variability, ed. W. H. G. Lewin & M. van der Klis, 39–112

Vila, G. S. & Romero, G. E. 2010, MNRAS, 403, 1457

Wagner, R. M., Kreidl, T. J., Howell, S. B., & Starrfield, S. G. 1992, ApJ, 401, L97

Wardle, J. F. C., Dare, E. A., & Cheung, C. C. 2011, in American Astronomical Society Meeting Abstracts #218, 230

Wardle, J. F. C. & Homan, D. C. 2001, in Astronomical Society of the Pacific Conference Series, Vol. 250, Particles and Fields in Radio Galaxies Conference, ed. R. A. Laing & K. M. Blundell, 152

Wardle, J. F. C., Homan, D. C., Ojha, R., & Roberts, D. H. 1998, Nature, 395, 457

Warner, B. 1995, Cambridge Astrophysics Series, 28

Xie, F.-G. & Yuan, F. 2012, MNRAS, 427, 1580

Zhang, X. L., Feng, Y. X., Zhang, S. N., & Yao, Y. 2002, in Bulletin of the AAS, Vol. 34, AAS, 1123